Sensitivity Studies for the ORCA and Super-ORCA Neutrino Detector

Master's Thesis in Physics

Presented by

Marc Bruchner

30.11.2018

Erlangen Centre for Astroparticle Physics
Physikalisches Institut
Friedrich-Alexander-Universität Erlangen-Nürnberg

1. Supervisor: PD Dr. Thomas Eberl
2. Supervisor: Prof. Dr. Gisela Anton

Contents

Chapter 1

Introduction

As part of the Standard Model (SM) of particle physics, neutrinos are crucial for the understanding of our Universe. Despite the conservation of the lepton number demanded by the SM, solar neutrino studies have shown that neutrinos violate this conservation by changing their flavours while propagating [1], an effect called neutrino oscillation. While the theoretical nature of these oscillations is well understood, there are a few parameters still unknown, while most of them have been determined with sufficient precision.

Two important oscillation parameters are the neutrino mass hierarchy (NMH), which is defined by the sign of the large squared mass difference ΔM^2, and the CP-violating phase δ_{CP}. Both parameters can be determined by further studies with neutrinos in the GeV-energy range, planned by the KM3NeT collaboration by measuring neutrino oscillation occurring during the neutrino's path through Earth. In order to do so, a new detector known as ORCA (Oscillation Research with Cosmics in the Abyss) is used, which is currently under construction [2]. While ORCA is optimized to determine the NMH, δ_{CP} is more difficult to measure, which is why we are already investigating the successor called Super-ORCA, a much more-densely instrumented detector. Although this is a completely hypothetical detector, we can present its high capabilities in this thesis.

This thesis focuses on preliminary sensitivity studies for the determination of the NMH using ORCA and Super-ORCA. The calculation is based on the Asimov approach [5], a technique to calculate sensitivities. The neutrinos used in the studies are either produced in the atmosphere or are generated as a beam by a particle accelerator.

The thesis is organised as follows: chapter 2 begins with an introduction to the scientific background, focusing on the theoretical description of neutrino oscillations (section 2.1), the neutrino sources we use (section 2.2) and the general idea of detection via Cherenkov light (section 2.3). Chapter 3 then continues with sensitivity studies for ORCA, introducing the software used, called *paramNMH* (section 3.1), showing the influence of a new set of parameters describing systematic uncertainties to make the calculation, done by *paramNMH*, more realistic (section 3.2), and doing sensitivity studies by using a neutrino beam instead of the atmospheric neutrino flux (section 3.3). Finally, in chapter 4 we will move on to sensitivity studies with a hypothetical denser detector, taking a closer look at the detector performance of Super-ORCA compared to ORCA (section 4.1), and showing the results concerning the sensitivity to determine δ_{CP} using atmospheric neutrinos (section 4.2) and neutrino beams (section 4.3).

Chapter 2

Scientific Background

2.1 Neutrino Oscillations

In this section we will describe the basic theory of neutrino oscillation which is important for determining the so called neutrino mass hierarchy (NMH) and the CP-violation phase δ_{CP}. All formulas have been taken from [6], [8] and [9].

2.1.1 Neutrino Oscillations in Vacuum

Due to solving the solar neutrino flux problem, where less electron neutrinos have been detected than expected, neutrino oscillation was first mentioned to solve the problem by PONTECORVO [3] in 1957, and later accepted due to measurements with atmospheric neutrinos. The here considered oscillation theory was invented by MAKI, NAKAGAWA and SAKATA in 1962 [4]. Their assumption was to treat neutrinos as massive particles while their mass is only a tiny fraction of the electron mass, so they hardly interact via gravity but due to weak interaction with their surrounding. However, the particles interacting this way are only a superposition of the neutrinos with different masses.

Therefore, we distinguish the neutrinos in two sets of different eigenstates:

mass eigenstates $|\nu_k\rangle$ describe the propagating neutrinos with different but fixed masses. In the three neutrino model we have three different mass eigenstates with masses m_k where $k = 1, 2, 3$. Mass eigenstates are defined by numbers as index if they are clearly defined, or Latin letters if they are undefined.

flavour eigenstates $|\nu_\alpha\rangle$ describe the interacting particles that preserve the lepton number. In the three neutrino model we distinguish between ν_e, ν_μ and ν_τ corresponding to the three heavy leptons electron e, muon μ and tau τ. Flavour eigenstates are written with a Greek letter as index if undefined.

A simple example of a neutrino oscillation can be described as the following: a neutrino is generated as an $|\nu_e\rangle$ due to a β-decay, it propagates as an superposition of $|\nu_1\rangle$, $|\nu_2\rangle$ and $|\nu_3\rangle$, and interacts again as a $|\nu_\mu\rangle$, generating a μ. While propagating, the ratio of the mass eigenstate superposition changes, so the amplitude of each eigenstate $|\nu_1\rangle$, $|\nu_2\rangle$ and $|\nu_3\rangle$ oscillates with time. With that, the composition of the superposition is likely to be different at the target compared to the state at the generation of the neutrino.

To describe the relation between mass and flavour eigenstates, we use the complex unitary PMNS mixing matrix $\mathcal{U}$, named after the first letters of its inventors' names:

$$\begin{pmatrix} \nu_e \\ \nu_\mu \\ \nu_\tau \end{pmatrix} = \mathcal{U} \times \begin{pmatrix} \nu_1 \\ \nu_2 \\ \nu_3 \end{pmatrix} \tag{2.1}$$

So the flavour eigenstates can be written as a superposition of the mass eigenstates (similar for antineutrinos):

$$|\nu_\alpha\rangle = \sum_k \mathcal{U}^*_{\alpha k} \, |\nu_k\rangle \, , \tag{2.2}$$

$$|\bar{\nu}_\alpha\rangle = \sum_k \mathcal{U}_{\alpha k} \, |\bar{\nu}_k\rangle \, . \tag{2.3}$$

For the other way around we get for the mass eigenstates:

$$\begin{aligned} |\nu_k\rangle &= \sum_\alpha ((\mathcal{U}^*)^\dagger)_{k\alpha} \, |\nu_\alpha\rangle \\ &= \sum_\alpha \mathcal{U}_{\alpha k} \, |\nu_\alpha\rangle \, , \end{aligned} \tag{2.4}$$

$$|\bar{\nu}_k\rangle = \sum_\alpha \mathcal{U}^*_{\alpha k} \, |\bar{\nu}_\alpha\rangle \, . \tag{2.5}$$

Here we used the PMNS matrix to be unitary:

$$\mathcal{U}^\dagger \mathcal{U} = \mathrm{id} \quad \Rightarrow \quad \mathcal{U}^{-1} = \mathcal{U}^\dagger = (\mathcal{U}^*)^T \tag{2.6}$$

In the following, we want to calculate the probability $P_{\nu_\alpha \to \nu_\beta}(L, E)$ which describes a neutrino with energy E, that is generated as ν_α, is measured as ν_β after a propagating distance L. As we stated before, the amplitudes of the mass eigenstates oscillate with time (and therefore fulfil the Schrödinger equation):

$$|\nu_k(t)\rangle = e^{-iE_k t} \, |\nu_k\rangle \, . \tag{2.7}$$

The energy E_k can be described as:

$$E_k = \sqrt{p^2 + m_k^2} \approx p + \frac{m_k^2}{2p} \approx E + \frac{m_k^2}{2E}, \tag{2.8}$$

due to the Taylor expansion because $p >> m_k$ and therefore $E \approx p$ in natural units $(c = 1)$.

Now we can describe the flavour eigenstate in dependence of time t, using the equations (2.2), (2.4) and (2.7).

$$|\nu_\alpha(t)\rangle \;=\; \sum_{k,\gamma} \mathcal{U}^*_{\alpha k}\, \mathcal{U}_{\gamma k}\; e^{-iE_k t}\;\; |\nu_\gamma\rangle\,. \tag{2.9}$$

Note that α is the flavour of the neutrino at time $t = 0$ such that $|\nu_\alpha(t = 0)\rangle = |\nu_\alpha\rangle$.

With that we can calculate the time-dependent transition amplitude:

$$\begin{aligned} A(\alpha \to \beta; t) \;&=\; \langle \nu_\beta | \nu_\alpha(t)\rangle \\ &=\; \sum_k \mathcal{U}^*_{\alpha k}\, \mathcal{U}_{\beta k}\; e^{-iE_k t} \;=\; (\mathcal{U}^*\; D\, \mathcal{U})_{\alpha\beta}. \end{aligned} \tag{2.10}$$

Here we use $\langle \nu_\beta | \nu_\gamma\rangle = \delta_{\gamma\beta}$ and the diagonal matrix $D_{kj} = \delta_{kj} \exp(-iE_k t)$. By using (2.8), $E \approx p$, the amplitude of $|\nu_k\rangle$ oscillating with $\exp(-ipt)$ and the distance between the $|\nu_\alpha\rangle$-source and the detector $L = ct$ $(c = 1)$, we can write that as:

$$A(\alpha \to \beta; t) \;=\; \sum_k \mathcal{U}^*_{\alpha k}\, \mathcal{U}_{\beta k}\; e^{-i\,\frac{m_k^2}{2}\,\frac{L}{E}} \;=\; A(\alpha \to \beta; L). \tag{2.11}$$

For antineutrinos we find the relationship:

$$A(\overline{\alpha} \to \overline{\beta}) \;=\; A(\beta \to \alpha). \tag{2.12}$$

The three important symmetry operations in particle physics are the charge conjugation symmetry (C-symmetry), where we compare a particle with its antiparticle, the parity symmetry (P-symmetry), where we invert the spatial coordinates $\mathbf{r} \to -\mathbf{r}$ and the time-symmetry (T-symmetry), where we invert the direction of time $t \to -t$ [11]. Until now, the combination of that symmetries CPT is always preserved, so the physics for a particle is exactly the same as for its antiparticle with inverted spatial and time coordinates.

C-symmetry alone is broken by the fact we have only left-handed neutrinos and right-handed antineutrinos, because with the C-transition of a neutrino, we should get a left-handed antineutrino, which doesn't exist at the momentary state of knowledge. Therefore we can distinguish between ν and $\bar{\nu}$ by distinguishing the chirality. However, the problem can be solved by changing the parity of the antineutrino, so the CP-symmetry is preserved. Still, there are some cases in the quark sector, like the decay of a kaon, that leads us to a CP-violation. Now we are looking for a CP-violation in the neutrino sector as well.

As we can see, the CPT-symmetry is preserved by eq. (2.12), because C converts the particles into anti-particles, P changes the helicity from left-handed to right-handed, and T changes the direction of the arrow. If we assume time-invariance of eq. (2.12), we would get as a result that the CP-symmetry is preserved as well:

$$A(\overline{\alpha} \to \overline{\beta}) \;=\; A(\alpha \to \beta) \;\overset{\mathrm{CP}}{=}\; A(\overline{\beta} \to \overline{\alpha}) \;=\; A(\beta \to \alpha). \tag{2.13}$$

We can test eq. (2.13) by measuring and comparing the oscillation probabilities of $P_{\nu_\alpha \to \nu_\beta}$ and $P_{\nu_\beta \to \nu_\alpha}$. If we have CP-violation, and therefore no invariance of time, the second equation sign in eq. (2.13) is wrong. We can describe this CP-violation due to a phase δ_{CP} as part of the PMNS mixing matrix $\mathcal{U}$. If the value of δ_{CP} differs from $n \cdot \pi$, $n \in \mathbb{Z}$, CP-symmetry would be violated.

Using equations (2.11) and (2.12), we can calculate the transition probability as:

$$\begin{aligned} P_{\nu_\alpha \to \nu_\beta}(L, E) &= |A(\alpha \to \beta; t)|^2 \\ &= \sum_{k,j} \mathcal{U}^*_{\alpha k}\, \mathcal{U}_{\beta k}\, \mathcal{U}_{\alpha j}\, \mathcal{U}^*_{\beta j}\, e^{i \Delta_{kj}}, \end{aligned} \tag{2.14}$$

where we have the phase difference:

$$\Delta_{kj} = -\frac{\Delta m^2_{kj}}{2} \cdot \frac{L}{E} \quad \text{with} \quad \Delta m^2_{kj} = m^2_k - m^2_j. \tag{2.15}$$

It can be seen from eq. (2.14) that it is not possible to measure the exact mass of the neutrinos by neutrino oscillation experiments but the squared mass difference between the three masses of the mass eigenstates only. While the value of Δm^2_{21} is known very well (by experiments with solar neutrinos [10]), only the absolute value of Δm^2_{23} could have been determined by now (using atmospheric neutrinos). So the mass ordering is still unknown (values taken from [8]):

$$\Delta m^2_{21} = \Delta m^2_{\mathrm{sol}} = (7.54^{+0.26}_{-0.22}) \times 10^{-5} \mathrm{eV}^2, \tag{2.16}$$

$$|\Delta m^2_{32}| = \Delta m^2_{\mathrm{atm}} = \Delta M^2 = (2.43 \pm 0.06) \times 10^{-3} \mathrm{eV}^2. \tag{2.17}$$

Depending on the sign of Δm^2_{32}, we distinguish two different neutrino mass hierarchies: the normal hierarchy (NH) assumes that the three different masses of the neutrino mass eigenstates are ordered by their numbers, starting with m_1 being the smallest mass and m_3 being the largest mass (Δm^2_{32} positive). The inverted hierarchy (IH) takes the other sign and postulates that m_3 is the smallest mass (Δm^2_{32} negative). However, due to the fact of the known sign of Δm^2_{21}, we know that m_2 is higher than m_1 (see Fig. 2.1).

To calculate the transition probability we need to know the values of the PMNS matrix, which can be written similar to the CKM matrix in the quark sector. Depending on the model we use for describing neutrino physics, $\mathcal{U}$ can be a 2 × 2-matrix (2-flavour model) or a 3 × 3-matrix (3-flavour model). If we take sterile neutrinos into account, what we will not do here, the matrix could even have a higher dimension.

If we use the 2-flavour model (ν_e, ν_μ), we only have one mixing angle θ. This model does not describe the reality as good as the 3-flavour model, but it is easier to understand, what we will use later for the description for oscillations in matter. However, the conceptional mathematics behind both models is still the same, so looking at the 2-flavour model will give us information on the 3-flavour model as well. Here, the mixing matrix can be written as:

$$\mathcal{U} = \begin{pmatrix} \cos\theta & \sin\theta \\ -\sin\theta & \cos\theta \end{pmatrix}. \tag{2.18}$$

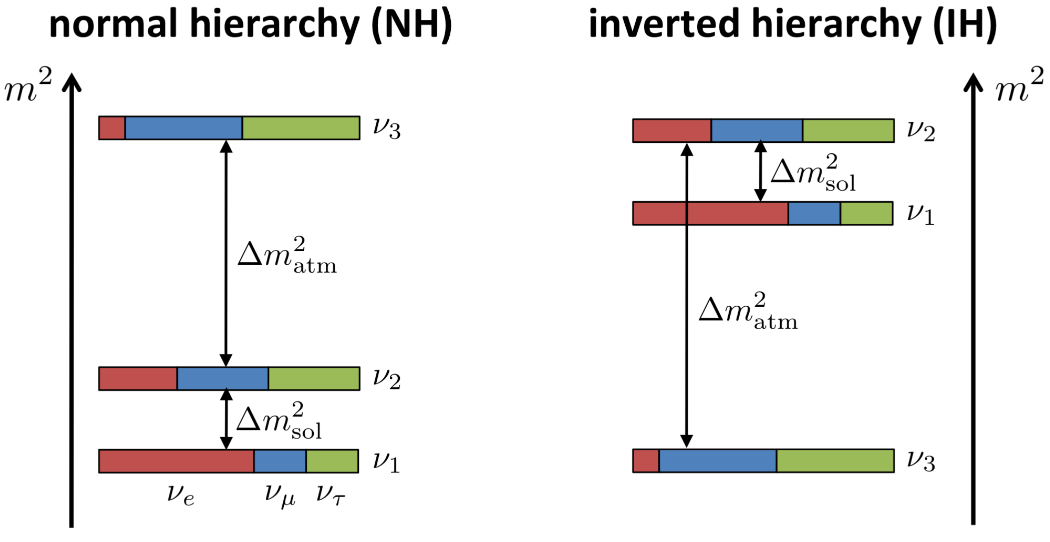

Figure 2.1: Neutrino mass hierarchy: the normal hierarchy (NH) describes the model where the mass m_3 is heavier than m_1 and m_2, while the inverted hierarchy (IH) assumes it to be lighter. In both cases, experiments with solar neutrinos proved m_2 to be larger than m_1 [10]. Additionally the mass eigenstates are split into their flavour eigenstates (different colours) by using the absolute values of the PMNS mixing matrix. [7]

Using the 3-flavour model we will have three different mixing angles θ_{kj} with $k, j = 1, 2, 3$ and $k \neq j$, as well as a CP-violating phase δ_{CP}. The two Majorana phases are neglected here, assuming we are working with Dirac particles. In the following we use $c_{kj} = \cos\theta_{kj}$ and $s_{kj} = \sin\theta_{kj}$.

$$\mathcal{U} = \begin{pmatrix} c_{12}c_{13} & s_{12}c_{13} & s_{13}e^{-i\delta_{\text{CP}}} \\ -s_{12}c_{23} - c_{12}s_{23}s_{13}e^{i\delta_{\text{CP}}} & c_{12}c_{23} - s_{12}s_{23}s_{13}e^{i\delta_{\text{CP}}} & s_{23}c_{13} \\ s_{12}s_{23} - c_{12}c_{23}s_{13}e^{i\delta_{\text{CP}}} & -c_{12}s_{23} - s_{12}c_{23}s_{13}e^{i\delta_{\text{CP}}} & c_{23}c_{13} \end{pmatrix}. \tag{2.19}$$

Different measurements like measuring solar neutrinos or reactor neutrinos determined the values of all mixing angles (values taken from [8]):

$$\theta_{12} = (33.4^{+1.05}_{-1.07})^\circ, \tag{2.20}$$
$$\theta_{13} = (8.42 \pm 0.26)^\circ, \tag{2.21}$$
$$\theta_{23} = (41 \pm 2)^\circ. \tag{2.22}$$

Of those three, only θ_{12} has no significant influence on the measurement of NMH and δ_{CP} and will therefore be assumed to be a constant. θ_{13} and especially θ_{23} have a strong influence on the mass hierarchy, so these mixing angles can be used as fit parameters later.

To calculate the fluxes at the detector site Φ', we have to take the initial fluxes Φ of the atmospheric neutrinos or of the beam without oscillation into account, as well as the oscillation probabilities:

$$\begin{aligned}
\Phi'(\nu_e) &= P_{\nu_e\to\nu_e}(L,E)\cdot\Phi(\nu_e) + P_{\nu_\mu\to\nu_e}(L,E)\cdot\Phi(\nu_\mu) + P_{\nu_\tau\to\nu_e}(L,E)\cdot\Phi(\nu_\tau),\\
\Phi'(\nu_\mu) &= P_{\nu_e\to\nu_\mu}(L,E)\cdot\Phi(\nu_e) + P_{\nu_\mu\to\nu_\mu}(L,E)\cdot\Phi(\nu_\mu) + P_{\nu_\tau\to\nu_\mu}(L,E)\cdot\Phi(\nu_\tau),\\
\Phi'(\nu_\tau) &= P_{\nu_e\to\nu_\tau}(L,E)\cdot\Phi(\nu_e) + P_{\nu_\mu\to\nu_\tau}(L,E)\cdot\Phi(\nu_\mu) + P_{\nu_\tau\to\nu_\tau}(L,E)\cdot\Phi(\nu_\tau).
\end{aligned}$$

Whether we use the atmospheric neutrino flux or a generated beam as a neutrino source, $\Phi(\nu_\tau)$ will be always set to 0, so all measured ν_τ are generated solely by oscillation.

2.1.2 Neutrino Oscillations in Matter

Until now we have assumed neutrinos are propagating in vacuum which is a reasonable assumption for space but does not work anymore for propagating through the Earth. As we will see later, we will mainly take up-going neutrinos into account (neutrinos coming from below and traversing Earth) because down-going neutrinos have do not carry information on the NMH. In order to measure NMH, we need neutrino oscillation taking place inside the Earth. For that reason we have to understand how neutrino oscillation changes in matter.

For simplicity, we will study this subject in the 2-flavour model (ν_e, ν_μ). We rewrite eq. (2.1), using eq. (2.18) for the mixing matrix:

$$\begin{pmatrix}\nu_e\\ \nu_\mu\end{pmatrix} = \begin{pmatrix}\cos\theta & \sin\theta\\ -\sin\theta & \cos\theta\end{pmatrix}\begin{pmatrix}\nu_1\\ \nu_2\end{pmatrix}. \tag{2.23}$$

As we have already mentioned in eq. (2.7) the time-dependent mass eigenstates are a solution of the Schrödinger equation:

$$i\,\frac{\mathrm{d}\boldsymbol{\nu}(t)}{\mathrm{d}t} = H^k\,\boldsymbol{\nu}(t), \qquad \text{with} \quad \boldsymbol{\nu} = \begin{pmatrix}\nu_1\\ \nu_2\end{pmatrix}. \tag{2.24}$$

H^k is the Hamiltonian for the mass eigenstates which is diagonal in vacuum:

$$H^k = \frac{1}{2p}\begin{pmatrix}m_1^2 & 0\\ 0 & m_2^2\end{pmatrix}. \tag{2.25}$$

The Hamiltonian can be converted from the form for mass eigenstates H^k into the form for flavour eigenstates H^α using the mixing matrix U:

$$H^\alpha = \mathcal{U}H^k\mathcal{U}^\dagger = \frac{1}{4p}\,\Sigma\begin{pmatrix}1 & 0\\ 0 & 1\end{pmatrix} + \frac{1}{4p}\,D\begin{pmatrix}-\cos2\theta & \sin2\theta\\ \sin2\theta & \cos2\theta\end{pmatrix}, \tag{2.26}$$

with $\Sigma = m_1^2 + m_2^2$ and $D = m_2^2 - m_1^2$.

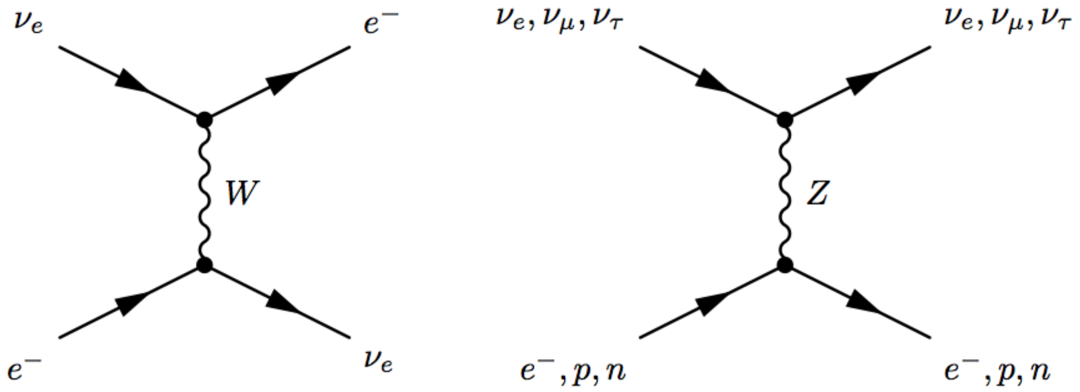

Figure 2.2: Coherent elastic forward scattering for the CC interaction (left) and the NC interaction (right). While the NC-scattering applies to all flavours and it only results in a phase factor equal for all flavours, the CC-scattering works only for electron neutrinos, which generates a potential V^{eff} affecting ν_e only. [9]

In matter we will experience a significant change in oscillation due to the different interactions of $\overset{(-)}{\nu_e}$ compared to the other flavours. The reason for that is a coherent elastic forward scattering with surrounding matter via the weak interaction (see Fig. 2.2). All flavours interact with matter due to the neutral current (NC) scattering (via the Z boson) in the same way, causing a shared phase factor without any physical effect. However, only $\overset{(-)}{\nu_e}$ undergo charged current (CC) scattering (via the $W^\pm$ boson), because normal matter consists mainly of electrons but not of muons and taus.

This can be described by an effective potential affecting only ν_e (+) and $\bar{\nu}_e$ (−):

$$V^{\text{eff}} = \pm\sqrt{2}G_{\text{F}}N_e, \tag{2.27}$$

where G_{F} is the Fermi coupling constant and N_e the electron number density. With that the first entry of the Hamiltonian H^α changes:

$$H^\alpha_m = H^\alpha + \frac{1}{2p}\begin{pmatrix} A & 0 \\ 0 & 0 \end{pmatrix}, \tag{2.28}$$

with the additional term and using that $E \approx p$:

$$A = 2EV^{\text{eff}} = 2\sqrt{2}G_{\text{F}}N_e p. \tag{2.29}$$

Therefore the mass difference D changes as well:

$$D_{\text{m}} = D\sqrt{\left(\frac{A}{D} - \cos 2\theta\right)^2 + \sin^2 2\theta}, \tag{2.30}$$

and with that the mixing angle:

$$\sin 2\theta_{\text{m}} = \frac{\sin 2\theta}{\sqrt{\left(\frac{A}{D} - \cos 2\theta\right)^2 + \sin^2 2\theta}}. \tag{2.31}$$

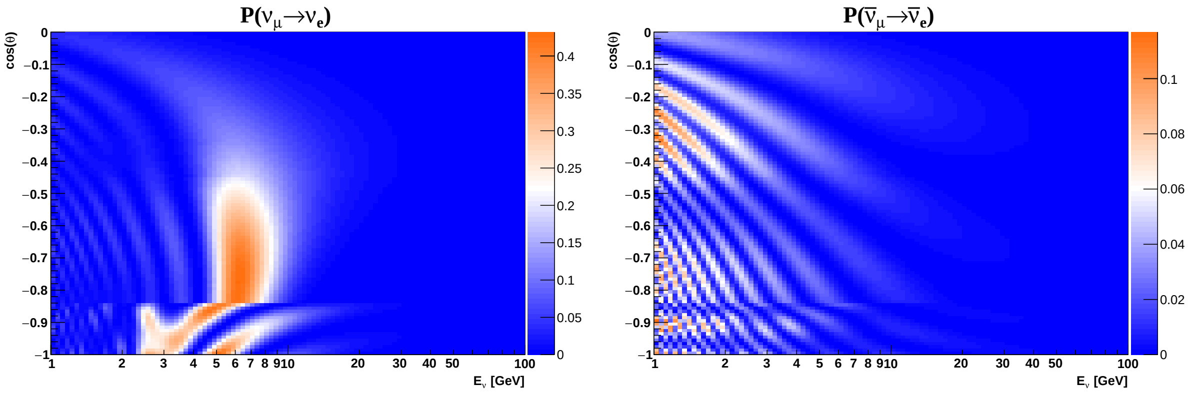

(a) ν and NH (b) $\bar{\nu}$ and NH

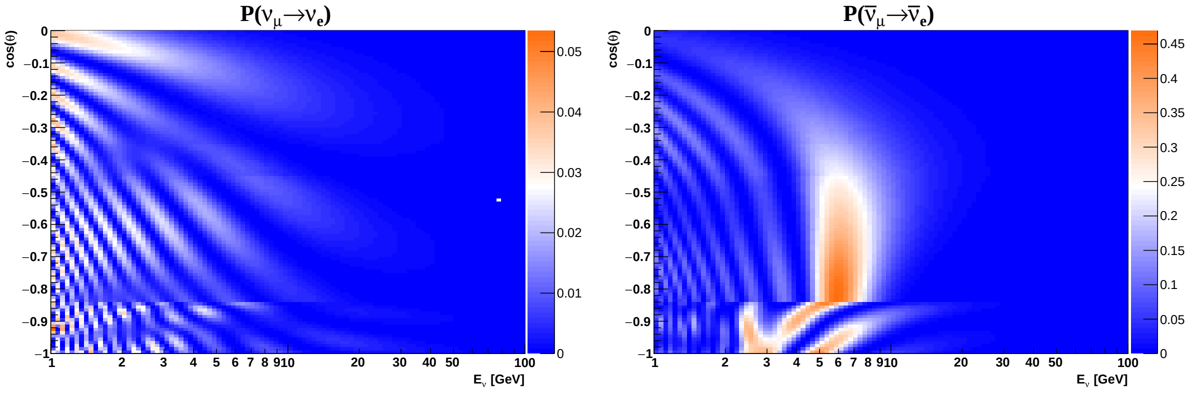

(c) ν and IH (d) $\bar{\nu}$ and IH

Figure 2.3: Oscillation probability for $\nu_\mu \to \nu_e$ and $\bar{\nu}_\mu \to \bar{\nu}_e$ for NH and IH. While (a) and (d) are showing a resonance between 2 and 10 GeV, depending on the path through Earth, (b) and (c) do not have this resonance. The visible line at $\cos\theta_{zenith} \approx -0.85$ describes the transition between the Earth's mantle and its denser core.

For the 2-flavour model we have the following oscillation probability:

$$P_{\mathrm{m}}(\nu_e \to \nu_\mu) \;=\; \sin 2\theta_{\mathrm{m}} \cdot \sin^2 \frac{\Delta_{\mathrm{m}}}{2}, \qquad \text{with} \quad \Delta_{\mathrm{m}} = \frac{D_{\mathrm{m}}}{2} \cdot \frac{L}{p}. \tag{2.32}$$

The resonance at $A/D \approx \cos 2\theta$ is dependent on the mass squared difference D, which helps us to determine the neutrino mass hierarchy. The resonance occurs at energy E_0 that has to be positive for neutrinos or negative for antineutrinos:

$$E_0 \;=\; \frac{D \cos 2\theta}{2V^{\mathrm{eff}}}. \tag{2.33}$$

If E_0 is positive, the resonance occurs only for neutrinos and $D > 0$. If E_0 is negative, only antineutrinos are subject to the resonance and $D < 0$.

For the 3-flavour case we are dealing with two different squared mass differences Δm^2_{21} and Δm^2_{32}. While the resonance and therefore the sign of Δm^2_{21} has been determined by SNO [14], the sign of Δm^2_{32} is still unknown (see Fig. 2.1). Fortunately, the resonance of Δm^2_{32} happens in the Earth and can be measured at energies between $E_0 = 2$ GeV and $E_0 = 10$ GeV, depending on the density of the Earth's mantle and core. From now on we will use $\Delta M^2 := \Delta m^2_{32}$ for the large squared mass difference.

To now evaluate the sign of ΔM^2, we use the fact that A is depending on V^{eff}, which has a different sign for neutrinos and antineutrinos. Therefore, only in one of the two chiralities occurs a resonance due to $A/D \approx \cos 2\theta$. This is only the case, while A/D is positive:

(a) neutrinos (A positive), NH (D positive) → resonance,
(b) antineutrinos (A negative), NH (D positive) → no resonance,
(c) neutrinos (A positive), IH (D negative) → no resonance,
(d) antineutrinos (A negative), IH (D negative) → resonance.

So depending on the NMH, only neutrinos or antineutrinos will show a resonance, by which we can determine the sign of the large squared mass difference $\Delta M^2 = D$. In Fig. 2.3 the resonance can be seen, depending on the energy and the matter profile of the Earth in the propagating path of the (anti-)neutrinos, determined by $\cos\theta_{\text{zenith}}$. The transition from the Earth's mantle to the denser core is clearly visible at $\cos\theta_{\text{zenith}} \approx -0.85$.

2.2 Natural Neutrino Sources

While ARCA, the other detector built by the KM3NeT collaboration, is searching for galactic or extragalactic neutrino sources, ORCA is using the atmospheric neutrino flux or a neutrino beam to determine the values of the oscillation parameters.

Atmospheric neutrinos are generated by cosmic ray particles interacting with particles in Earth's upper atmosphere. The flux of these particles, and therefore that of the atmospheric neutrinos, follows a powerlaw depending on the particle's energy:

$$N(E) \propto E^{-\alpha}, \tag{2.34}$$

where $\alpha = 2.7$ for energies $E < 10^{15}$ eV (1 PeV) and $\alpha = 3.1$ for energies $E > 10^{15}$ eV. The steepening at 1 PeV is called the *knee* between galactic sources (lower energies) like supernovae or pulsars, and extragalactic sources (higher energies) like Active Galaxies, Gamma Ray Bursts and starburst galaxies [15]. However, because we are operating in the GeV energy range, we can assume α to be constant.

Due to spallation of atoms in the atmosphere due to interaction with those high-energy particles, secondary particles are generated, mainly neutrons, protons and pions. Resting

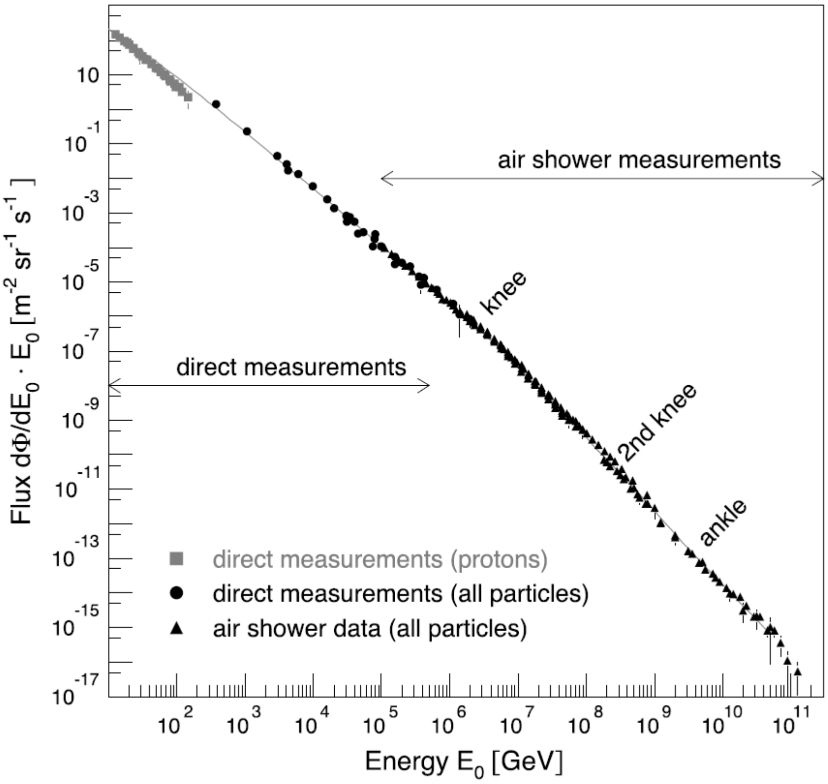

Figure 2.4: The flux of the cosmic ray particles decreases with the energy of the particle. Because these particles are the source for the atmospheric neutrino flux, the general energy dependency of the neutrino flux resembles this trend. [15]

pions decay after a very short time ($2.6 \cdot 10^{-8}$ s for $\pi^{\pm}$ and $8.52 \cdot 10^{-17}$ s for π^0 [8]) into muons, gamma and neutrinos:

$$\pi^0 \rightarrow \gamma + \gamma, \tag{2.35}$$

$$\pi^+ \rightarrow \mu^+ + \nu_\mu, \tag{2.36}$$

$$\pi^- \rightarrow \mu^- + \bar{\nu}_\mu. \tag{2.37}$$

When we take their high velocity into account ($v \lesssim c$), the half-life of the pions is increased significantly by the Lorentz boost, so $\pi^{\pm}$ would reach the Earth's surface with an kinetic energy of a few 100 GeV. Because of the longer distance through the atmosphere for horizontal particles, many pions and their secondary particles like muons have already decayed, so the neutrino flux is higher at the horizon than from the zenith (see Fig. 2.5).

Due to their lifetime of $2.2 \cdot 10^{-6}$ s and again the Lorentz boost due to their high velocity ($v \lesssim c$), muons can reach the Earth's surface causing a high background in the

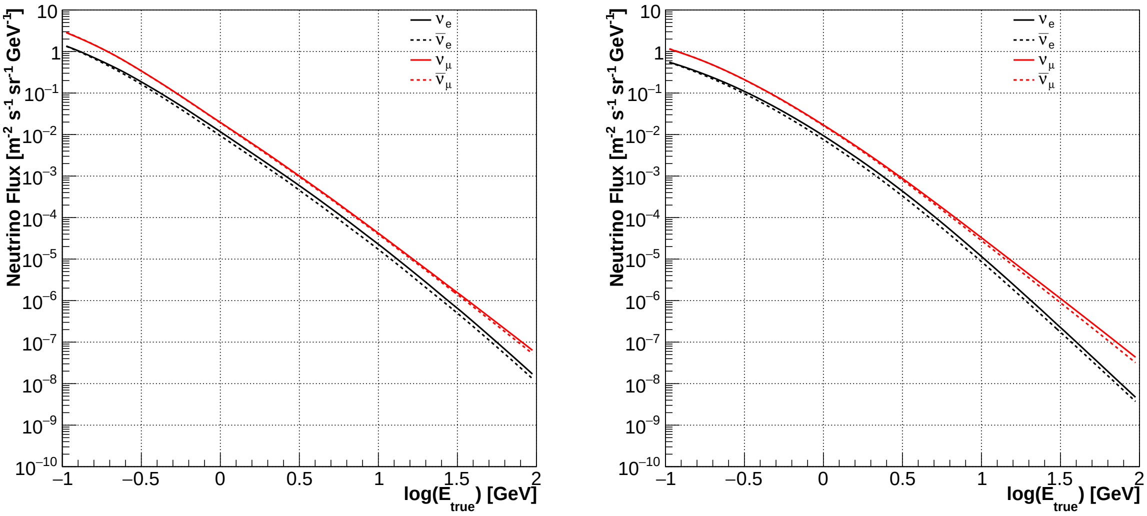

(a) $\cos\theta_{\text{true}} = -0.008$ (b) $\cos\theta_{\text{true}} = -0.342$

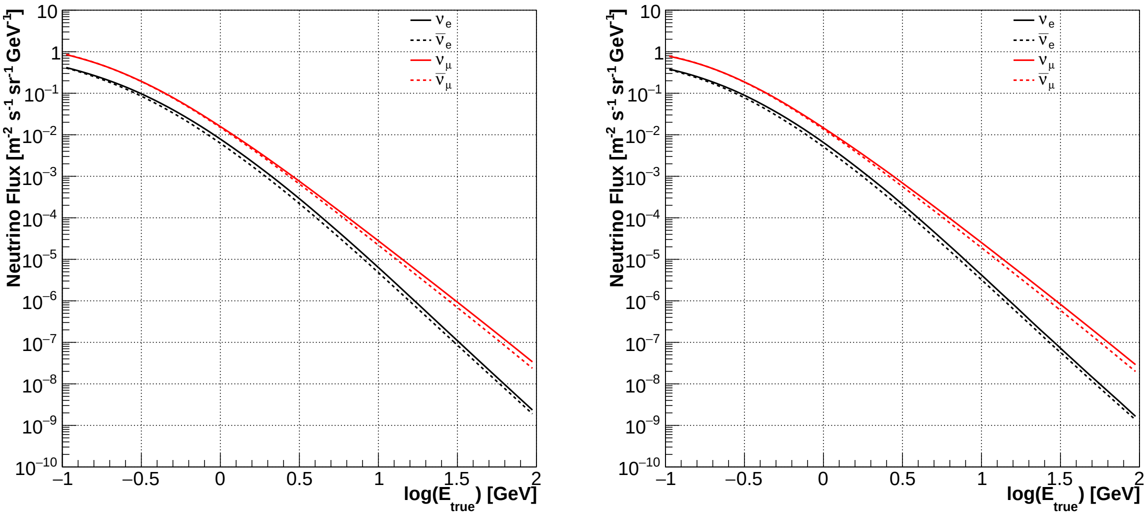

(c) $\cos\theta_{\text{true}} = -0.675$ (d) $\cos\theta_{\text{true}} = -0.992$

Figure 2.5: Atmospheric neutrino flux in units of particle per m^2 s sr GeV. As expected, the muon (anti-)neutrino flux is about twice as much as the electron (anit-)neutrino flux. They follow the same energy dependence as the cosmic ray particles. Their flux is maximal at the horizon ($\cos\theta_{\text{true}} = 0$) because the primary and secondary particles propagate a longer distance through the atmosphere and therefore have a higher probability of being decayed at the detector site. [13]

data for down-going particles. However, most of the muons, especially those with less energy and from the horizon decay on their way down to the surface:

$$\mu^+ \rightarrow e^+ + \nu_e + \bar{\nu}_\mu, \tag{2.38}$$

$$\mu^- \rightarrow e^- + \nu_\mu + \bar{\nu}_e. \tag{2.39}$$

With that we expect to measure two times more muon (anti-)neutrinos that electron (anti-)neutrinos:

$$\frac{\nu_\mu + \bar{\nu}_\mu}{\nu_e + \bar{\nu}_e} \sim 2. \tag{2.40}$$

The atmospheric neutrino flux used for sensitivity calculation can be seen in Fig. 2.5. It roughly follows the same energy dependency as the cosmic ray flux and is calculated via the Honda calculation of the neutrino flux [13].

2.3 Detection of Neutrinos

The low cross section of neutrino interactions, which allows them to propagate through Earth and the sun without a significant loss in their numbers, is also the main problem in detecting them: only a tiny fraction of neutrinos interacts with matter in the vicinity or even inside the detector. But even if a neutrino interacts, it is not automatically detected.

As we stated before, neutrinos interact only via the weak interaction, where we distinguish between NC and CC (see Fig. 2.6).

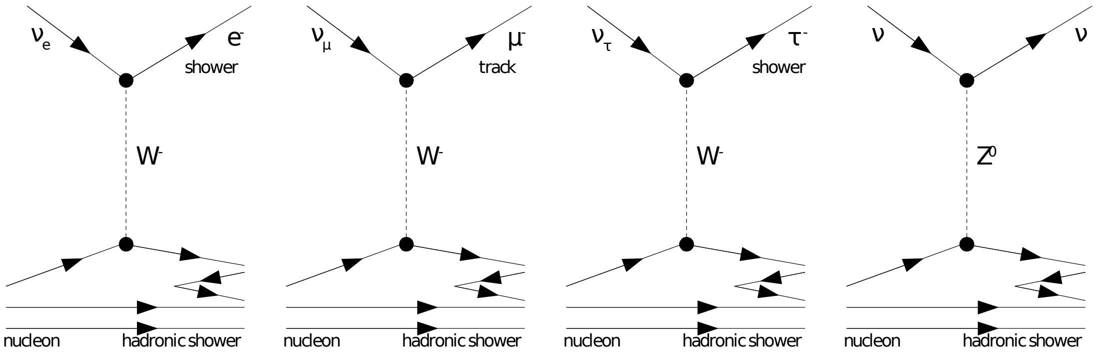

Figure 2.6: The four types of neutrino interactions: on the left, the CC interactions for all flavours are shown, the NC interaction is on the right. While all interactions produce a hadronic shower, the neutrino produced in the NC interaction disappears unseen. The electron is stopped very fast in the surrounding water, producing an electromagnetic shower. The muon propagates through the detector as a track like event. The tau has a very short lifetime and mostly decays shortly after being produced into a μ, $\bar{\nu}_\mu$ and a ν_τ, or an e, $\bar{\nu}_e$ and a ν_τ, so it can leave a electron or muon like event in the detector [8].

When it comes to detection, we distinguish two different signatures of an event: a shower and a track like event. In a track like event, only a single particle (a muon) generates Cherenkov light over a long distance (see below) and is therefore responsible for the signal in our detector. The electromagnetic shower is generated by an electron with an energy above 100 MeV which looses its energy almost entirely by bremsstrahlung. In that process, photons are emitted that mainly interact via pair production, generating an electron and an positron that can again loose energy by bremsstrahlung.

In the NC case we can only detect the hadronic shower because the secondary neutrino escapes without leaving any track. This is completely different for CC where we also have a hadronic cascade but we can also detect an electromagnetic shower of an electron or a track like event of a muon. The tau mainly decays into a muon or an electron, and therefore can look like a track and a shower like event [8].

To detect both the hadronic shower and the lepton, we exploit the fact that the particles are propagating with a velocity close to lightspeed in vacuum c. If a charged particle is propagating through a translucent medium like water or ice with a velocity larger than the speed of light in that medium, Cherenkov light is emitted in a cone around the particle (see Fig. 2.7). The opening angle θ_C of that cone is depending on the refractive index n of the surrounding medium and the velocity $\beta = v/c$:

$$\cos\theta_\mathrm{C} = \frac{1}{n\beta} \tag{2.41}$$

For water ($n \approx 1.33$) and $v \approx c$ the angle is approximately 41°.

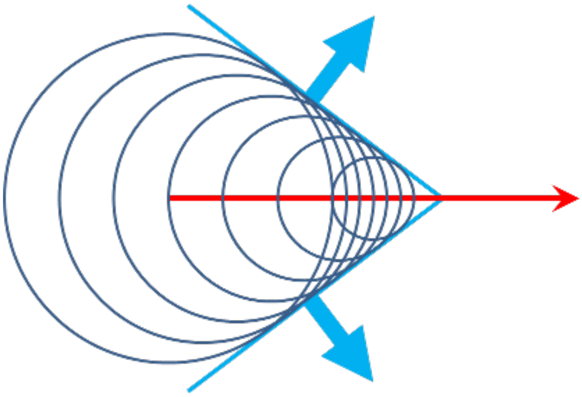

Figure 2.7: A charged particle like a muon propagates with a relativistic velocity β through a medium (red arrow), for example water, with a refraction index n. If $\beta > \frac{1}{n}$, Cherenkov light is emitted in a cone along the propagation direction with an opening angle of θ_C (blue lines). [16]

The Cherenkov photons are then to be detected by photomultipliers (PMTs) building the detector. To detect those photons, one must go deep under the surface where sun light does not produce a high background. Therefore, most neutrino detectors like ORCA are being built on the bottom of the sea, or beneath a few kilometers of ice like IceCube, while others are built in a closed reservoir like Hyper-Kamiokande [15] [27]. In KM3NeT detectors (ORCA and ARCA), 31 PMTs are arranged in a sphere called digital optical modules (DOM), to look in every direction to detect the photons [2].

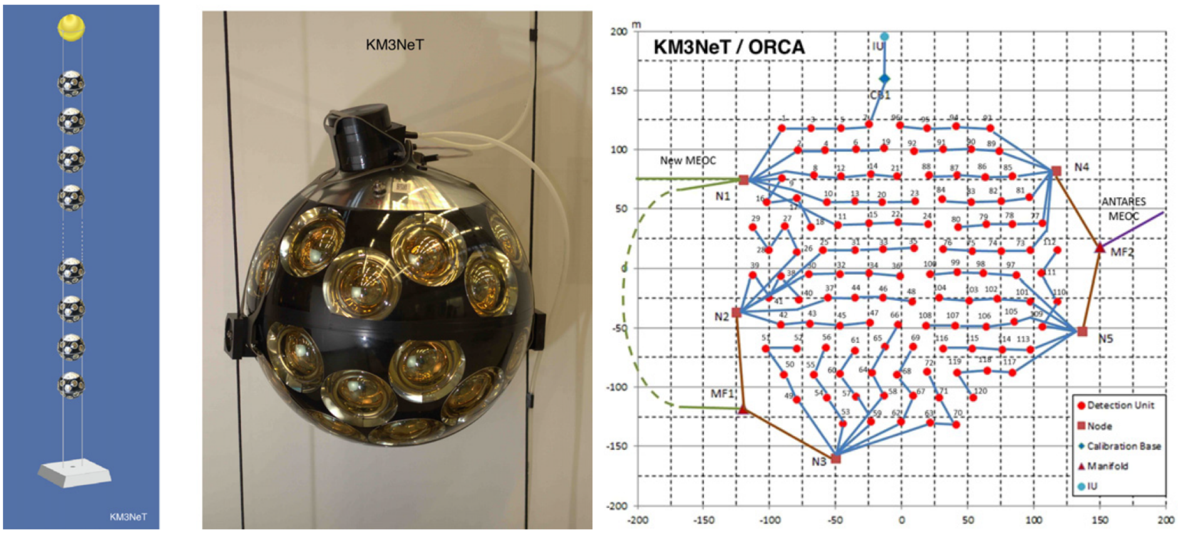

(a) Strings and DOM

(b) ORCA building block

Figure 2.8: (a) Alignment of 18 DOMs as a string, and a picture of a DOM with its 31 PMTs. (b) Layout for the ORCA building block and their connection via cables to shore. [2]

ORCA consists of one building block of 115 detection strings, each consisting of 18 DOMs. A detection string is fixed by a heavy anchor to the ground and sustained by a buoy towards the surface, and is about 200 m in height with DOMs spaced 9 m apart in vertical direction and the strings are deployed about 20 m from each other [2]. The spacing between the DOMs determines the minimum energy threshold of incoming neutrinos that can still be detected. A smaller spacing shifts that threshold to lower energies. Therefore, a hypothetical Super-ORCA could have a roughly 10 times denser arrangement, to have more sensitivity in the low energy range, which is more important for the determination of δ_{CP} than it is for NMH.

Chapter 3

Sensitivity Studies for ORCA

3.1 *paramNMH*

For all sensitivity studies, the software called *paramNMH* (version 3.0) provided by Jürgen Brunner and maintained by Liam Quinn was used. It is built on the data analysis framework **ROOT**, a C++ library used to analyse data at CERN [17]. Before we will turn to the new features we have included in this framework, we will give a quick overview of its computation chain of sensitivity studies.

3.1.1 Rate Calculation

First, we will focus on the rate calculation that is used to transform a incoming flux of neutrinos into detector dependent reconstructed events. The general idea of the evaluation is the same for ORCA and Super-ORCA, as it is the same for the atmospheric neutrino flux and a neutrino beam, although the inputs will of course be different. The hypothetical data from both ORCA and Super-ORCA will consist of observed event rates By comparing the true data with the calculated reconstructed events, done by *paramNMH*, it will be possible to derive the statistical significance to refute out a certain set of oscillation parameters. The exact implementations of the steps are given in the specific inputs in section 3.1.3 for ORCA and section 4.1.1 for Super-ORCA.

The general computing chain is shown as a flowchart in Fig 3.1 (which is designed for ORCA using atmospheric neutrino flux, but not for *paramNMH* specifically) and will be described here in detail. For further information, see the *Letter of Intent for KM3NeT 2.0* [2]. The flux and event rates to be determined are a function of the *true* neutrino energy E_{true} and the zenith angle θ_{true} and the *reconstructed* energy E_{reco} and zenith angle θ_{reco}, respectively.

At first we will attend to the detector independent part, starting with the incoming neutrino flux $\Phi_\alpha(E_{\text{true}}, \theta_{\text{true}})$ of a flavour α. For the normal sensitivity studies we use the

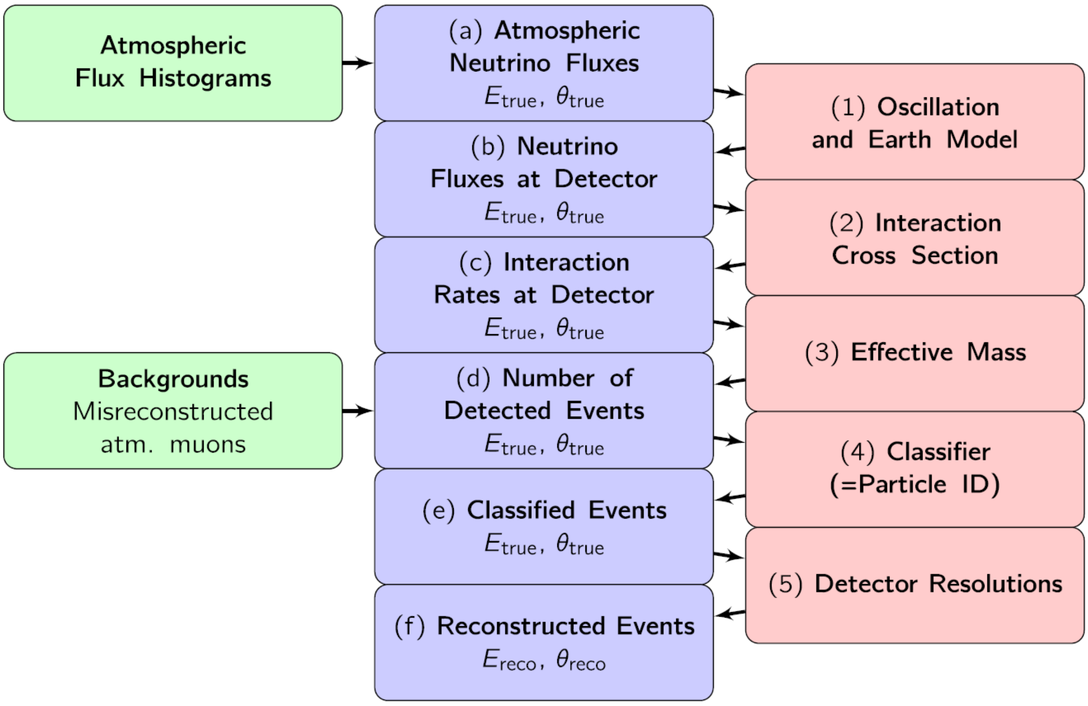

Figure 3.1: Chart for general strategy to calculate event rates: The green blocks contain external and additional inputs that do not result from any step before them. The blue blocks show the intermediate results after taking a step from all the way of the incoming flux to the final reconstructed events. The red blocks describe the steps that are executed between those results. *paramNMH* does not take the muon background into account. [2]

atmospheric neutrino flux Φ_α^{atm}, for the beam we will use an artificial flux $\Phi_\alpha^{\text{beam}}$. Note that the flavour α in this case can be ν_e, ν_μ, $\bar{\nu}_e$ and $\bar{\nu}_\mu$ because all those representatives are produced in the atmosphere and the beam generator. Tau (anti-)neutrinos are only generated by oscillation in sufficient number.

The first step in Fig. 3.1 (1) concerns the oscillation that occurs between the source of the provided neutrino flux and the detector. Note that this is still independent of any systematics of the detector. To calculate oscillations in Earth, we use *OscProb* that uses a density profile of the Earth with about 50 different density shells provided by PREM [12] and is implemented in *paramNMH*. The majority of relevant neutrinos will propagate through the Earth because of their oscillation probabilities are changed by Earth matter effects (see section 2.1.2). *OscProb* calculates the oscillation probability $P^{\text{osc}}_{\nu_\alpha \to \nu_\beta}(E_{\text{true}}, \theta_{\text{true}})$ from flavour α to flavour β (which now includes ν_τ, $\bar{\nu}_\tau$, too), depending on the true energy of the neutrino and the path through Earth which is given by the true zenith angle. The zenith angle, which is used in its cosine form for calculation, determines the different layers of Earth, as well as the propagating distance L in those shells. With equation for the oscillation probability, see section 2.1, we can calculate the oscillated neutrino flux directly at the detector site (b):

$$\Phi^{\text{det}}_{\beta}(E_{\text{true}},\theta_{\text{true}}) \;=\; \sum_{\alpha} P^{\text{osc}}_{\nu_\alpha\to\nu_\beta}(E_{\text{true}},\theta_{\text{true}}) \;\cdot\; \Phi_\alpha(E_{\text{true}},\theta_{\text{true}}). \tag{3.1}$$

For the interaction with the matter (2) in our detector, we use the GENIE event generator which gives us the charged current (CC) and the neutral current (NC) neutrino-nucleon cross sections $\sigma_\beta(E_{\text{true}})$ for an oxygen nucleus and two protons (normal water) (see Fig. 3.2) [19].

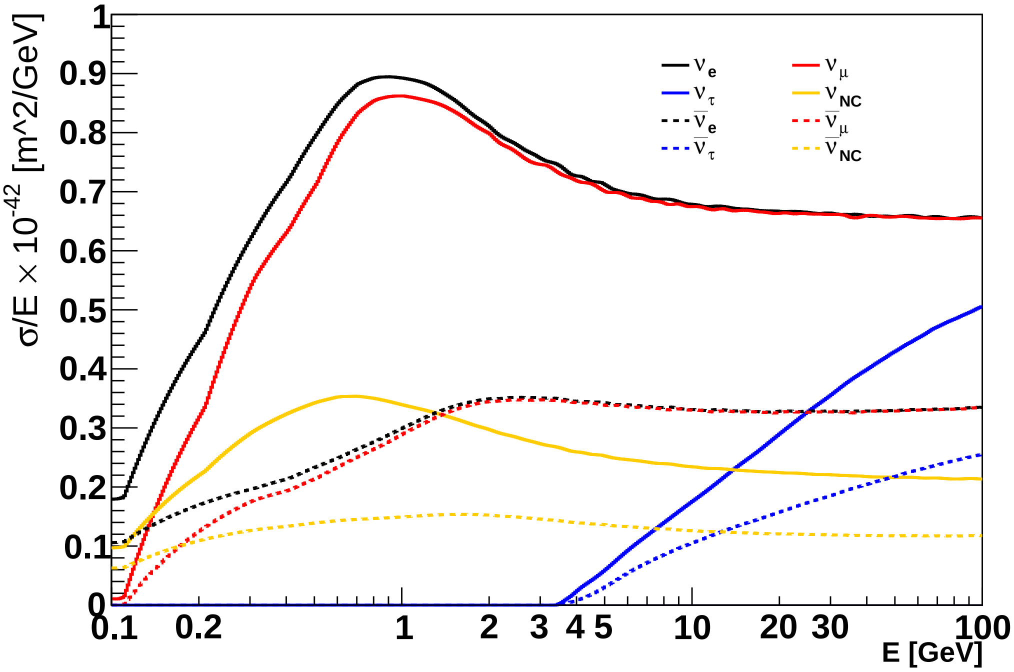

Figure 3.2: Energy-dependent cross section for all interaction types generated by GENIE [19].

With this, we get the interaction rate per unit volume at the detector site $R_\beta(E_{\text{true}},\theta_{\text{true}})$ depending on the true energy and zenith angle for a (anti-)neutrino of flavour β (intermediate result (c)).

$$R_\beta(E_{\text{true}},\theta_{\text{true}}) \;=\; \frac{\rho_{\text{water}}}{m_{\text{nucleon}}} \cdot \sum_{\alpha} \sigma_\beta(E_{\text{true}}) \cdot P^{\text{osc}}_{\nu_\alpha\to\nu_\beta}(E_{\text{true}},\theta_{\text{true}}) \cdot \Phi_\alpha(E_{\text{true}},\theta_{\text{true}}). \tag{3.2}$$

By that time we have calculated eight histograms, six for the CC interactions (three flavours, two chiralities) and two NC interactions of neutrinos and antineutrinos. The binning in all those histograms is consistent. The energy axis is linear in $\log_{10}(E_{\text{true}})$ from 2 to 100 GeV in 40 bins for ORCA and from 0.1 to 100 GeV in 60 bins for Super-ORCA (see chapter 4 for further changes). The zenith angle axis is binned linearly in $\cos\theta_{\text{zenith}}$ from -1 to 0 in 40 bins, where $\cos\theta_{\text{zenith}} = -1$ corresponds to directly up-going neutrinos coming from the nadir. However, if we take down-going neutrinos into account, we will use 80 bins and a range going from -1 to 1. For beam experiments, we will use only one bin for the zenith angle, which is given by the direction to the source. We still need the value for $\cos\theta_{\text{zenith}}$ to calculate the density profile through the Earth and the oscillation probability, but the event rates histograms become one-dimensional.

The next step (3) will be the first which is depending on the detector itself. The effective mass or better the effective volume (without ρ_{water}) can be imagined as the size of a hypothetical detector where every events can be reconstructed. Therefore, the effective mass M_{eff} determines how many of the events can be reconstructed and is depending on the neutrino energy E_{true} (version 4.0 of *paramNMH* is also adding a zenith angle dependency for the effective mass, but it is not used for the results in this thesis):

$$M_{\text{eff}} = V_{\text{gen}} \cdot \rho_{\text{water}} \cdot \frac{N_{\text{sel}}}{N_{\text{gen}}}. \tag{3.3}$$

N_{gen} is the total number of generated events in the generation volume V_{gen}, N_{sel} is the number of successfully reconstructed events, $\rho_{\text{water}} = 1025\ \text{kgm}^{-3}$ is assumed for the density of sea water.

When we are using real data, we additionally have to take misreconstructed atmospheric muons as background into account. While those events have to be removed by an effective muon veto [18], using simulations with *paramNMH* does not need this step because those wrong events due to atmospheric muons are ignored. That is why the number of detected events R_β^{det} (result (d)) is only given by:

$$R_\beta^{\text{det}}(E_{\text{true}}, \theta_{\text{true}}) = R_\beta(E_{\text{true}}, \theta_{\text{true}}) \cdot M_{\text{eff}}. \tag{3.4}$$

In step (4) the event has to be identified to be a track or shower event, the so-called *particle identification* (PID). Ideally, all CC muon interactions would be considered to be track-like events, and all other CC interactions, as well as NC interactions would be identified as shower like events (see Fig. 2.6). However, there is an energy-dependent efficiency in identifying the true event type, so that events could be misclassifiedIn that step, each of the eight histograms is splitted into two new ones, where events are identified as tracks or showers.

At last, the detector cannot measure the exact energy and zenith angle, which is why we have to apply an energy and an angular smearing. Until now, we have calculated the events depending on the true energy E_{true} and the true zenith angle θ_{true}. Now we have to smear this data to get the response of the detector, calculating the reconstructed energy E_{reco} and the reconstructed zenith angle θ_{reco}.

After the energy reconstruction (result (f) in the chart) the 16 histograms are reduced to four, by adding up the CC histograms classified as tracks and showers binwise. Additionally, all histograms of antineutrinos are added to their particular neutrino histogram, because we have no way to identify ν and $\bar{\nu}$ to separate them from each other. Thus, we get the following four histograms:

- CC interactions (all flavours, neutrinos and antineutrinos) classified as tracks
- CC interactions (all flavours, neutrinos and antineutrinos) classified as showers
- NC interactions (neutrinos and antineutrinos) classified as tracks
- NC interactions (neutrinos and antineutrinos) classified as showers

3.1.2 Sensitivity Calculation

Sensitivity calculation is done by a χ^2-fit using an Asimov data set, where every event rate per bin is set to its expectation value [20]. The idea is to calculate the median significance to reject a wrong NMH or δ_{CP} assuming another value to be correct [21]. As a starting point, we are calculating the four histograms from the rate calculation (see last section) for a certain set of oscillation parameters (neutrino mass hierarchy, mixing angles, squared mass differences, CP-violating phase) considered to be true. Each bin j, depending on E_{reco} and θ_{reco}, consists of a certain number of events $\mu^{\mathrm{true}}_{\mathrm{CC,TR},j}$, $\mu^{\mathrm{true}}_{\mathrm{CC,SH},j}$, $\mu^{\mathrm{true}}_{\mathrm{NC,TR},j}$ and $\mu^{\mathrm{true}}_{\mathrm{NC,SH},j}$.

For comparison, we have to calculate a second set of those histograms, changing one of the parameters and fixing it (for example taking another NMH), while the other parameters are fitted. With this we get "wrong" event rates, which we want to refute with a certain significance, assuming the "true" event rates. Note that the "true" histograms are simulated here as some kind of pseudo-data and can later be replaced by the true data coming from the detector.

For each bin, the "true" and "wrong" total number of track and shower events are calculated, using the following equations:

$$\begin{aligned}
\mu^{\mathrm{true}}_{\mathrm{TR},j} &= \mu^{\mathrm{true}}_{\mathrm{CC,TR},j} + \mu^{\mathrm{true}}_{\mathrm{NC,TR},j}, && (3.5)\\
\mu^{\mathrm{true}}_{\mathrm{SH},j} &= \mu^{\mathrm{true}}_{\mathrm{CC,SH},j} + \mu^{\mathrm{true}}_{\mathrm{NC,SH},j}, && (3.6)\\
\mu^{\mathrm{wrong}}_{\mathrm{TR},j} &= (\mu^{\mathrm{wrong}}_{\mathrm{CC,TR},j} + \mu^{\mathrm{wrong}}_{\mathrm{NC,TR},j} \cdot n_{\mathrm{NC}}) \cdot n_{\mathrm{TR}}, && (3.7)\\
\mu^{\mathrm{wrong}}_{\mathrm{SH},j} &= (\mu^{\mathrm{wrong}}_{\mathrm{CC,SH},j} + \mu^{\mathrm{wrong}}_{\mathrm{NC,SH},j} \cdot n_{\mathrm{NC}}) \cdot n_{\mathrm{SH}}. && (3.8)
\end{aligned}$$

n_{NC}, n_{TR} and n_{SH} are scaling factors for the event numbers for NC, track and shower events, and are later used as fit parameters to determine the overall norm, the track/shower skew and the scaling of NC events. The true value is always assumed to be 1, so we do not have to apply those factors to the "true" event rates.

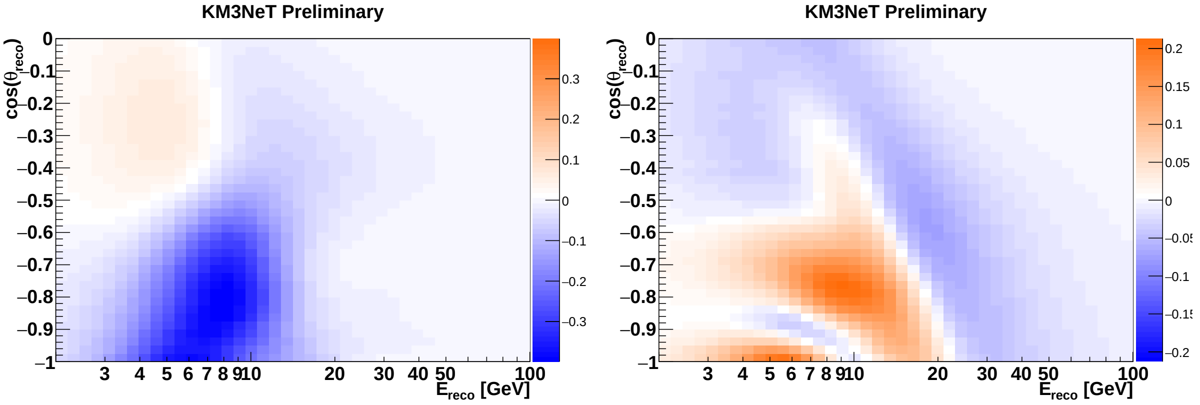

(a) $\nu_e + \bar{\nu}_e$ (b) $\nu_\mu + \bar{\nu}_\mu$

Figure 3.3: Distribution of the relative NMH differences for $\overset{(-)}{\nu}_e$-CC (a) and $\overset{(-)}{\nu}_\mu$-CC (b) after applying the resolution as a function of the reconstructed energy E_{reco} and the reconstructed zenith angle θ_{reco} after one year of data taking. The binning is the same as for the event histograms. The colour gives the statistical significance χ_j calculated for each bin j (see equating (3.11)).

These event rates are now used to define our χ^2, where we treat track and shower events individually:

$$\chi^2 = \sum_j \left(\frac{\mu^{\text{wrong}}_{\text{TR},j} - \mu^{\text{true}}_{\text{TR},j}}{\sqrt{\mu^{\text{true}}_{\text{TR},j}}} \right)^2 + \sum_j \left(\frac{\mu^{\text{wrong}}_{\text{SH},j} - \mu^{\text{true}}_{\text{SH},j}}{\sqrt{\mu^{\text{true}}_{\text{SH},j}}} \right)^2 . \qquad (3.9)$$

By adjusting the fit parameters, the event rates of the “wrong” histograms will change and the fit will try to minimize χ^2 this way, adapting the “wrong” histograms to the “true” histograms in the best way possible. This is done by the *Minuit 2* function of ROOT [22]. The square root of χ^2_{min} will then give us the statistical significance to refute the histograms due to the parameter assumed to be “wrong” (for example the NMH or δ_{CP}):

$$\sigma = \sqrt{\chi^2_{\text{min}}}. \qquad (3.10)$$

In Fig. 3.3 we can see the distreibution of the relative NMH differences for ν_e and $\bar{\nu}_e$ (left) and ν_μ and $\bar{\nu}_\mu$ (right), which mainly defines the asymmetry for showers and tracks, respectively. The colour gives the statistical significance χ_j calculated for each bin j. Here, we use χ_j instead of $\sqrt{\chi_j^2}$ so we can see the sign of the difference.

$$\chi_j = \frac{\mu_j^{\text{IH}} - \mu_j^{\text{NH}}}{\sqrt{\mu_j^{\text{NH}}}}. \qquad (3.11)$$

As we can see here, the main sensitivity comes from an energy range between 5 and 15 GeV.

Because the sensitivity is heavily dependent on θ_{23}, which is not sufficiently known, the sensitivity is calculated for different values of $\theta_{23}^{\text{true}}$ in the interval between $[40°, 50°]$. The values for the other oscillation parameters are for better comparision the same as in the Letter of Intent and therefore slightly outdated. In addition to the oscillation parameters, we use five other parameters, that are already implemented in *paramNMH* and have been used in the Letter of Intent [2]. The parameters including their priors can be see in table 3.1.

parameter	true value	prior	treatment
θ_{23} (°)	{40, 41,..., 50}	no	Fitted
θ_{13} (°)	8.42	0.26	Fitted/Fixed
θ_{12} (°)	33.4	N/A	Fixed
ΔM^2 (10^{-3} eV)	2.44	no	Fitted
Δm^2 (10^{-5} eV)	7.53	N/A	Fixed
δ_{CP} (°)	0	no	Fitted
Overall flux factor	1	0.1	Fitted
NC scaling	1	0.1	Fitted
$\nu/\bar{\nu}$ skew	0	0.03	Fitted
μ/e skew	0	0.1	Fitted
Energy slope (spectral index)	0	0.05	Fitted

Table 3.1: Standard parameters used in *paramNMH*.

While the first six parameters in table 3.1 are oscillation parameters described in chapter 2, the other parameters are implemented in *paramNMH* as followed. The overall flux factor and the μ/e skew are calculated by using the scaling factors n_{TR} and n_{SH} in equations (3.7) and (3.8):

$$\text{Overall flux factor} = \frac{n_{\text{TR}} + n_{\text{SH}}}{2}, \tag{3.12}$$

$$\mu/e \text{ skew} = \frac{n_{\text{TR}} - n_{\text{SH}}}{2}. \tag{3.13}$$

The NC scaling is equal to the scaling factor n_{NC} in equations (3.7) and (3.8). The spectral index x_{spectral} is able to suppress event rates at lower or higher energies and favour the others. The energy slope E_{slope} can be calculated by the spectral index for each energy bin, using the true energy E_{true}:

$$E_{\text{slope}} = \left(\frac{E_{\text{true}}}{E_0}\right)^{x_{\text{spectral}}}. \tag{3.14}$$

E_0 is the center of the seesaw and equals 6 GeV for ORCA. The factor E_{slope} is then multiplied with the event number for each bin.

The $\nu/\bar{\nu}$ skew f_{nunubar} is implemented as a factor directly to the flux of a certain flavour α: $\Phi^{\alpha}_{\nu/\bar{\nu}}$, so we get a slightly modified flux:

$$\Phi^{\alpha,\text{new}}_{\nu/\bar{\nu}}(E_{\text{true}}) = \Phi^{\alpha}_{\nu/\bar{\nu}}(E_{\text{true}}) \cdot (1 + \Theta^{\text{norm}}_{\nu,\bar{\nu}} \cdot f_{\text{nunubar}}). \tag{3.15}$$

$\Theta^{\text{norm}}_{\nu,\bar{\nu}}$ is 1 for ν and -2 for $\bar{\nu}$, so f_{nunubar} distinguishes between neutrinos and antineutrinos.

In table 3.1 we state that some parameters are fixed in the fit, because they do not influence the sensitivity of the detector, while others are fitted, so the chi^2 can change these parameters slightly. To prevent the fit of changing the parameters too much, we can apply priors σ_x to each parameter, by adding the following term to the calculated χ^2 for each parameter x (x_{true} is the value of x assumed to be true):

$$\frac{(x - x_{\text{true}})^2}{\sigma_x^2}$$

As we can see, assuming the NH to be true is much more dependent on the mixing angle θ_{23} than for the IH assumed to be true. Additionally, the sensitivity for $\delta^{\text{true}}_{\text{CP}} = 0°$ is significantly higher than those of $\delta^{\text{true}}_{\text{CP}} = 180°$. In the following we will assume $\delta^{\text{true}}_{\text{CP}} = 0°$ for all sensitivity studies concerning the NMH with ORCA.

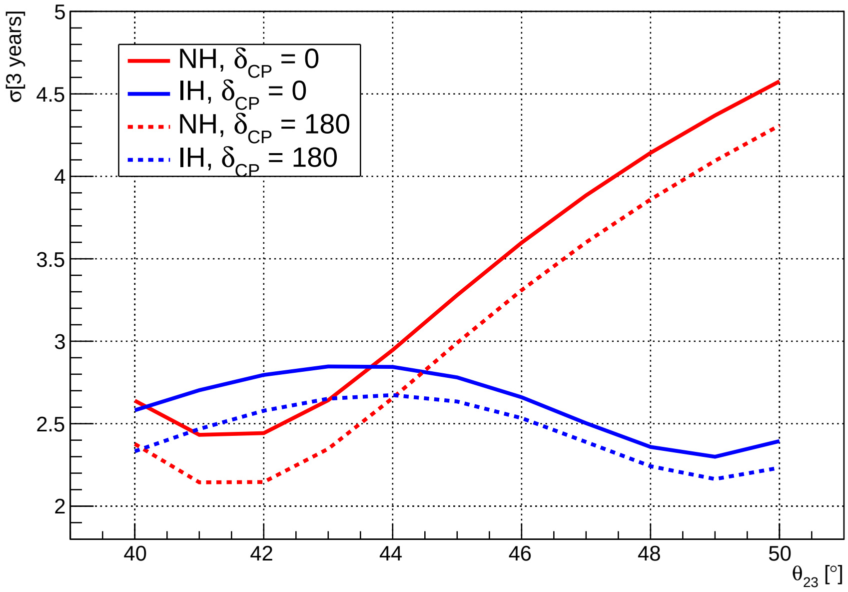

Figure 3.4: Standard *paramNMH* statistical significance for ORCA in dependency of θ_{23} for assuming NH (red) or IH (blue) to be the true hierarchy after three years of data taking. $\delta_{\text{CP}} = 0°$ for solid lines and $\delta_{\text{CP}} = 180°$ for dashed lines. The normal parameters of the Letter of Intent were used without priors.

Using the standard parameters of *paramNMH* without priors (θ_{13} is not fitted here), we define two **standard** graphs for the two different hierarchies for $\delta_{\mathrm{CP}}^{\mathrm{true}} = 0°$ and two for $\delta_{\mathrm{CP}}^{\mathrm{true}} = 180°$ (see Fig. 3.4) after three years of data taking. Here we can see that our statistical significance is heavily dependent on the mixing angle θ_{23} which is the reason we calculate the significance for different values of θ_{23}.

The red curves show the significance of refuting IH if we assume NH to be true, and vice versa for the blue lines. For NH assumed to be true, the significance has a minimum of 2.45σ (2.15σ) around $\theta_{23} = 41.5°$ for $\delta_{\mathrm{CP}} = 0°$ ($\delta_{\mathrm{CP}} = 180°$) and then increases with increasing θ_{23} up to 4.1σ (4.3σ). The IH fits have a minimum of 2.3σ (2.2σ) around $\theta_{23} = 49°$ for $\delta_{\mathrm{CP}} = 0°$ ($\delta_{\mathrm{CP}} = 180°$), but do not increase that much for smaller values of θ_{23} (maximum of 2.85σ (2.7σ) for $\theta_{23} = 44°$). In both cases (NH and IH), the significance is always better for $\delta_{\mathrm{CP}} = 0°$ and $\delta_{\mathrm{CP}} = 180°$, which are the two possible values for preserving the CP-symmetry.

3.1.3 ORCA-specific Inputs

While the energy and sometimes zenith angle-dependent input data (see green and red boxes in Fig. 3.1) are determined by different software, *paramNMH* uses parametrisations that have been fitted on the original simulated data. While the cross section and the atmospheric flux are given in a list of data and the fit-software interpolates in between, the effective mass, PID and resolution are given by equations that are shown in this section. Each of them have certain parameters that are evaluated by fitting the approximation functions to the software's data for each of the eight interactions.

The here presented formulas are used for ORCA and have been originally implemented in *paramNMH*, using the same data as in the Letter of Intent [2]. The values of the parameters can be found in table A.1 in the appendix. The Super-ORCA implementation will be shown later in section 4.1.1.

The effective mass for ORCA is calculated by the following equation:

$$M_{\mathrm{eff}}(E_{\mathrm{true}}) = \begin{cases} N_{\mathrm{Meff}} \cdot \tanh\left(\frac{E_{\mathrm{true}}-E_{\mathrm{min}}}{\sigma_{\mathrm{Meff}}}\right) & \text{if } E_{\mathrm{true}} > E_{\mathrm{min}}, \\ 0 & \text{if } E_{\mathrm{true}} \leq E_{\mathrm{min}}, \end{cases} \tag{3.16}$$

where E_{min} is the lower energy threshold for the effective mass of a certain interaction, σ_{Meff} describes the slope, and N_{Meff} the normalisation, which gives the maximum effective mass for a neutrino interaction type. The effective masses for ORCA in the typical range from 2 GeV to 100 GeV can be seen in Fig. 3.5 (a).

The effective mass therefore is zero below a minimum energy, which means that all neutrinos with an energy below that threshold cannot be detected by the detector because too few photons hit the PMTs. With increasing energy the effective mass increases with a steepness defined by the slope σ_{Meff} , until it reaches its maximum value and goes to saturation at N_{Meff}.

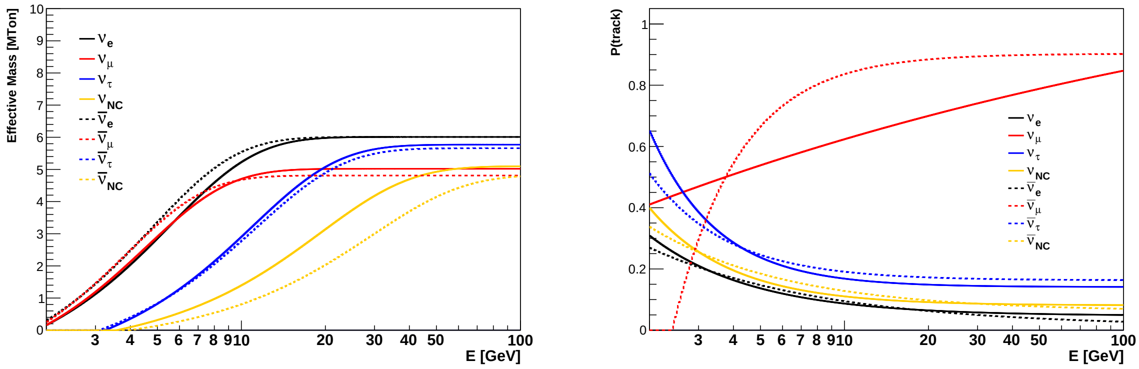

(a) Energy-dependent effective mass

(b) Energy-dependent PID

Figure 3.5: Effective mass (a) and PID (b) as function of energy for all interaction types for ORCA.

The PID, more specifically the probability to classify an event as a track P_{track}, is calculated in *paramNMH* by the following equation in *paramNMH*, while x_0, x_1 and x_2 are determined for all different interactions:

$$P_{\text{track}}(E_{\text{true}}) = x_0 + x_1 \cdot E_{\text{true}}^{-x_2}. \tag{3.17}$$

The possibility of classifying an event as a shower is given by $P_{\text{shower}} = 1 - P_{\text{track}}$.

As it is shown in Fig. 3.5 (b), the classification in the high energy limit is quite accurate, classifying true track events ($\overset{(-)}{\nu}_\mu$-CC) as tracks, and true shower events mainly as showers. On the other hand, the detected muons and especially antimuons are misclassified in the low energy limit, due to their lack of kinetic energy, while the shower events are misclassified as track events more often. However, the effective mass in that energy range is very low, so that effect is limited. The difference between the PID ν_μ-CC and $\bar{\nu}_\mu$-CC can be explained by different behaviour of the cross section for neutrinos and antineutrinos with respect to the Bjorken y. The lepton track and the hadronic shower can be easily identified for the muon channel, so we can see the the effect of the y better than in the other channels [2].

The energy resolution is dependent on the true energy E_{true} and essentially a smearing of the measured event numbers by a normal distribution. So the number of events calculated for a particular true energy is distributed into all energy bins available, using a given mean $\bar{E}$ and a standard deviation σ_{resol}:

$$\bar{E}(E_{\text{true}}) = E_{\text{true}} \cdot \left(m_0 + m_1 \cdot \log \frac{E_{\text{true}}}{\text{GeV}} + m_2 \cdot \left(\log \frac{E_{\text{true}}}{\text{GeV}} \right)^2 \right), \tag{3.18}$$

$$\sigma_{\text{resol}}(E_{\text{true}}) = s_0 + s_1 \cdot E_{\text{true}} + s_2 \cdot E_{\text{true}}^2. \tag{3.19}$$

m_0, m_1, m_2, s_0, s_1 and s_2 are parameters given for each type of interaction.

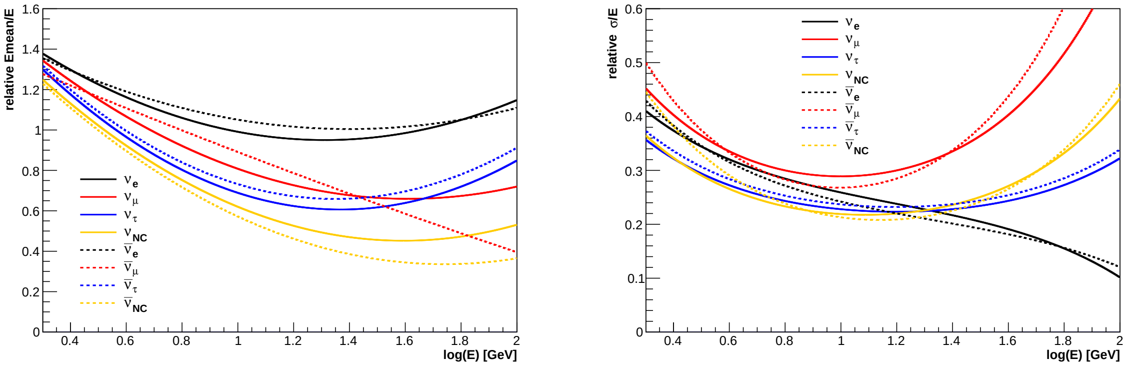

(a) $\bar{E}/E_{\mathrm{true}}$ (b) $\sigma_{\mathrm{resol}}/E_{\mathrm{true}}$

Figure 3.6: (a) relative mean energy in dependency of the true energy for all interaction types for ORCA. (b) relative standard deviation in dependency of the true energy for all interaction types for ORCA.

In Fig. 3.6 (a) the relative mean energy $\bar{E}/E_{\mathrm{true}}$ is shown for all different interaction channels. While the events are shifted to higher energies for ν_e and $\bar{\nu}_e$, the events for all other interactions are mainly shifted to lower energies. Note that this shift is done after applying the effective mass and the cross section, which is the reason why we have for example ν_τ events for energies lower than the rest mass of τ. Fig. 3.6 (b) shows the relative standard deviation $\sigma_{\mathrm{resol}}/E_{\mathrm{true}}$: While the resolution for electron neutrinos and antineutrinos is getting better for increasing energy, all other interactions have their best resolution between 6 and 15 GeV, which is only slightly above the interesting energy range for NMH determination. $\overset{(-)}{\nu}_\mu$-CC have the worst resolution, because the energy of an event is determined by the overall light that has been measured in the detector. Because $\overset{(-)}{\nu}_\mu$-CC are track like events, the generated muon often leaves the detector before loosing all its kinetic energy. The detector only sees a fraction of the true energy of the muon, while the rest is leaving the detector with the muon. This effect becomes stronger with increasing energy.

The energy after the smearing is then called the reconstructed energy E_{reco}. Figure 3.7 shows here are the energy resolution histograms for neutrinos (antineutrinos are shown in the appendix, see Fig. A.1). These histograms are calculated once and are not changed by any oscillation parameter. When the energy scale parameters are used, the fit is interpolating between the bins to extract the energy resolution for the changed energy (see section 3.2.1). Again, it can be seen that $\sigma_{\mathrm{resol}}/E$ is minimal at high energies for ν_e and $\bar{\nu}_e$ and that many events are shifted to lower energies for all other interactions.

The angular resolution is dependent on both true energy E_{true} and true zenith angle $\cos\theta_{\mathrm{true}}$. θ_{true} is the true zenith angle, the neutrino enters the detector, while θ_{reco} is the reconstructed zenith angle. θ_{dist} is the angle between the true neutrino direction on the sphere and the reconstructed one, which is not necessarily parallel to the meridian. To

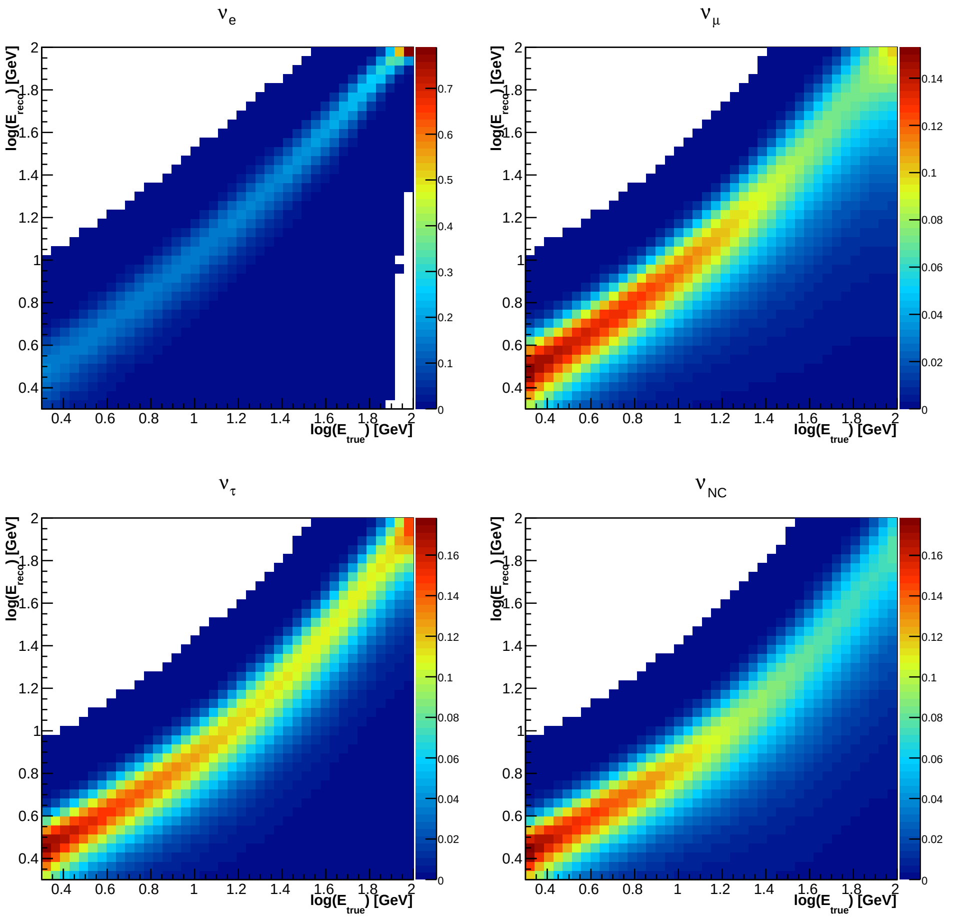

Figure 3.7: Energy resolution E_{reco} in dependency of the true energy for all neutrino interaction types for ORCA.

calculate θ_{reco}, we use a normal distribution of $\cos\theta_{\text{dist}}$ around the meam value $\cos\theta_{\text{true}}$. The standard deviation $\sigma_{\cos}$ for this normal distribution is calculated using only one parameter x_{med}, different for each type of interaction:

$$\sigma_{\cos}(E_{\text{true}}) \;=\; 0.74 \;\cdot\; \left| x_{\text{med}}^2 \cdot \frac{10}{E_{\text{true}}} \right|. \tag{3.20}$$

As it can be seen in Fig. 3.8 the standard deviation is high for lower energies, which is not so important because the detector isn't sensitive at low energies expressed by the effective detector mass.

After the calculation of $\cos\theta_{\text{dist}}$, the cosine of the zenith angle after applying the resolution $\cos\theta_{\text{reco}}$ is calculated by the following equation:

$$\cos\theta_{\text{reco}} \;=\; \cos\alpha \cdot \sin\theta_{\text{true}} \cdot \sin\theta_{\text{dist}} \;+\; \cos\theta_{\text{true}} \cdot \cos\theta_{\text{dist}}. \tag{3.21}$$

α is called the course angle which defines the angle of the shift between the true and the reconstructed neutrino direction in respect to the meridian. For the calculation, 30

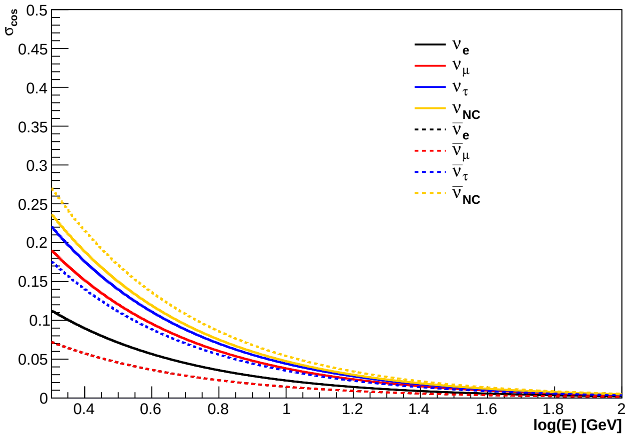

Figure 3.8: Energy-dependent angular resolution $\sigma_{\cos}$ for all interaction types for ORCA.

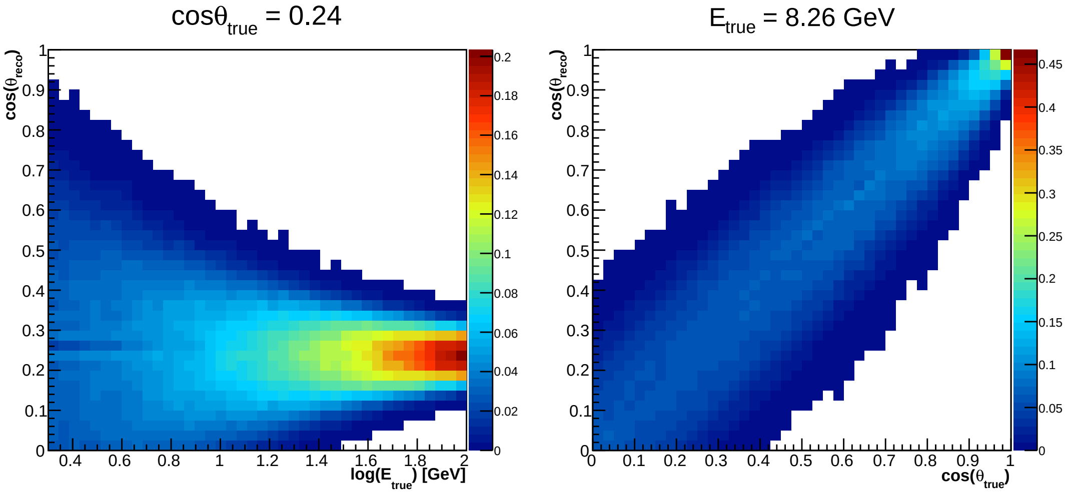

Figure 3.9: Angular resolution for ν_e for ORCA: left: $\cos\theta_{\mathrm{reco}}$ in dependency of E_{true} for $\cos\theta_{\mathrm{true}} = 0.24$; right $\cos\theta_{\mathrm{reco}}$ in dependency of $\cos\theta_{\mathrm{true}}$ for $E_{\mathrm{true}} = 8.26$ GeV. The z-axis is giving the ratio of the smearing in a certain bin of $\cos\theta_{\mathrm{reco}}$ depending on the values of E_{true} and $\cos\theta_{\mathrm{true}}$.

different values of α between 0 and π are sufficient. For further information on calculating $\cos\theta_{\mathrm{reco}}$, see [23], although we here use a nadir based system instead of a system centred around the zenith.

Because the angular resolution is depending on the true energy and the true zenith angle, the angular resolution for one interaction type is saved in a three-dimensional histogram. Shown in Fig. 3.9 are two slices of the histogram for ν_e: on the left hand side, the energy-dependent resolution ratio for $\cos\theta_{\mathrm{true}} = 0.24$ is shown, while on the right hand side, we can see the zenith angle-dependent resolution ratio for the energy $E_{\text{true}} = 8.26$ GeV. The artefact in the left picture between $\cos\theta_{\text{true}} = 0.2$ and 0.3 for low energies is a result of the low number of 30 for the course angle α for ORCA. However, the effect has no significant influence, so the low number is sufficient enough and saves time. For Super-ORCA this number has to be increased to avoid an even stronger effect.

It is clearly visible that $\cos\theta_{\text{reco}}$ is normally distributed around $\cos\theta_{\text{true}}$ when we take a look at the left picture. However, if we take a closer look at the distribution for $\cos\theta_{\text{true}} = 0.9625$, we can the maximum is not in the bin for $\cos\theta_{\text{reco}} = 0.9625$ but in the pole bin for $\cos\theta_{\text{reco}} = 0.9875$. This is an effect that occurs due to the usage of spherical coordinates and will be even stronger for Super-ORCA at lower energies.

3.2 New Set of Systematics

In addition to the parameters originally provided by the software, we have implemented a set of new parameters. Additional parameters help us to take more systematics into account and provide a better representation of the reality. Of course, more parameters will also mean that we have more fit possibilities and therefore a better chance to fit the wrong hierarchy to the true hierarchy's pseudo data, which will become noticeable by a decreasing sensitivity.

All those parameters used will be motivated and their implementation will be described in this section, as well as the priors we chose for them. For ORCA we have three major groups of new parameters: many of them have an influence on the energy scale, while a few effect the PID, and the last group of parameters can be described as flux-depending parameters.

The parameters for energy scale and flux are implemented as additional factors in the main calculation, while the PID parameters are implemented directly into the formula of the probability calculation to classify an event as a track. Because we are using a different formula for Super-ORCA, the PID parameters only apply to ORCA, while energy scale and flux parameters work in the same way for both experiments.

3.2.1 Systematics for the Energy Scale

The real detector will probably under- or overestimate the produced luminance by μ, e and hadronic showers. This systematic comes from a wrongly calibrated photon detection efficiency which is inevitable. To include this systematic, we distinguish between the true energy of the incoming neutrino E_ν, and the energy E_{detector} that is assigned to the event by the measurement, due to the luminance and the calibration of the detector.

The new energy E_{detector} is only used by steps completely dependent on the detector, such as the calculation of the effective mass and the smearing of the energy and angular resolution. All other steps concerning the physics without the detector will use the true energy of the neutrino, such as the calculation of the oscillation and the determination of the flux at a certain energy. The PID will also use E_ν.

The two formulas used to calculate E_{detector} for the NC and the CC interactions are given here:

$$\begin{aligned}\text{NC}: \quad E_{\text{detector}} &= E_\nu \cdot e_{\text{Escale}} \cdot [1 + e_{\text{EscNC}} \\ &\qquad + (\Theta_{\text{up}} \cdot e_{\text{Escctup}} + \Theta_{\text{down}} \cdot e_{\text{Escctdown}}) \cdot \cos\theta_{\text{zenith}}], \quad (3.22)\\ \text{CC}: \quad E_{\text{detector}} &= E_\nu \cdot e_{\text{Escale}} \cdot [1 + \Theta_{\nu,\overline{\nu}} \cdot \Theta_{(e,\mu),\tau} \cdot e_{\text{Escnu}} + \Theta_{e,\mu} \cdot e_{\text{Escemu}} + \Theta_\tau \cdot e_{\text{Esctau}} \\ &\qquad + (\Theta_{\text{up}} \cdot e_{\text{Escctup}} + \Theta_{\text{down}} \cdot e_{\text{Escctdown}}) \cdot \cos\theta_{\text{zenith}}]. \quad (3.23)\end{aligned}$$

The first parameter e_{Escale} is an overall scaling factor between the neutrino energy and E_{detector} and does not depend on any other input, like flavour, chirality or the zenith angle. Whether we look at NC interaction or a CC interaction of ν_e or $\bar{\nu}_\tau$, this factor will apply to all in the same way.

In contrast to the first parameter with a standard value of 1, all other factors are implemented as skews and therefore their standard value is 0. In the NC interaction we introduce e_{EscNC} as a factor that takes the difference between NC and CC into account. Due to the implementation in the NC case only, the CC interactions are set as being normal and the NC interaction is shifted compared to that normal value. The main reason for using that parameter is again the possible different light generation between the two types of interaction.

parameter	true value	prior	interpretation
e_{Escale}	1	3 %	overall norm
e_{EscNC}	0	5 %	ratio between NC and CC
e_{Escnu}	0	3 %	ratio between ν and $\overline{\nu}$
e_{Escemu}	0	3 %	ratio between electron and muon flavour
e_{Esctau}	0	5 %	ratio of tau flavour to all other interactions
e_{Escctup}	0	3 %	dependency on $\cos\theta_{\text{zenith}}$ for upgoing neutrinos
$e_{\text{Escctdown}}$	0	3 %	dependency on $\cos\theta_{\text{zenith}}$ for downgoing neutrinos

Table 3.2: Energy scale parameter with their priors and their interpretation.

In the CC case we have three other skews to add more systematics. First, e_{Escnu} describes the different different detector responses to the energy due to the chirality: here, $\Theta_{\nu,\overline{\nu}}$ equals 1 for neutrinos and −1 for antineutrinos. Because of the uncertainties in the tau-family, we only take $\overset{(-)}{\nu}_e$ and $\overset{(-)}{\nu}_\mu$ into account, using $\Theta_{(e,\mu),\tau}$ equals 1 for electron and muon flavour, and 0 for tau flavour.

To describe the energy changes depending on the difference of the main flavour types e and μ, we use the new parameter e_{Escemu}, where $\Theta_{e,\mu}$ equals 1 for $\overset{(-)}{\nu}_e$, −1 for $\overset{(-)}{\nu}_\mu$ and 0 for $\overset{(-)}{\nu}_\tau$. With those we deal with another skew called e_{Esctau}, which is activated only for $\overset{(-)}{\nu}_\tau$ due to the factor Θ_τ, which equals 1 for $\overset{(-)}{\nu}_\tau$ and 0 for everything else.

Furthermore, we have two more parameters dealing with a zenith angle dependency θ_{zenith}, or rather on the cosine of that angle. The prefactor Θ_{up} equals 1 for up-going $\overset{(-)}{\nu}$ and 0 for down-going $\overset{(-)}{\nu}$, while the factor Θ_{down} behaves the other way around. With that, e_{Escctup} applies only to up-going, $e_{\text{Escctdown}}$ only to down-going neutrinos. Note that the skew defined by those parameters is always zero for $\cos\theta_{\text{zenith}} = 0$, so for horizontal incoming neutrinos.

Because of the construction of the detector is still in progress, we do not know the exact systematic uncertainties. Therefore we had to do some estimations for the priors that could be applied to the parameters (see table 3.2).

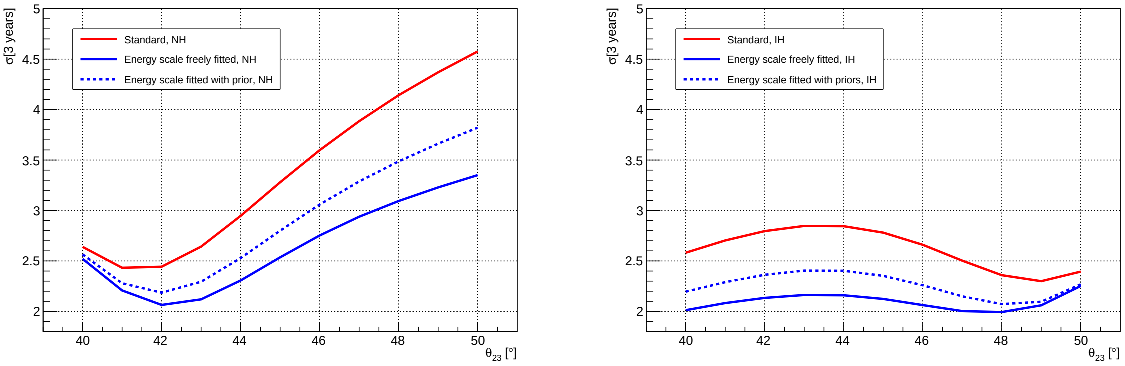

(a) NMH = NH

(b) NMH = IH

Figure 3.10: Influence of the energy scale parameter: red is the standard fit (see Fig. 3.4); the solid/dashed blue line is the fit including all new energy scale parameters without/with their priors.

Note that e_{Escnu} and e_{Escemu} are implemented as differences, so when for example $e_{\text{Escnu}} = 0.01$, E_{detector} will be increased by 1% for neutrinos and decreased by 1% for antineutrinos. The priors given in table 3.2 are the priors on the ratio between ν and $\overline{\nu}$ or the ratio between electron and muon flavour.

In Fig. 3.10 we can see the effect of the new energy scale parameters compared to the standard fit from Fig. 3.4 using the original parameters without their priors applied in *paramNMH*. The general form of the curve is preserved, but as expected, the statistic significance decreases due to the fact that we have more parameters for the fit that can be adjusted by the minimization. Depending on the mixing angle θ_{23}, the sensitivity loss due to the new parameters is very different for normal hierarchy assumed to be true (a): for small values of θ_{23} the loss in sensitivity is very small, but for higher θ_{23} the sensitivity decreases by more than 1σ. The minimum statistical significance is equal to

2.1σ for $\theta_{23} = 42°$, the maximum is equal to 3.3σ for $\theta_{23} = 50°$. For the inverted hierarchy assumed to be true, it is the other way around: the statistic significance decreases for small values of θ_{23} by 0.6σ and by 0.15σ for $\theta_{23} = 50°$. The minimum statistical significance is equal to 2.0σ for $\theta_{23} = 40°$ and 48°, the maximum is equal to 2.25σ for $\theta_{23} = 50°$.

Of course, constraining the parameters with their uncertainties by using priors decreases the sensitivity loss in both cases. However, the uncertainties for the energy scale are just educated guesses and are not based on determined values. Therefore, with more smaller uncertainties and stronger priors coming with that, the sensitivity loss could be limited even more. For NH and $\theta_{23} = 50°$, the sensitivity loss is decreased by 0.5σ while it is smaller for smaller θ_{23}. For IH, the sensitivity loss is decreased by 0.2σ for θ_{23} between 40° and 47°.

There is no single new parameter that dominates the others, though e_{EscNC}, e_{Escnu} and e_{Esctau} seem to have the largest impact. Example values for the fits can be seen in the appendix for NH, $\theta_{23} = 49°$ in table A.2 and for IH, $\theta_{23} = 44°$ in table A.3.

3.2.2 Systematics for the Particle ID

For ORCA we use the parametrisation shown in eq. (3.17) for the PID. The new parameters for PID are now implemented in this formula by the following way:

$$\begin{aligned} P_{\mathrm{track}} &= x_0 \cdot (1 + \Theta_{\nu,\bar{\nu}} \cdot p_{\mathrm{nuanu0}} + \Theta_{\mathrm{track,shower}} \cdot p_{\mathrm{trsh0}}) \\ &\quad + x_1 \cdot (1 + \Theta_{\nu,\bar{\nu}} \cdot p_{\mathrm{nuanu1}} + \Theta_{\mathrm{track,shower}} \cdot p_{\mathrm{trsh1}}) \cdot E_{\nu}^{-x_2}. \end{aligned} \tag{3.24}$$

$\Theta_{\nu,\bar{\nu}}$ again equals 1 for neutrinos and -1 for antineutrinos, so p_{nuanu0} and p_{nuanu1} are defined as a skew for the chirality for x_0 and x_1, respectively. $\Theta_{\mathrm{track,shower}}$ equals 1 for ν_μ and $\bar{\nu}_\mu$ and -1 for all other interactions. Therefore, the parameters p_{trsh0} and p_{trsh1} mimic a different behaviour between real track events and real shower events for x_0 and x_1, respectively.

There is no need for assigning similar parameters to x_2 as well, because they would be strongly correlated to the new parameters of x_1. Note that the energy used to calculate P_{track} is always E_ν and not E_{detector}.

Like for the energy scale parameter, we do not know the uncertainties before the detector has been built and further studies have determined the PID, so we have assumed two sets of priors. Those priors are assigned to all four new parameters similarly:

priors = 2.5 %
priors = 5 %

By definition, all parameters are set to 0 if not used.

In Fig. 3.11 the effect of the new PID parameters is shown, again compared to the standard *paramNMH* parameters without priors from Fig. 3.4. The sensitivity loss without using the PID priors is similar to that of using the energy scale parameters without priors (see solid blue line in Fig. 3.10) for both hierarchies. For NH the loss in

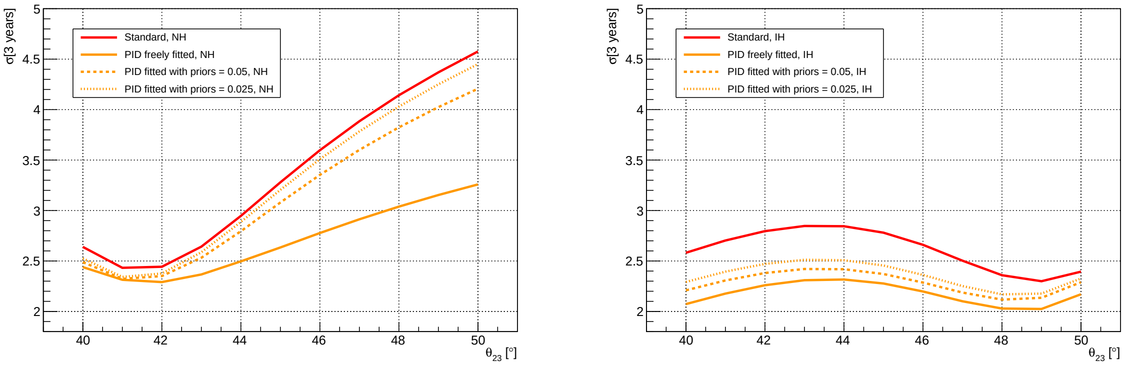

(a) NMH = NH (b) NMH = IH

Figure 3.11: Influence of PID parameters on the sensitivity: red is the standard fit (see Fig. 3.4); the solid orange line is the fit including all new PID parameters without their priors; dotted and dashed lines are fitted with prior = 2.5% and prior = 5% for the PID parameters, respectively.

statistical significance is equal to 0.15σ for $\theta_{23} = 41°$ and roughly 1.3σ for $\theta_{23} = 50°$. For IH the loss in statistical significance is relatively constant for $\theta_{23} = 40°$ to $46°$ with 0.5σ and minimal (0.2σ) for $\theta_{23} = 50°$.

By applying the priors to the fit, the sensitivity loss for NH decreases significantly. Like those for the energy scale, the applied priors are estimated and not taken from some determined values. For further analysis, the 5% prior will be used. For IH assumed to be true, however, the priors show smaller effects than for NH by far. For NH, the statistical significance loss is equal to 0.15σ for $\theta_{23} = 40°$ and 0.4σ (0.15σ) for $\theta_{23} = 50°$ and prior=5% (2.5%). For NH, the statistical significance loss is equal to 0.4σ (0.3σ) for $\theta_{23} = 40°$ and prior=5% (2.5%), and 0.1σ for $\theta_{23} = 50°$ and both prior sets.

The dominating parameter is the energy-dependent skew for $\nu/\bar{\nu}$, called p_{nuanu1}. This parameter is running away by almost 25 % for $\theta_{23} = 49°$ (NH) in the fit without priors (solid orange line in Fig. 3.11 (a)). This effect can be seen in Fig. 3.12. While the probability of classifying an electron neutrino CC event as a track event is increased, the probability for electron antineutrinos is decreased by nearly the same amount (a). For muon neutrinos and antineutrinos it is the other way around (b). Although the changes in PID are not so large, the sensitivity loss is high. Example values for the fits can be seen in the appendix for NH, $\theta_{23} = 49°$ in table A.4 and for IH, $\theta_{23} = 44°$ in table A.5.

3.2.3 Systematics for the Flux

The flux parameters are applied directly to the unoscillated flux $\Phi^{\alpha}_{\nu/\bar{\nu}}(E)$ as skews, where α is the flavour of the (anti-)neutrino. Because we are interested in flux uncertainties

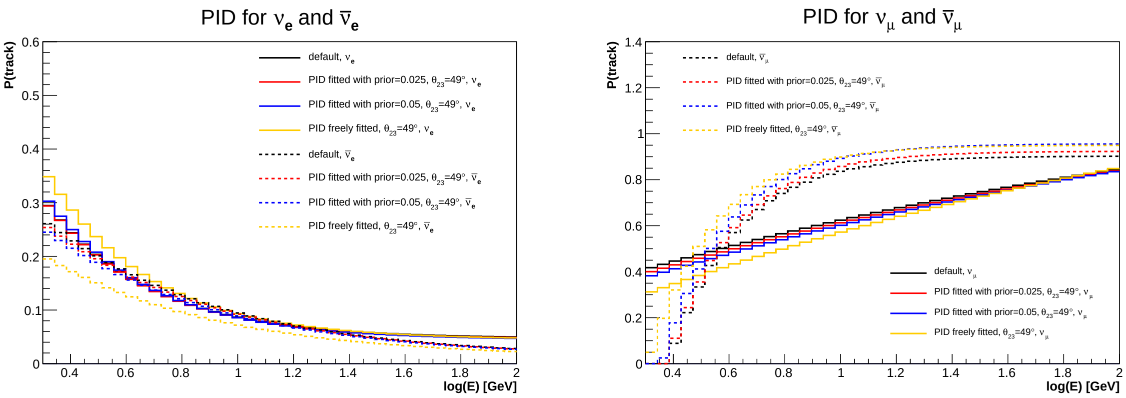

(a) ν_e & $\bar{\nu}_e$

(b) ν_μ & $\bar{\nu}_\mu$

Figure 3.12: Change of PID due to the four PID parameter values determined by the fit for $\theta_{23} = 49°$ (NH) for the fit without priors (yellow), with Prior 1 (blue), Prior 2 (red) and the default values (black). The solid lines are used for neutrinos and the dashed lines are used for antineutrinos. The binning here is the same as used in the fit. (a) for electron flavour and (b) for muon flavour.

of the incoming flux before oscillation, we are only looking at electron and muon (anti-)neutrinos. These parameters are added in addition to f_{nunubar} which describes the overall skew between neutrinos and antineutrinos in the original version of *paramNMH* (see section 3.1.2). Note that these parameters do not preserve the total flux.

$$\begin{aligned}\Phi^{\alpha,\text{new}}_{\nu/\bar{\nu}}(E) =& \Phi^{\alpha}_{\nu/\bar{\nu}}(E) \cdot \Big[1 + f_{\text{Fluxct1}} \cdot |\cos\theta_{\text{zenith}}| + f_{\text{Fluxct2}} \cdot \cos^2\theta_{\text{zenith}} + f_{\text{Fluxemu}} \cdot \Theta_{e,\mu} \\ &+ \Theta^{\text{norm}}_{\nu,\bar{\nu}} \cdot \left(f_{\text{nunubar}} + f_{\text{nunubarct}} \cdot |\cos\theta_{\text{zenith}}| + \left(\frac{E_\nu}{E_0}\right)^{f_{\text{nunubarE}}} - 1 \right)\Big]. \quad (3.25)\end{aligned}$$

Because the atmospheric neutrino flux differs significantly for different values of $\cos\theta_{\text{zenith}}$, the first two parameters f_{Fluxct1} and f_{Fluxct2} focus on the overall flux (equally for each flavour and chirality). The next parameter f_{Fluxemu} is focusing on the difference between the incoming electron flavour and muon flavour flux, where $\Theta_{e,\mu}$ is 1 for $\overset{(-)}{\nu}_e$, and -1 for $\overset{(-)}{\nu}_\mu$.

Like f_{nunubar}, the other parameters are focusing on the difference between neutrino and antineutrino flux. For this, $\Theta^{\text{norm}}_{\nu,\bar{\nu}}$ is 1 for neutrinos and -2 for antineutrions. While f_{nunubar} is the overall parameter for this skew, $f_{\text{nunubarct}}$ takes the zenith angle into account, and f_{nunubarE} is dependent on the neutrino energy E_ν. E_0 is again the centerpoint for the seesaw-like dependency and equals the centerpoint of the seesaw used for the spectral index (see section 3.1.2).

In addition we have two more parameters, which are not applied directly to the unoscillated, incoming flux, but on the calculated events per energy and zenith angle. Both are used to describe a difference between events classified as track or shower, one depend-

parameter	prior	source	interpretation
f_{Fluxct1}	2 %	Fig. 9 of [24]	dependency on $\cos\theta_{\text{zenith}}$
f_{Fluxct2}	2 %	Fig. 9 of [24]	dependency on $\cos^2\theta_{\text{zenith}}$
f_{Fluxemu}	1 %	Fig. 7 of [24]	ratio between electron and muon flavour
f_{nunubar}	3 %	Fig. 8b of [24]	overall skew for ratio between ν and $\overline{\nu}$
$f_{\text{nunubarct}}$	3 %	Fig. 8b of [24]	$\cos\theta_{\text{zenith}}$ depending skew for ratio between ν and $\overline{\nu}$
f_{nunubarE}	0.7	Fig. 7 of [24]	energy depending skew for ratio between ν and $\overline{\nu}$ (power law)
f_{TrShct}	0.5 %	Fig. 8b of [24]	$\cos\theta_{\text{zenith}}$ depending skew for ratio between track and shower
f_{TrShE}	0.5	Fig. 7 of [24]	energy depending skew for ratio between track and shower (power law)

Table 3.3: Flux parameters with their priors and their interpretation.

ing on the $\cos\theta_{\text{zenith}}$ (f_{TrShct}), the other on the neutrino energy E_ν (f_{TrShE}). Since they act as changing the norm, they can be seen as a flux parameter, but are also dependent on the PID and other factors:

$$\mu^{\text{new}}_{\text{track}}(E_\nu, \cos\theta_{\text{zenith}}) = \mu_{\text{track}}(E_\nu, \cos\theta_{\text{zenith}}), \tag{3.26}$$

$$\mu^{\text{new}}_{\text{shower}}(E_\nu, \cos\theta_{\text{zenith}}) = \mu_{\text{shower}}(E_\nu, \cos\theta_{\text{zenith}}) \cdot \left(f_{\text{TrShct}} \cdot \cos\theta_{\text{zenith}} + \left(\frac{E_\nu}{E_0}\right)^{f_{\text{TrShE}}} \right). \tag{3.27}$$

$\mu_{\text{track}}(E_\nu, \cos\theta_{\text{zenith}})$ is the number of reconstructed track events for a certain energy and zenith angle, while $\mu_{\text{shower}}(E_\nu, \cos\theta_{\text{zenith}})$ describes the number of reconstructed showers. Both values are calculated by the steps following Fig. 3.1.

The priors for the flux parameters are taken from Figures 7, 8 and 9 from [24] and can be found in table 3.3. Figure 7 in [24] also explains the powerlaw implementation of the two energy-dependent flux skews f_{nunubarE} and f_{TrShE}.

Fig. 3.13 shows the influence of the new flux parameters. While energy scale and PID parameters have an effect mainly for higher values of θ_{23}, assuming NH to be true, the flux parameters also decrease the sensitivity for lower values of the mixing angle. The statistical significance loss is equal to 0.5σ for $\theta_{23} = 40°$ and $1.3\sigma$for $\theta_{23} = 50°$. For IH, we can see a relatively constant sensitivity loss for all values the mixing angle θ_{23}: 0.55σ for $\theta_{23} = 40°$ and $0.4\sigma$for $\theta_{23} = 50°$.

Because the priors are taken from the Barr paper in 2006 [24], an analysis of systematic uncertainties in atmospheric neutrino flux, the effect of the priors concerning the sensitivity loss are more accurate than for the other two classes of new parameters. Nevertheless, the fit using the priors is in the same range as with the other parameters before, suggesting an equally important influence by all new parameter classes, though this depends on the final systematic uncertainties of the other parameter sets.

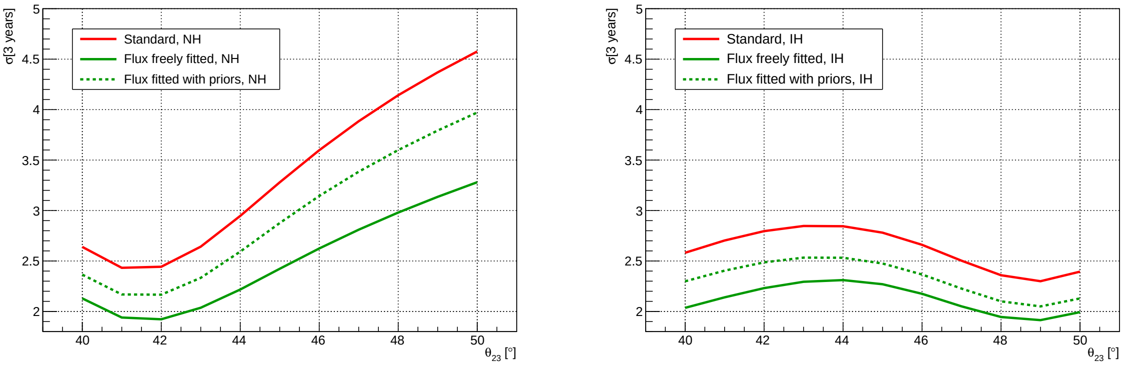

(a) NMH = NH

(b) NMH = IH

Figure 3.13: Influence of the flux parameter on the sensitivity: red is the standard fit (see Fig. 3.4); the solid/dashed green line is the fit including all new flux parameters without/with their priors.

For NH, the statistical significance loss with uncertainties is equal to 0.3σ for $\theta_{23} = 40°$ and $0.55\sigma$for $\theta_{23} = 50°$. For IH, we again see a relatively constant significance loss: 0.3σ for $\theta_{23} = 40°$ and $0.25\sigma$for $\theta_{23} = 50°$.

The dominating parameters in the fits without priors are f_{Fluxemu} for low values of θ_{23} for NH and high θ_{23} for IH, so the skew between the incoming flux between electron and muon flavour, and $f_{\text{nunubarct}}$ for high values of θ_{23} for NH and low θ_{23} for IH, so the zenith angle-dependent skew for neutrinos and antineutrinos. However, both parameters are restricted very well and are suppressed by their priors. Additionally, f_{nunubarE} is high in the fits with priors for NH. Example values for the fits can be found in the appendix for NH in table A.6 and for IH in table A.7. Because the parameter values are very different for different values of θ_{23}, values are given for $\theta_{23} = 41°$ and $\theta_{23} = 49°$.

3.2.4 Combination of new Systematics

In the end, we want to know the effect of all new parameters joined together. For this we activate all new parameters to be fitted with their priors. All original parameters are also used with their priors (already implemented in *paramNMH*), except for ΔM^2 and θ_{23} which are freely fitted. We used only up-going neutrinos here, so $e_{\text{Escctdown}}$ is basically fixed to 0. For the PID, the prior set = 5 % is used.

In Fig. 3.14 the fits from before with their priors are shown for comparison. For NH, the flux parameters dominate the sensitivity loss for lower values of θ_{23}, while flux and energy parameters are equally important for higher values of the mixing angle. It is also important to take the PID parameters into account, especially because the uncertainties are not well known here, so the loss in sensitivity due to the PID systematics might be

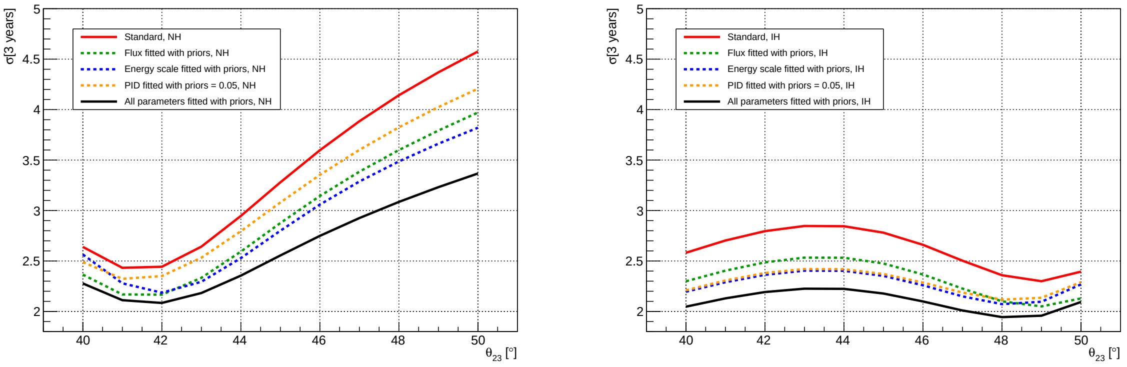

(a) NMH = NH

(b) NMH = IH

Figure 3.14: Combination of energy scale, PID and flux parameter: red is the standard fit (see Fig. 3.4); the dashed blue line is the fit including all new energy scale parameters with their priors; the dashed green line is the fit including all new flux parameters with their priors; the dashed orange line is the fit including all new PID parameters with priors = 0.05; the black line is the fit using all parameters including their priors, except for ΔM^2 and θ_{23} which are freely fitted.

even higher. Additionally, we have the black line, which is the result of the fit using all systematics combined as it is explained above. The statistical significance loss with all systematics (black) compared to the standard fit (red) is equal to 0.35σ for $\theta_{23} = 40°$ and 1.2σ for $\theta_{23} = 50°$. The minimal significance is reached at 2.1σ for $\theta_{23} = 42°$ and the maximum is at 3.4σ for $\theta_{23} = 50°$.

For IH, the flux parameters dominate for higher values of θ_{23}. In difference to NH, here the PID parameters are equally important to the energy scale parameters for all values of the mixing angle. The statistical significance loss with all systematics (black) compared to the standard fit (red) is equal to 0.55σ for $\theta_{23} = 40°$ and 0.3σ for $\theta_{23} = 50°$. The minimal significance is reached at 1.95σ for $\theta_{23} = 48°$ and the maximum is at 2.2σ for $\theta_{23} = 43°$ and $44°$.

To improve the sensitivity again, we now take down-going neutrinos into account, see Fig. 3.15. In order to do that, we double the numbers of $\cos\theta_{\text{zenith}}$ bins, and increase the range from 1 to -1, so we do not work with one hemisphere but with the whole sphere now. We can use the down-going neutrinos as some kind of reference, because their flux is approximately the same as for up-going neutrinos, mirrored at the horizon. The main difference is that we assume the flux arriving at the detector is the unoscillated flux generated in the atmosphere, because the propagating length is very short and no matter effects occur. With that, both the down-going events for normal and inverted hierarchy are absolutely the same, because we do not apply oscillation, so we can use those as reference. For simplicity, *paramNMH* does not take down-going muons into account, so every calculated event that is coming from above is the product of a neutrino

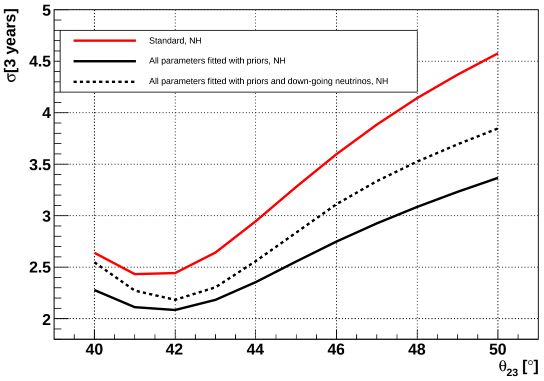

Figure 3.15: Combination of energy scale, PID and flux parameters: red is the standard fit (see Fig. 3.4); the solid black line is the fit using all parameters including their priors except for ΔM^2 and θ_{23} which are freely fitted; the dashed black line additionally uses down-going neutrinos as reference. Normal hierarchy is assumed to be true.

interaction. This does not apply to real data, where we have to use an effective muon veto, to distinguish between atmospheric muons and muons generated by neutrinos interacting in the detector volume [18].

In Fig. 3.15 we can see the influence of the down going neutrinos for NH: the fit is done by using the same systematics as before (solid black line), with the exception that we now have to use $e_{\mathrm{Escctdown}}$, which describes the up/horizontal skew of the energy scale for down-going neutrinos as counterpart to e_{Escctup}. As we would expect, the reference data given by the event rates of down-going neutrinos increases the sensitivity significantly, so the loss in sensitivity due to more parameters is not so high when we include down-going neutrinos in the sensitivity study. The statistical significance loss with all systematics including down going neutrinos (dashed black) compared to the standard fit (red) is equal to 0.1σ for $\theta_{23} = 40°$ and 0.65σ for $\theta_{23} = 50°$. The minimal significance is reached at 2.2σ for $\theta_{23} = 42°$ and the maximum is at 3.85σ for $\theta_{23} = 50°$.

3.2.5 Sensitivity on the Atmospheric Oscillation Parameters

Another important measurement of ORCA will be the 90 % confidence level contour for the great squared mass difference ΔM^2 and the mixing angle θ_{23}, which define the atmospheric oscillation parameters. This can be done since version 3.0 of *paramNMH*, however, due to the minimization problems by using energy scale parameters, we had to use another strategy: We calculated the sensitivity for several different values of ΔM^2 and θ_{23} to be rejected to a true value (here we used $\theta_{23} = 45°$ and $\Delta M^2 = 2.44 \cdot 10^{-3}$ eV) and then interpolated between these grid points to get the 90 % confidence level. Comparison with the contour method provided by ROOT (which is used in the original version 3.0 of

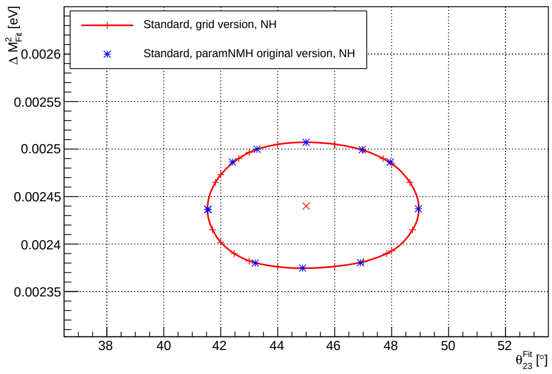

Figure 3.16: Comparison of the new method to calculate the 90 %-contour (red curve) with the original version in *paramNMH* (blue data points). Used are the original *paramNMH* parameters fitted without priors for NH. True values (red cross) is marked by the values $\theta_{23} = 45°$ and $\Delta M^2 = 2.44 \cdot 10^{-3}$ eV.

paramNMH) shows that the results for the standard fit are in agreement with each other, see Fig. 3.16.

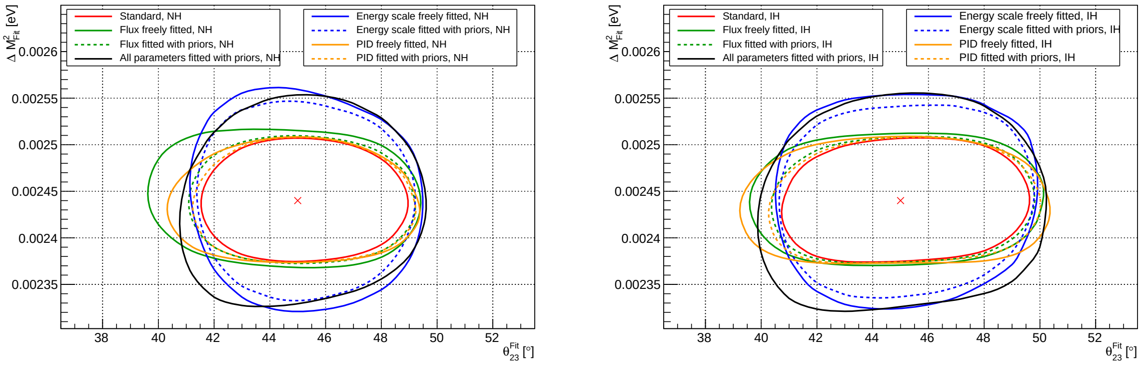

(a) NMH = NH

(b) NMH = IH

Figure 3.17: Contour fit: 90 % contour for fixed fitted θ_{23}^{fit} and ΔM^2_{fit}. True values (red cross) is marked by the values $\theta_{23} = 45°$ and $\Delta M^2 = 2.44 \cdot 10^{-3}$ eV. The colours are expressing the same configuration as in Fig. 3.14. Solid and dashed lines define freely fitted or fitted with priors, respectively. The red curve is the fit using standard parameters without priors, while the black curve is using all parameters fitted with their priors.

In Fig. 3.17 we can see the influence on the contour: For NH, the maximal values of the 90 % contour for the original *paramNMH* parameters fitted without priors (red) are $\theta_{23}^{\text{fit}} = 41.5°$ and $\theta_{23}^{\text{fit}} = 49°$, and $\Delta M^2_{\text{fit}} = 2.375 \cdot 10^{-3}$ eV and $\Delta M^2_{\text{fit}} = 2.51 \cdot 10^{-3}$ eV. If we add the energy scale systematics (blue), the maximal values get larger by almost 100 %

for ΔM^2_{fit} ($2.32 \cdot 10^{-3}$ eV, $2.56 \cdot 10^{-3}$ eV) and only slightly larger for θ_{23}^{fit} (41.1°, 49.5°). If we add the PID systematics (orange), we can see we have almost no influence on ΔM^2_{fit}, but the maximal values are increased for θ_{23}^{fit} (40.3°, 49.4°). If we add the flux systematics (green), the maximal values for ΔM^2_{fit} just increase slightly ($2.37 \cdot 10^{-3}$ eV, $2.465 \cdot 10^{-3}$ eV), but the maximal values for θ_{23}^{fit} are increased by a higher amount (39.5°, 49.4°). If we apply the priors to the fits (dashed), the maximal values do not increase that much, as we can expect it. If we apply all parameters with their priors (black), we get increasing maximal values for ΔM^2_{fit} due to the energy scale parameters ($2.325 \cdot 10^{-3}$ eV, $2.555 \cdot 10^{-3}$ eV) and increasing maximal values for θ_{23}^{fit} mainly due to flux and PID systematics (40.75°, 49.5°). The effect for IH is similar.

While the energy scale parameters mainly influence the squared mass difference, the flux and PID parameters mainly affect the mixing angle. This is not surprising, because both energy scale and ΔM^2 are affecting the energy for the minimum of the oscillation probability $P_{\nu_\mu \to \nu_\mu}$ and are therefore degenerated in the first order. On the other hand, flux and θ_{23} are both changing the depth of the minimum of the oscillation probability $P_{\nu_\mu \to \nu_\mu}$ and therefore affecting the track/shower ratio, just like the PID obviously does.

3.3 Beam Experiment

Instead of using the atmospheric flux, one can use an artificial neutrino beam, produced in a particle accelerator that is sent directly towards the detector. We have tested two different beams, one coming from Protvino in Russia [25] (using the beam settings from [26]), aiming for a detector at the ORCA site, and the other one coming from J-PARC in Japan [27] [28], using a hypothetical detector built in the sea between Japan and Korea. The hypothetical detector is assumed to be 1.5° off-axis from the J-PARC beam, whose data we only used for Super-ORCA. This is mainly done to determine the CP-violating phase δ_{CP}, assuming the NMH is already determined. Here we assume NH to be true.

Both beams are essentially a ν_μ beam with contamination of ν_e, $\bar{\nu}_e$ and $\bar{\nu}_\mu$ using positive horn polarity. Like in the atmospheric flux, tau neutrinos and antineutrinos are only produced by neutrino oscillation in a sufficient number.

While the atmospheric flux is depending on the neutrino energy and the zenith angle, the beam's angle is of course fixed, since it comes only from one direction to the detector. Therefore, $\cos\theta_{\text{zenith}}$ is taking one value which is not important for the flux itself, but for the path through Earth and therefore for the oscillation probability. Additionally, angular resolution is of no use here, because the beam's flux is higher by many magnitudes than the atmospheric flux, so we can roughly assume that all neutrino events produced in the detector are coming from the beam's source, so the value of $\cos\theta_{\text{zenith}}$ is quite clear and does not need any smearing. All other calculations like effective mass, PID and energy resolution stay the same as for the atmospheric neutrino flux.

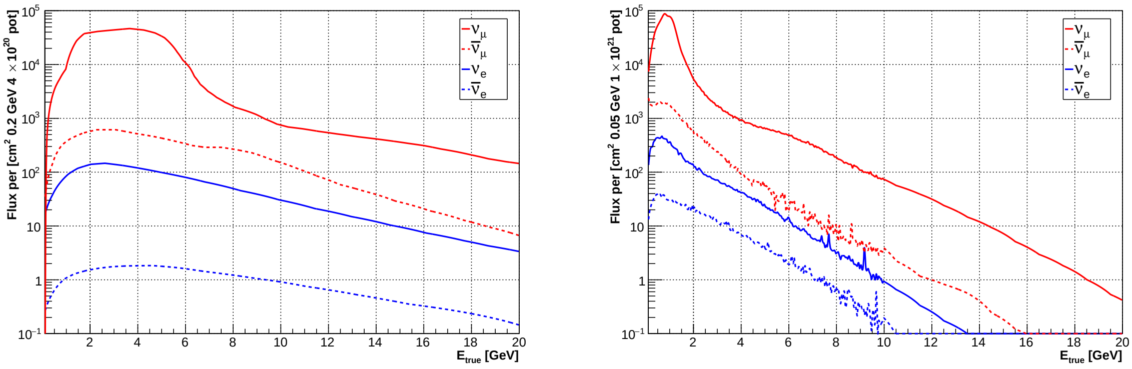

(a) Protvino beam (b) J-PARC beam

Figure 3.18: Unoscillated flux of Protvino (a) [25] and J-PARC beam with 1.5° off-axis angle (b) [27] [28].

Due to the high flux, a sensitivity of 3σ or even more for NMH and δ_{CP} can be achieved faster than with using the atmospheric flux. However, the neutrinos propagate only through a small fraction of the Earth's outer mantle and never through the core, so the matter effect is not that high for all events. This can be compensated by low uncertainties of the flux and the purity of the artificial beam, which means that one channel is favoured by the flux (in Fig. 3.18 it is ν_μ).

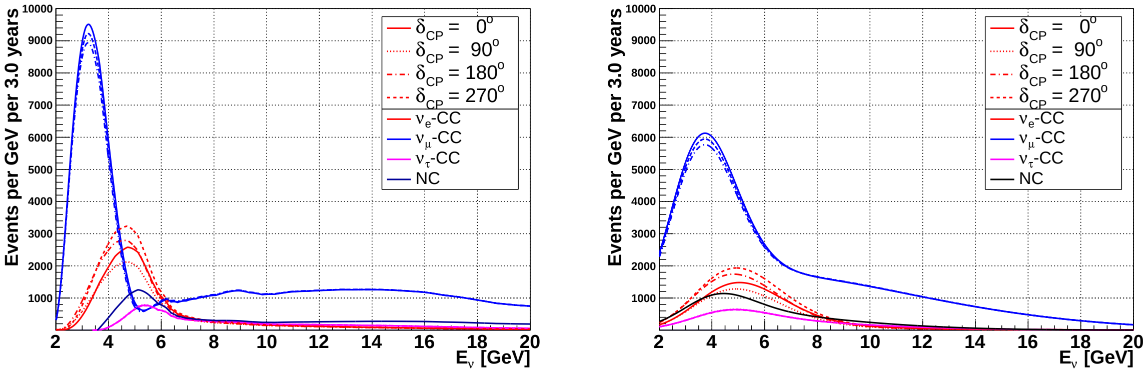

(a) Without smearing due to resolution (b) With smearing due to resolution

Figure 3.19: Expected event numbers for ORCA after three years of data taking using the Protvino neutrino beam (positive horn polarity), assuming NH to be true for four different test-values of δ_{CP}.

In Fig. 3.19 the number of events after three years are shown without (a) and with (b) applying the detector's resolution. As it can be seen, the muon flavour dominates, however, the sensitivity for determination of δ_{CP} comes from the electron flavour in an energy interval between 2 and 8 GeV. Here, the smearing towards lower energies can be seen very well, as it is described in section 3.1.3, especially for τ-CC and NC interactions.

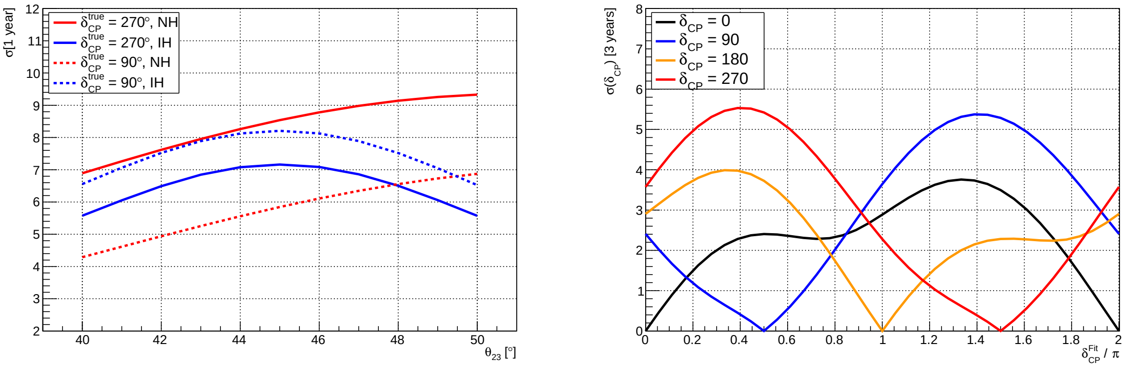

(a) Sensitivity of NMH

(b) Sensitivity of δ_{CP}

Figure 3.20: (a) Sensitivity to determine the NMH with ORCA using the Protvino beam after one year of data taking as a function of θ_{23}. (b) Sensitivity to exclude δ_{CP} with ORCA using the Protvino beam after three years of data taking as a function of $\delta_{\mathrm{CP}}^{\mathrm{true}}$ for NH, $\theta_{23} = 42°$ is fixed.

Fig. 3.20 shows the sensitivity to determine the neutrino mass hierarchy after one year, and the sensitivity to determine δ_{CP} after three years of data taking using the Protvino beam as part of the project "Protvino to ORCA" (P2O). We fitted all original *paramNMH*-parameters with their priors. With the beam, determining the NMH would reach the 5σ within one year for almost all values of θ_{23} and δ_{CP} (a). Interestingly, the dependency on the mixing angle differs from the sensitivity curves determined with the atmospheric flux (see Fig. 3.4), as well as we find a stronger dependency on the CP-violating phase.

In Fig. 3.20 (b) we can see the sensitivity of rejecting a wrong $\delta_{\mathrm{CP}}^{\mathrm{Fit}}$ for an assumed $\delta_{\mathrm{CP}}^{\mathrm{true}}$. For $\delta_{\mathrm{CP}}^{\mathrm{true}} = 0$ and π, 1σ is reached after three years for ±20° from the true value, while for $\delta_{\mathrm{CP}}^{\mathrm{true}} = \pi/2$ and $3/2\pi$ the 1σ precision is much more broadened and asymmetric with $+30°/-45°$ around the true value. $\theta_{23} = 42°$ is fixed.

For $\delta_{\mathrm{CP}}^{\mathrm{true}} = 0$ and π, we additionally find a local minimum in the fit, for example for $\delta_{\mathrm{CP}}^{\mathrm{true}} = 0$ at $\delta_{\mathrm{CP}}^{\mathrm{Fit}} = 0.75\pi$. This is due to the fact that in Fig. 3.19 the electron neutrino curves for $\delta_{\mathrm{CP}} = 90°$ and $\delta_{\mathrm{CP}} = 270°$ are the best to be distinguished, so every value has some other value to be degenerated in first order when it comes to muon neutrino event numbers (see section 4.1). Therefore, it is much more complicated for the fit to distinguish between those $\delta_{\mathrm{CP}}^{\mathrm{Fit}}$ values. This is also the reason, why the maximum for the red and blue curves are much higher than for the other values, because their true values for δ_{CP} create an extremely low or high number of muon neutrinos.

Chapter 4

Sensitivity Studies for Super-ORCA

While ORCA's main purpose is the determination of the neutrino mass hierarchy in an energy range of the 2 GeV to 15 GeV, Super-ORCA focuses on the measurement of the value of the CP-violating phase δ_{CP} in the energy interval between 1 GeV and 6 GeV. Therefore, a denser arrangement of the detector's instrumentation is needed, causing an increase of the effective mass for lower energies. In addition, the accuracy of PID, the energy and angular resolution are to be improved. For Super-ORCA, the vertical spacing between the DOMs is assumed to be ten times denser than for ORCA.

For Super-ORCA the same software *paramNMH* is used as a basis and configured to be used for a much denser detector. Therefore, we have to change the subroutines of the calculation of the effective mass, the PID and the detector resolution. All other aspects of neutrino flux and oscillation stay the same as before. However, the minimum energy to be considered is decreasing from 2 GeV for ORCA to 0.1 GeV for Super-ORCA. Because we had a binning of 20 for each energy magnitude for ORCA, the total number of energy bins for Super-ORCA is increased by one magnitude to 60 bins, while the zenith angle bins are still set to 40. The seesaw centerpoint E_0 for the spectral index is set to 1 GeV for Super-ORCA.

4.1 Performance changes for Super-ORCA

Because this is a new project, we changed the oscillation parameters slightly, according to the values in the PDG [29] from 2018, which are newer than those values used in the Letter of Intent [2] for ORCA. We used the old values there to compare our results to previously made results. The standard parameters for Super-ORCA can be seen in table 4.1. We checked the changes in NMH sensitivity due to that small difference in the oscillation values, and they are not significant, as expected.

Instead of having different effective masses, PIDs, and resolutions for all eight types of interactions, $\overset{(-)}{\nu}_\tau$ are treated like $\overset{(-)}{\nu}_{\mathrm{NC}}$. All parameters used in the following section to

parameter	true value	prior	treatment
θ_{23} (°)	42	no	Fitted
θ_{13} (°)	8.8	0.26	Fixed
θ_{12} (°)	33.7	N/A	Fixed
ΔM^2 (10^{-3} eV)	2.43	no	Fitted
Δm^2 (10^{-5} eV)	7.54	N/A	Fixed
δ_{CP} (°)	0	no	Fitted
Overall flux factor	1	0.1	Fitted
NC scaling	1	0.1	Fitted
$\nu/\bar{\nu}$ skew	0	0.03	Fitted
μ/e skew	0	0.1	Fitted
Energy slope (spectral index)	0	0.05	Fitted

Table 4.1: New standard parameters used for Super-ORCA.

calculate the effective mass, PID and the resolution are shown in table A.8 in the appendix [30].

4.1.1 Super-ORCA-specific Inputs

The formula describing the effective mass has not changed much for Super-ORCA, but the parameters N_{Meff}, E_{min} and σ_{Meff} for the different interaction types have changed. Especially the threshold energy had been decreased due to the denser detector instrumentation. Note that due to the determination of the new parameters, N_{Meff} is no longer in units of a mass, but of efficiency of an overall maximum effective mass $M_{\mathrm{eff}}^{\mathrm{max}} = 4$ Mton for all types of interactions, so that our formula for the effective mass now reads:

$$M_{\mathrm{eff}}(E_{\mathrm{true}}) \;=\; M_{\mathrm{eff}}^{\mathrm{max}} \cdot N_{\mathrm{Meff}} \;\cdot\; \tanh\left(\frac{E_{\mathrm{true}} - E_{\mathrm{min}}}{\sigma_{\mathrm{Meff}}}\right), \tag{4.1}$$

The major change with respect to ORCA is the shift to lower energies in the effective mass (see Fig. 4.1 (a)): While ORCA is not sensitive for energies below 2 GeV, Super-ORCA has full capacity at that energy and even nearly maximal effective mass at 1 GeV. The slope of the effective mass is much steeper as for ORCA, so maximum capacity is reached very fast. Note that Super-ORCA is not sensitive for energies below 300 MeV, which is technically described by the effective mass, so all strange effects of PID and other inputs for low energies can be neglected.

The formula for the PID has changed completely, so we are now using the following approach to calculate the probability of classifying an event as track:

$$P_{\mathrm{track}}(E_{\mathrm{true}}) \;=\; x_0 + \frac{x_1}{(E_{\mathrm{true}} - x_3)} + \frac{x_2}{(E_{\mathrm{true}} - x_3)^2}, \tag{4.2}$$

Note that many of those parameters x_i, $i = 0, \ldots, 3$ can be zero for some of the interaction types due to their different shapes (see table A.8). For example, the probability of

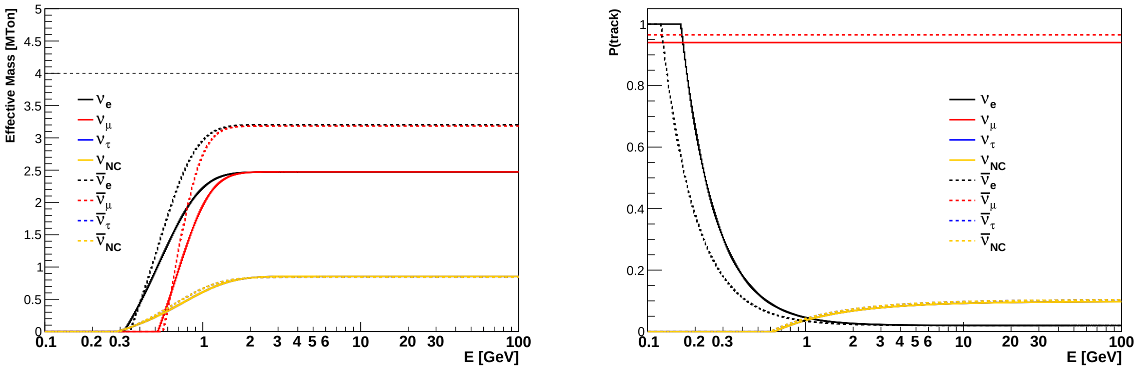

(a) effective mass

(b) PID

Figure 4.1: Energy-dependent effective mass (a) and PID (b) for all interaction types for Super-ORCA. The dashed line at 4 Mton for the effective mass describes the upper limit set for the effective mass. $\overset{(-)}{\nu}_\tau$ are behaving the same way as $\overset{(-)}{\nu}_{\text{NC}}$.

classifying a $\overset{(-)}{\nu}_\mu$ as a track are not depending on the energy, since all values except x_0 are set to zero. Because the formula has changed, the new PID parameters cannot be used for Super-ORCA, while the flux and effective mass systematics can be used here, too.

The increase of classifying $\overset{(-)}{\nu}_e$ as a track for lower energies is eye-catching and could be seen as alarming because they all should be classified as showers. However, as we stated above, Super-ORCA is not sensitive for energies below 300 MeV, so this region can be ignored.

Both the mean value and the standard deviation are calculated by a different equation for Super-ORCA (see Fig. 4.2):

$$\bar{E}(E_{\text{true}}) = E_{\text{true}} \cdot \left(m_0 + m_1 \cdot \left(\frac{E_{\text{true}}}{m_2} \right)^{m_3} \right), \tag{4.3}$$

$$\sigma_{\text{resol}}(E_{\text{true}}) = E_{\text{true}} \cdot \left(s_0 + \frac{s_1}{\sqrt{E_{\text{true}}}} + \frac{s_2}{E_{\text{true}}} + s_3 \cdot E_{\text{true}}^{s_4} \right). \tag{4.4}$$

However, the resolution is assumed to be the same for all true energies below $E_{\text{true}} = 0.4$ GeV. Additionally, the standard deviation σ_{resol} must stay in the interval $[0; 0.4\ E_{\text{true}}]$, so if it expires a limit at one side, it is set to this limit.

In Fig. 4.2 (a) it can be seen that NC- and tau-CC-events are extremely shifted to lower energies for high energy events, while all events in the lower energy sector are shifted to higher values for all interaction types. The reason for this behaviour is a selection effect: Super-ORCA can not detect neutrinos in that energy region very well. The only events, the detector can measure, are those with a high luminosity, so these events are going to be treated as events with much higher energy than E_{true}. However, because Super-ORCA is not so sensitive in that energy region, these shifts are not so important because

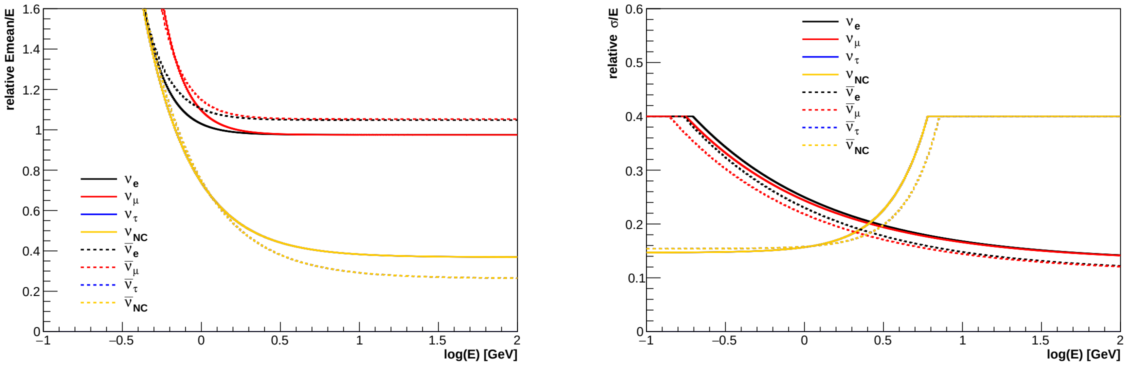

(a) $\bar{E}/E_{\text{true}}$ (b) $\sigma_{\text{resol}}/E_{\text{true}}$

Figure 4.2: (a) Relative mean energy in dependency of the true energy for all interaction types for Super-ORCA. (b) Relative standard deviation in dependency of the true energy for all interaction for Super-ORCA. $\overset{(-)}{\nu}_\tau$ are behaving the same way as $\overset{(-)}{\nu}_{\text{NC}}$.

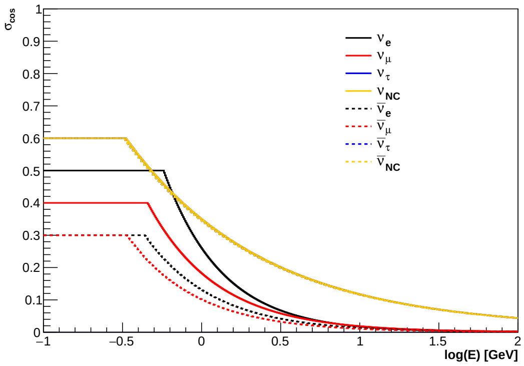

Figure 4.3: Energy-dependent angular resolution $\sigma_{\cos}$ for all interaction types for Super-ORCA. $\overset{(-)}{\nu}_\tau$ are behaving the same way as $\overset{(-)}{\nu}_{\text{NC}}$.

of the suppressing due to the effective mass. In Fig. 4.2 (b) we can see the contrary behaviour of the energy resolution: While electron and muon (anti-)neutrinos are rather sharp distributed for high energies, NC and tau-CC events, which have a very different $\bar{E}$ compared to $\overset{(-)}{\nu}_e$-CC and $\overset{(-)}{\nu}_\mu$-CC events, have a high uncertainty. For low energies it is the other way around. The sensitivity for both the NMH and δ_{CP} is coming from electron and muon (anti-)neutrinos, the resolution of which is quite good for the important energy interval (low energies are again neglectable due to the effective mass).

The angular resolution for Super-ORCA does not depend on one single parameter like it has been for ORCA, but a set of parameters called d_i, $i = 1, \ldots, 6$:

$$\sigma_{\cos}(E_{\text{true}}) \;=\; d_0 + \frac{d_1}{\sqrt{E_{\text{true}}}} + \frac{d_2}{E_{\text{true}}} + \frac{d_3}{E_{\text{true}}^2} + d_5 \cdot E_{\text{true}}^{d_6}. \tag{4.5}$$

d_4 is an upper threshold for $\sigma_{\cos}$, important for the low energy range. The exact position of the limit is not so important due to the cut-off by the effective mass. In Fig. 4.3 we see that the angular resolution gets better with higher energies, similar to those of ORCA. Again, NC-events have the worst resolution, which mainly creates an unwanted background, because they are not depending on neutrino oscillations and therefore hold no information of the CP-violating phase.

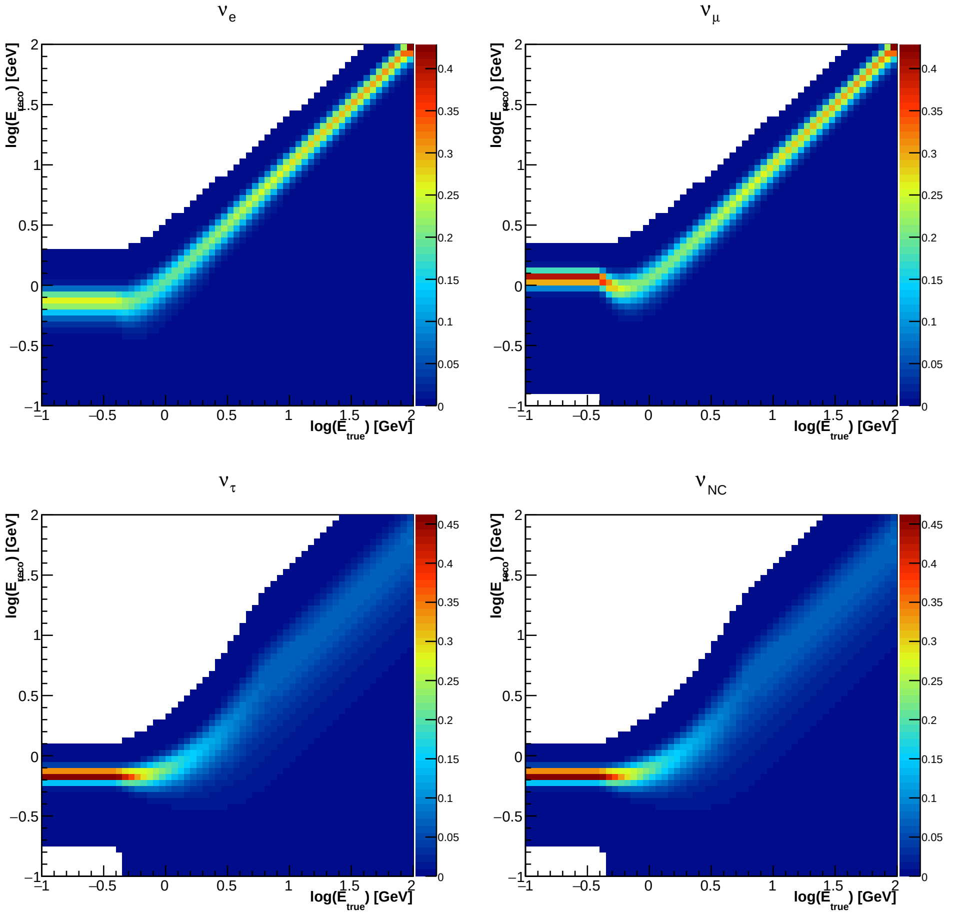

Figure 4.4: Energy resolution E_{reco} in dependency of the true energy for all neutrino interaction types for Super-ORCA. All bins below 0.4 GeV have the same resolution calculated for 0.4 GeV.

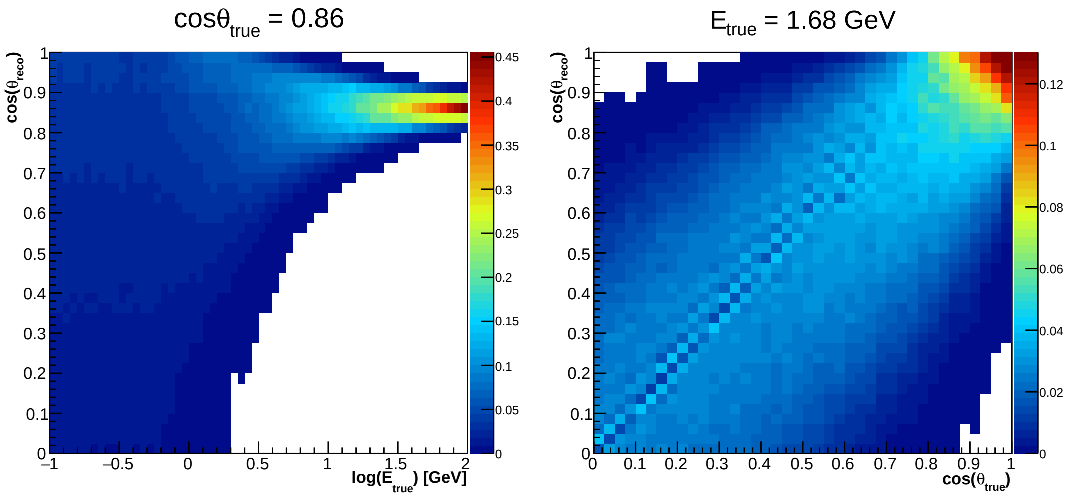

Figure 4.5: Angular resolution for ν_e for Super-ORCA: left: $\cos\theta_{\text{reco}}$ as a function of E_{true} for $\cos\theta_{\text{true}} = 0.86$; right $\cos\theta_{\text{reco}}$ as a function of $\cos\theta_{\text{true}}$ for $E_{\text{true}} = 1.68$ GeV. The z-axis is giving the ratio of the smearing in a certain bin of $\cos\theta_{\text{reco}}$ depending on the values of E_{true} and $\cos\theta_{\text{true}}$.

Fig. A.2 shows for Super-ORCA the energy resolution for all four kinds of neutrino interactions (antineutrinos are shown in the appendix, see Fig. **??**). In comparison with the ORCA detector, we can see that the resolutions are much sharper for Super-ORCA, at least for $\overset{(-)}{\nu}_e$-CC and $\overset{(-)}{\nu}_\mu$-CC interactions. The $\overset{(-)}{\nu}_\tau$-CC channel by definition has the same resolution as the NC interactions. As stated above, the resolution is constant for all energy bins below 0.4 GeV, because the formula to calculate the resolution would deliver non-physical results. Due to the cut off of the effective mass, this energy range is not so important.

Fig. 4.5 shows the angular resolution of ν_e-CC in dependency of the true energy E_{true} and the cosine of the true zenith angle $\cos\theta_{\text{true}}$. Again we can see that the energy-dependent resolution is much better than for ORCA. Note that the energy of $E_{\text{true}} = 1.68$ GeV is below the minimum energy at which ORCA is still sensitive, so the dependency on the zenith angle looks much broader than in Fig. 3.9.

Here again we can see the effect close to the pole: the maximum of the smearing $\cos\theta_{\text{reco}}$ is shifted to the pole for high values of $\cos\theta_{\text{true}}$. The strange effect slightly above the line $\cos\theta_{\text{true}} = \cos\theta_{\text{reco}}$ comes from the large step size used for the course angle α, which has already been increased by a factor of 10 for Super-ORCA compared to ORCA. Without that increase the effect would be much stronger, and we have derived that the factor of 10 is sufficient for the fit. A higher binning would not influence the fit result, just the time consumption to build the resolution histograms.

4.1.2 Fast Oscillation in the low Energy Limit

The fact that Super-ORCA is sensitive at much lower energies than ORCA holds a problem with the simplified implementation concerning the oscillations. While there is no problem with the oscillation in the high energy limit, the oscillation in the low energy limit, mainly below 10 GeV and even more below 1 GeV is very fast, as it can be seen in Fig. 4.6 (narrow lines). The different colours show different values of δ_{CP} which differ the most for energies between 0.4 and 6 GeV, where most sensitivity of Super-ORCA comes from.

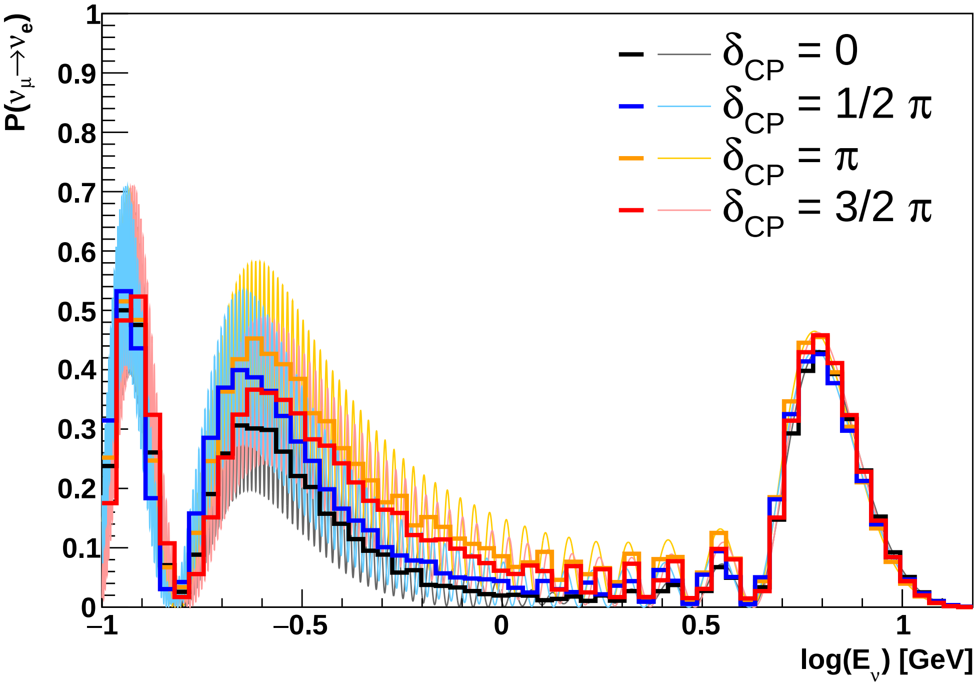

Figure 4.6: Oscillation probabilities $P_{\nu_\mu \to \nu_e}$ for four different values of δ_{CP}, NH, $\theta_{23} = 42°$ and $\cos\theta_{\text{zenith}} = 0.8$. The narrow lines in the back represent the true oscillation probabilities (here we use a finer binning of a factor of 100), while the broad lines are the average values used by the fit. The fit itself uses a finer binning of a factor of 10, which is sufficient.

The energy binning of 20 bins per magnitude is too rough for that energy range, so the oscillation probability would just be a random number depending on the energy in the center of the bin. Because a finer binning would slow down the fit by a factor similar to the finer binning, we still use 60 energy bins for the event histograms, from 0.1 to 100 GeV. However, depending on the energy of the center of the bin, the value for the transition probability for ν_μ to ν_e can differ between 0.2 and 0.5 for 0.4 GeV and $\delta_{\text{CP}} = 0$ for example, just due to a small shift in energy. Therefore, we have to use a finer binning for oscillation probability, and then calculate the average value for event rate of the histogram's bin. The averaged oscillation probabilities can be seen in Fig. 4.6 represented by the broad lines.

While we use a finer binning in Fig. 4.6 of a factor 100 for each used bin value (one broad value point) to demonstrate it here, we use only a factor of 10 for the finer binning in the fit. This factor is low enough to reduce the time of the fit and high enough that a finer binning does not make any difference anymore, so 10 is sufficient.

We get the same problem for the binning depending on the zenith angle concerning oscillation for lower energies as well. Here we found that a finer binning of a factor of 5 is sufficient, without increasing calculation time too much.

We can already see that $\delta_{\mathrm{CP}} = 0$ and π are causing different oscillation probabilities and therefore we expect a high sensitivity when we compare those two δ_{CP} values with each other. As we see later, the highest and lowest probability $P_{\nu_\mu \to \nu_e}$ (and therefore similar extremes for all other oscillation probabilities) we get for $\delta_{\mathrm{CP}} \approx 0.15\pi$ and $\delta_{\mathrm{CP}} \approx 1.1\pi$, respectively. As a result of this, all other δ_{CP} values possess a complementary δ_{CP} value with a similar oscillation probability, roughly mirrored on the other side of the extreme points. We will see the effect of this degeneration in the results below.

4.2 Results with Atmospheric Neutrinos

Super-ORCA is designed for determining the CP-violating phase δ_{CP} and is capable to determine the NMH as well. Recent analyses of global data favour normal hierarchy (NH) over IH and a value of $\delta_{\mathrm{CP}} \approx \frac{3}{2}\pi = 270°$, i.e. maximal CP violation [31]. We will therefore focus on these values to be true in the following.

4.2.1 Sensitivity on NMH

At first we want to take a look on the performance of Super-ORCA concerning the determination of the NMH. Shown in Fig. 4.7 is the sensitivity to determine NMH for different values of θ_{23} for NH and IH assumed to be true and for two different values of $\delta_{\mathrm{CP}} = 0°$ and $180°$ preserving the CP-symmetry after three years of data taking. The general dependency of the fit on θ_{23} hasn't changed compared to the results for ORCA (see Fig. 3.4), though the measurements are much more significant.

For NH assumed to be true, the significance has a minimum of 4σ (3.2σ) between $\theta_{23} = 42°$ and $43°$ for $\delta_{\mathrm{CP}} = 0°$ ($\delta_{\mathrm{CP}} = 180°$) and then increases with increasing θ_{23} up to 7.35σ (6.3σ) for $\theta_{23} = 50°$. The IH fits have a minimum of 4.4σ (3.4σ) around $\theta_{23} = 48°$ for $\delta_{\mathrm{CP}} = 0°$ ($\delta_{\mathrm{CP}} = 180°$), but do not increase that much for smaller values of θ_{23} (maximum of 5σ (4σ) for $\theta_{23} = 44°$). Therefore the sensitivity increases for $\theta_{23} = 50°$ to 5.2σ (4.2σ). For IH, the sensitivity of $\delta_{\mathrm{CP}} = 0°$ is always about 1σ above the results for $\delta_{\mathrm{CP}} = 180°$, which is a larger difference than for ORCA (0.2σ). For NH, the sensitivity of $\delta_{\mathrm{CP}} = 0°$ is mostly better than that for $\delta_{\mathrm{CP}} = 180°$, except for smaller values of θ_{23}.

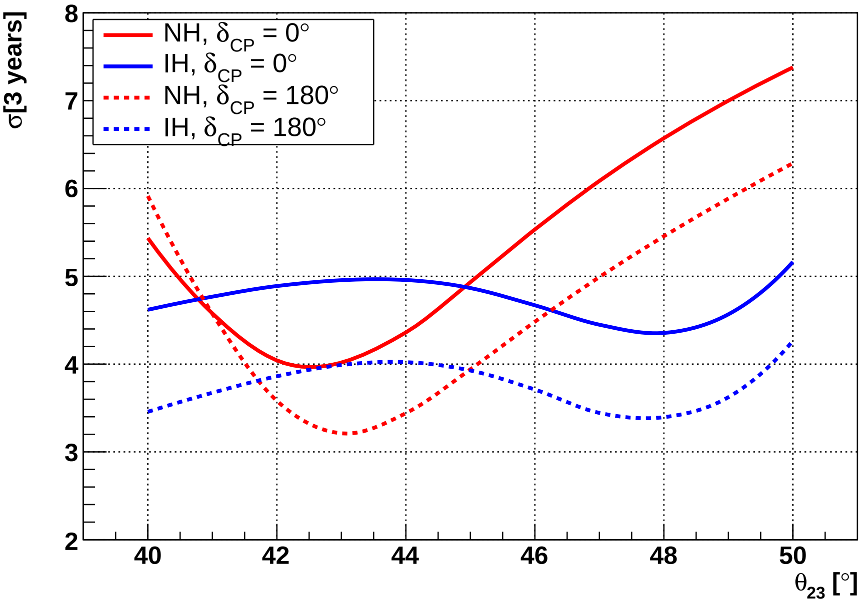

Figure 4.7: Sensitivity to determine NMH as a function of θ_{23} with Super-ORCA for assuming NH (red) or IH (blue) to be the true hierarchy after three years of data taking. $\delta_{\mathrm{CP}} = 0°$ for solid lines and $\delta_{\mathrm{CP}} = 180°$ for dashed lines. The parameters from table 4.1 have been used without their priors.

With that, Super-ORCA is about 1.5σ better than ORCA (see Fig. 3.4). To achieve the same significance as Super-ORCA after three years of data taking, ORCA would have to measure roughly eight years.

4.2.2 Distribution of the relative δ_{CP} differences

The main purpose of Super-ORCA is the determination of δ_{CP}, so we want to take a look at the distributions of the relative δ_{CP} differences we can achieve with Super-ORCA. Therefore we calculate the event rates for $\overset{(-)}{\nu_e}$ and $\overset{(-)}{\nu_\mu}$ of an ideal detector (no resolution applied, constant 4 Mton effective mass) for $\delta_{\mathrm{CP}} = 0$ and $\delta_{\mathrm{CP}} = \frac{3}{2}\pi$ as a function of the true energy E_ν and the true zenith angle θ_{zenith}. To compare the histograms with the event rates μ, we use the same equation as we did for the χ^2 fit (eq. (3.9)), calculating χ_j for each bin j:

$$\chi_j = \frac{\mu_j^{\delta_{\mathrm{CP}}=\frac{3}{2}\pi} - \mu_j^{\delta_{\mathrm{CP}}=0}}{\sqrt{\mu_j^{\delta_{\mathrm{CP}}=0}}} \tag{4.6}$$

The binning is the same used for the histograms used in the fit later: 60 energy bins and 40 zenith angle bins. If we use a finer binning we could see more structures, however,

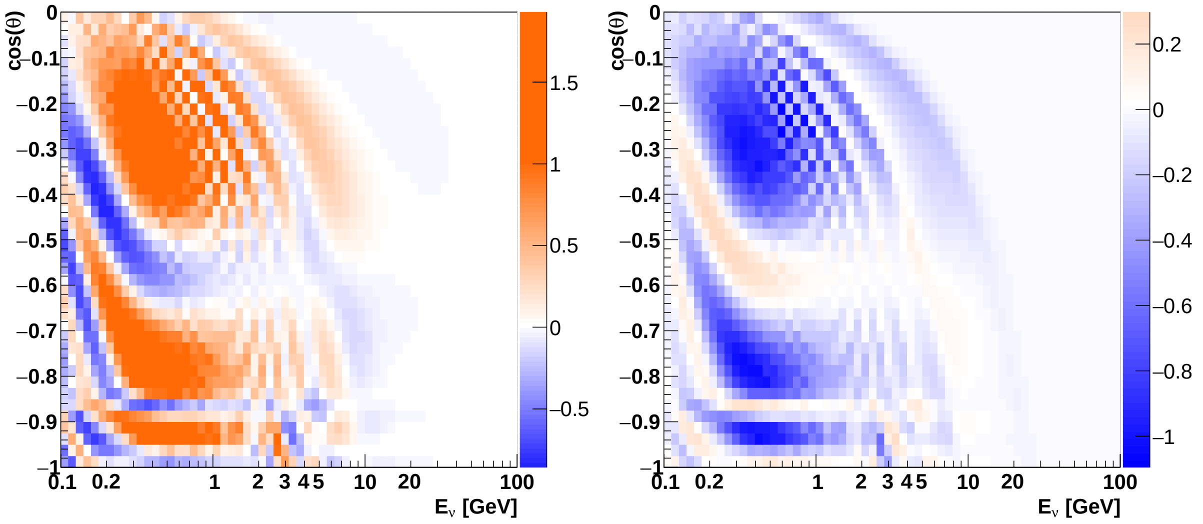

(a) $\nu_e + \bar{\nu}_e$ (CC)

(b) $\nu_\mu + \bar{\nu}_\mu$ (CC)

Figure 4.8: Distribution of the relative δ_{CP} differences for $\overset{(-)}{\nu_e}$-CC (a) and $\overset{(-)}{\nu_\mu}$-CC (b) for an ideal detector, before applying the detector resolution and using a constant effective mass of 4 Mton,as a function of the true energy E_ν and the true zenith angle θ_{zenith} after one year of data taking. The binning is the same as for the event histograms. The z-axis gives $\sqrt{\chi_j^2}$ according to eq. (4.6).

we would blur those structures anyway by applying the detector resolution later. The result of those calculation can be seen in Fig 4.8. (a) uses only $\overset{(-)}{\nu_e}$-CC to calculate the difference in the binwise statistical significance, (b) only $\overset{(-)}{\nu_\mu}$-CC.

As we can see, the main sensitivity comes from the interval between 0.2 and 6 GeV, though the true detector cannot use the events below 0.3 GeV due to the small effective mass. The main problem can be seen by comparing the two plots: The effect by the electron flavour and the muon flavour, which hold the main sensitivity in δ_{CP}, are opposing to each other. This means we have to effectively separate $\overset{(-)}{\nu_e}$-CC from $\overset{(-)}{\nu_\mu}$-CC events, so that two flavours do not cancel each other out in the fit. This requires a good knowledge of the PID, so the effect of $\overset{(-)}{\nu_e}$-CC and $\overset{(-)}{\nu_\mu}$-CC can be distinguished by track and shower classification.

Now we have to take into account that we do not have an ideal detector: We apply the effective mass and resolution introduced above. As a result, we get a cut off for low energies and the structures of Fig. 4.8 get smeared out. As we can see in Fig. 4.9, we have the highest sensitivity coming from the region between 0.5 and 2 GeV for both electron and muon flavour, which is mainly independent from the reconstructed angle.

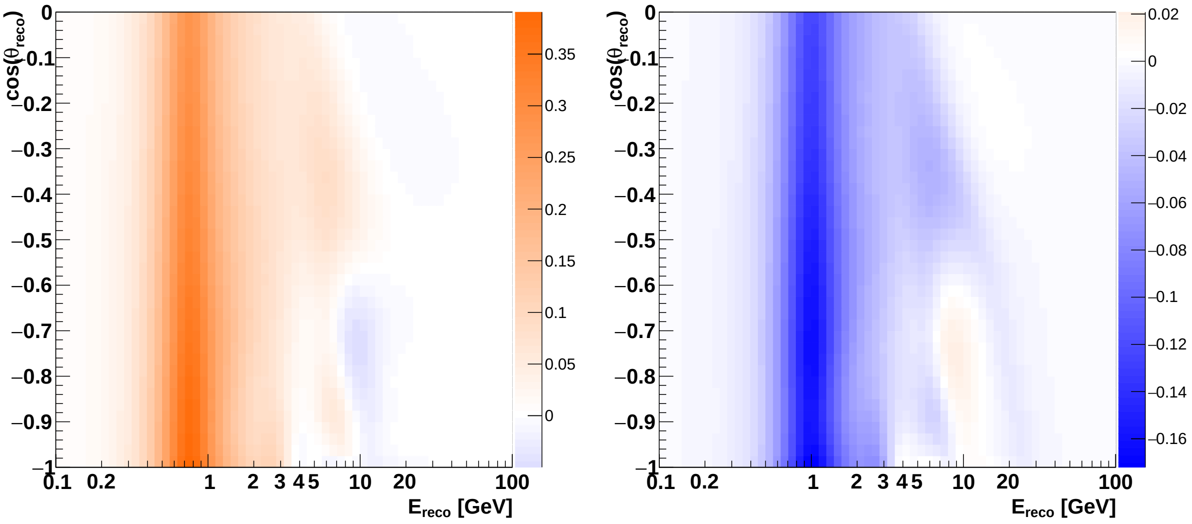

(a) $\nu_e + \bar{\nu}_e$ (CC)

(b) $\nu_\mu + \bar{\nu}_\mu$ (CC)

Figure 4.9: Distribution of the relative δ_{CP} differences for $\overset{(-)}{\nu}_e$-CC (a) and $\overset{(-)}{\nu}_\mu$-CC (b) for a detector with applying the resolution in dependence of the reconstructed energy E_{reco} and the zenith angle θ_{reco}.The binning is the same as for the event histograms. The δ_{CP} effect remains after the smearing.

When we compare the distributions of the relative δ_{CP} with those derived for Super-PINGU by Razzaque and Smirnov [32], we get very similar structures in the results for an ideal detector. However, when we look at the smeared out distribution of the relative δ_{CP} differences, we can see that Super-PINGU, using a PINGU resolution reduced by a factor of $1/\sqrt{3}$, has a much higher relative difference per bin ($\left|\chi_j^{\mathrm{max}}\right| = 0.92$ for $\overset{(-)}{\nu}_\mu$-CC) than Super-ORCA does ($\left|\chi_j^{\mathrm{max}}\right| = 0.17$ for $\overset{(-)}{\nu}_\mu$-CC). So we expect a higher sensitivity for Super-PINGU than for Super-ORCA.

4.2.3 δ_{CP}-Sensitivity Studies using χ^2-Asimov-Fits

To calculate the sensitivity for Super-ORCA to determine δ_{CP}, we again use eq. (3.9), this time with μ^{true} choosing one CP-violating phase to be true $\delta_{\mathrm{CP}}^{\mathrm{true}}$ and fit the event rates μ^{wrong} using the oscillation parameter $\delta_{\mathrm{CP}}^{\mathrm{fit}}$. $\delta_{\mathrm{CP}}^{\mathrm{fit}}$ goes from 0° to 360° in steps of 10°, so we have 36 fit points per curve. The resulting sensitivity in units of σ gives us the statistical significance of refuting $\delta_{\mathrm{CP}}^{\mathrm{fit}}$, assuming $\delta_{\mathrm{CP}}^{\mathrm{true}}$ to be true.

If it is not stated otherwise, we are using the standard parameters of *paramNMH* fitted without their priors (see table 4.1), the normal hierarchy and $\theta_{23} = 42°$ after five years of data taking for Super-ORCA measurements with atmospheric neutrinos.

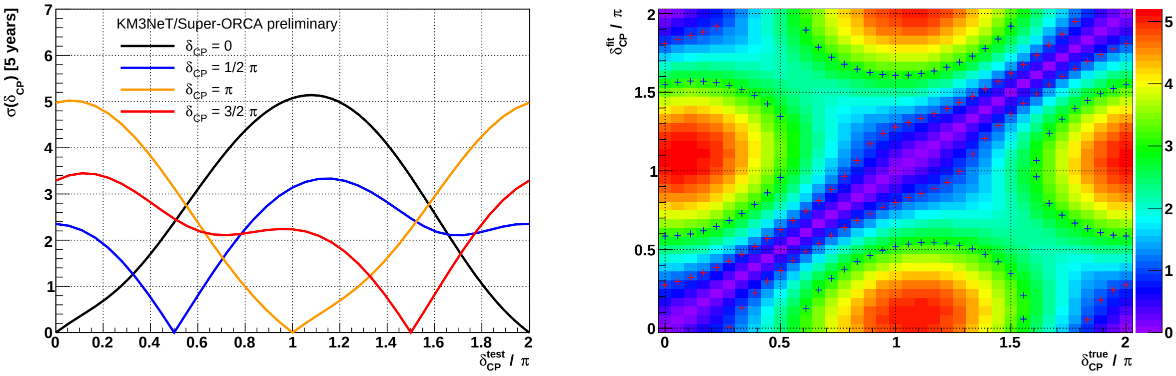

(a) function of $\delta_{\mathrm{CP}}^{\mathrm{fit}}$

(b) function of $\delta_{\mathrm{CP}}^{\mathrm{true}}$ and $\delta_{\mathrm{CP}}^{\mathrm{fit}}$

Figure 4.10: Sensitivity to exclude certain values of δ_{CP} with Super-ORCA after five years of data taking as a function of $\delta_{\mathrm{CP}}^{\mathrm{fit}}$ (a) for different values of $\delta_{\mathrm{CP}}^{\mathrm{true}}$ and as a function of $\delta_{\mathrm{CP}}^{\mathrm{true}}$ and $\delta_{\mathrm{CP}}^{\mathrm{fit}}$ (b) for NH, $\theta_{23} = 42°$. In (b) the colour gives the significance, while the red (blue) crosses give the 1σ (3σ) precision for each $\delta_{\mathrm{CP}}^{\mathrm{true}}$.

At first we are interested in the sensitivity for four different values of $\delta_{\mathrm{CP}}^{\mathrm{true}} = 0°$, $90°$, $180°$ and $270°$, distributed equally spaced over $360°$, see Fig. 4.10 (a). $\delta_{\mathrm{CP}}^{\mathrm{true}}$ is easy to see from the fits, because the fit reaches 0 when $\delta_{\mathrm{CP}}^{\mathrm{fit}} = \delta_{\mathrm{CP}}^{\mathrm{true}}$. Like we have seen above by looking at the oscillations for different values of δ_{CP}, we can see the degenerate values of the CP-violating phase by looking at the local minimum for the red and the blue curve.

Interestingly, while the black and the yellow curve have a higher maximum than the others, the red and the blue curve reach the 1σ much faster at values of $\delta_{\mathrm{CP}}^{\mathrm{true}} \pm 0.15\pi$, while the other fits reach 1σ at values of $\delta_{\mathrm{CP}}^{\mathrm{true}} - 0.2\pi$ and $\delta_{\mathrm{CP}}^{\mathrm{true}} + 0.275\pi$. 60 % of δ_{CP} values are disfavoured with more than 2σ for $\delta_{\mathrm{CP}}^{\mathrm{true}} = 0$ and π, while it is even 70 % for $\frac{\pi}{2}$ and $\frac{3}{2}\pi$. Reason for the difference is again the behaviour of the oscillation probability for different values of δ_{CP} (see Fig. 4.6).

Shown in Fig. 4.10 (b) are the significances (colour) as a function of $\delta_{\mathrm{CP}}^{\mathrm{true}}$ and $\delta_{\mathrm{CP}}^{\mathrm{fit}}$. The red (blue) crosses give the 1σ (3σ) precision for each $\delta_{\mathrm{CP}}^{\mathrm{true}}$. It can be seen that the maximum significance for many values of $\delta_{\mathrm{CP}}^{\mathrm{true}}$ are positioned at 1.1π or 0.1π, which are the extreme values for δ_{CP} concerning the oscillation probabilities, as we have mentioned above (see Fig. 4.6). For $\delta_{\mathrm{CP}}^{\mathrm{true}}$ around those extreme values, we can refute about 50 % of $\delta_{\mathrm{CP}}^{\mathrm{fit}}$ with more than 3σ, while we can't reject about 25 % with even 1σ. For $\delta_{\mathrm{CP}}^{\mathrm{true}}$ far from the extreme values, for example $\delta_{\mathrm{CP}}^{\mathrm{true}} = 0.6\pi$ or 1.6π, we can refute about 88 % of $\delta_{\mathrm{CP}}^{\mathrm{fit}}$ with more than 1σ, however, we have very few percentage of $\delta_{\mathrm{CP}}^{\mathrm{fit}}$ we can refute with more than 3σ. We can see the same effect in Fig. 4.10 (a) for the blue and the red line, which hardly reach 3σ after five years of data taking.

The results in sensitivity are comparable with the results determined by ORCA using the Protvino beam after three years of data taking (see section 3.3), although the local minima of the fits occur here for other values of $\delta_{\mathrm{CP}}^{\mathrm{true}}$. The main reason for that is that

Super-ORCA gains information from lower energies than ORCA, and therefore a different shape of the δ_{CP}-differences. However, note that Super-ORCA is using atmospheric neutrinos here, while P2O uses the Protvino beam, and therefore flux with much lower uncertainties and purity. This shows the high capability of Super-ORCA, which will even improve when we assume a beam from Protvino to Super-ORCA (P2SO) later.

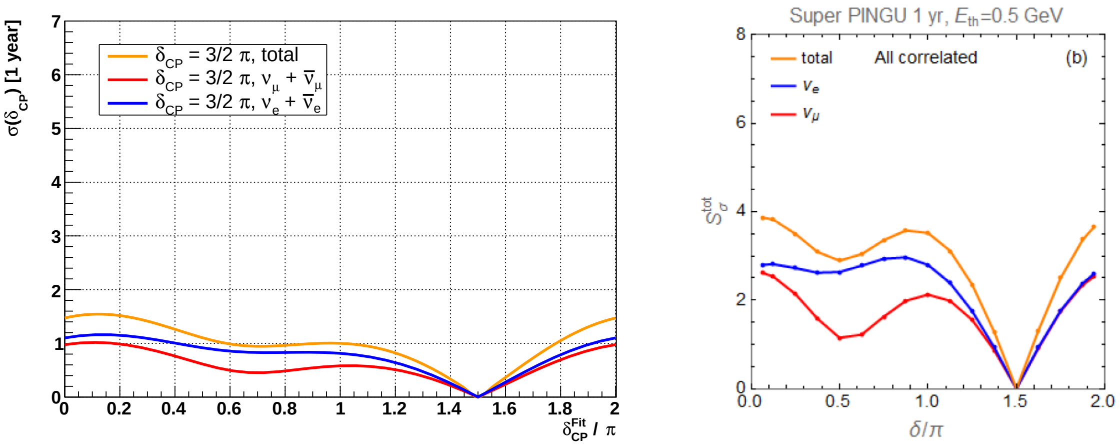

(a) Super-ORCA (b) Super-PINGU [32]

Figure 4.11: Sensitivity to exclude certain values of δ_{CP} with Super-ORCA and Super-PINGU [32] for $\delta_{\mathrm{CP}}^{\mathrm{true}} = 270°$. Shown are the total statistical significance after one year of data taking (orange), as well as the significance from $\overset{(-)}{\nu}_e$-CC (blue) and $\overset{(-)}{\nu}_\mu$-CC (red) events as a function of $\delta_{\mathrm{CP}}^{\mathrm{fit}}$.

When we compare the results with the studies made for Super-PINGU [32], we see the same effects concerning the maximums and the minimums of the fit curves. For example, the maximum of the black curve is not at π, because the smearing suppresses the sensitivity stronger for $\delta_{\mathrm{CP}}^{\mathrm{fit}} < \pi$ than for $\delta_{\mathrm{CP}}^{\mathrm{fit}} > \pi$, so the maximum is shifted towards 1.1π. For details concerning these shifts, see the theoretical part of [32]. However, the sensitivity of Super-PINGU seems to be better than for Super-ORCA (see Fig. 4.11) [32]. Note that the sensitivity for Super-PINGU is given after one year of data taking only, so to compare it with our results from Super-ORCA, we have to multiply the Super-PINGU results by $\sqrt{5}$ (five years), which we have done in 4.11 (a).

When we split up the sensitivity for $\delta_{\mathrm{CP}}^{\mathrm{true}} = \frac{3}{2}\pi$ into track and shower only (see Fig. 4.11), which can be done easily due to the calculation in eq. (3.9), we get similar results as derived in [32]: While the major part of the sensitivity comes from $\overset{(-)}{\nu}_e$ (blue), which are mainly classified as showers, the degeneration effect comes from $\overset{(-)}{\nu}_\mu$ (red), which are mainly classified as tracks. Same can be seen for Super-PINGU in Fig. 4.11 (b). However, the sensitivity after one year of data taking is significantly higher for Super-PINGU than for Super-ORCA.

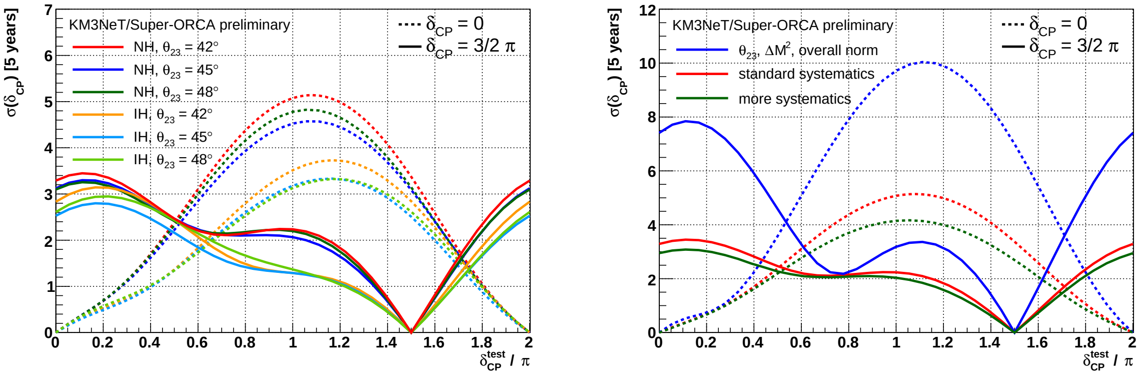

(a) different values of $\theta_{23}^{\text{true}}$ and NMH

(b) different systematics

Figure 4.12: Sensitivity to exclude certain values of δ_{CP} with Super-ORCA after five years of data taking as a function of $\delta_{\text{CP}}^{\text{fit}}$ for different values of $\theta_{23}^{\text{true}}$ and NMH (a) and for different systematics (b), which are given in table 4.2.

parameter	true value	prior	fit
θ_{23} (°)	42	no	🔵 🔴 🟢
θ_{13} (°)	8.8	fixed	
θ_{12} (°)	33.7	fixed	
ΔM^2 (10^{-3} eV)	2.43	no	🔵 🔴 🟢
Δm^2 (10^{-5} eV)	7.54	fixed	
mass ordering	NH	fixed	
Overall flux factor	1	no	🔵 🔴 🟢
NC scaling	1	no	🔴 🟢
$\nu/\bar{\nu}$ skew	0	no	🔴 🟢
μ/e skew	0	no	🔴 🟢
Energy slope (spectral index)	0	no	🔴 🟢
up/horizontal skew $\propto \cos\theta$ (f_{Fluxct1})	0	no	🟢
up/horizontal skew $\propto \cos^2\theta$ (f_{Fluxct2})	0	no	🟢
energy scale overall (e_{Escale})	1	0.03	🟢
Escale $\nu/\bar{\nu}$ skew (e_{Escnu})	0	0.03	🟢
Escale $(\nu_e+\bar{\nu}_e)/(\nu_\mu+\bar{\nu}_\mu)$ skew (e_{Escemu})	0	0.03	🟢
Escale $(\nu_{e,\mu}+\bar{\nu}_{e,\mu})/(\nu_\tau+\bar{\nu}_\tau)$ skew (e_{Esctau})	0	0.05	🟢
Escale CC/NC skew (e_{EscNC})	0	0.05	🟢
Escale up/horizontal skew (e_{Escctup})	0	0.03	🟢

Table 4.2: Parameters and priors used by the fits in Fig 4.12 (b). The colours in the last column describe which fit used which parameters: 🔵 low uncertainties only using θ_{23}, ΔM^2 and the overall norm; 🔴 standard uncertainties; 🟢 more uncertainties.

In Fig. 4.12 (a) we can see the influence of different values of $\theta_{23}^{\text{true}}$ as well as the change of the neutrino mass hierarchy to IH. As we can see, the sensitivity is minimal around a value of $\theta_{23}^{\text{true}} = 45°$, while $\theta_{23}^{\text{true}} = 42°$ clearly gives us a higher sensitivity. Over all, the dependency on θ_{23} is not as high as for the measuring of the NMH.

The sensitivity for the inverted hierarchy is always below the sensitivity for the normal hierarchy the normal hierarchy using the same $\delta_{\text{CP}}^{\text{true}}$ and $\theta_{23}^{\text{true}}$. Additionally, we can see that the oscillation probabilities for different values of δ_{CP} seem to shift compared to each other, because the local minimum for $\delta_{\text{CP}}^{\text{true}} = \frac{3}{2}\pi$ is not as distinctive as for NH anymore. For $\delta_{\text{CP}}^{\text{true}} = 0$ the maximum of the fits is shifted to 1.2π. Summarized, the inverted hierarchy needs more exposure time to reach a comparable significance than NH.

In Fig. 4.12 (b) we can see the influence of different magnitudes of systematics, described in table 4.2. The additional parameters introduced for ORCA decrease the sensitivity by 0.5 to 1σ in the maximum (difference between ● and ●). The difference in sensitivity between the standard fit (●) and the low uncertainties fit (●), which only fits oscillation parameters, is much higher. Interestingly, the sensitivity for the complementary value of δ_{CP}, where we find the degenerate state of the oscillations, is only coming from the oscillation parameters θ_{23}, ΔM^2 and the overall norm, because all curves meet at the local minimum. Indeed, the other fit parameters are close to their true value for the fits near the local minima.

4.3 Beam Experiment

Like P2O for ORCA, we can use the Protvino beam for measurements with Super-ORCA, calling it "Protvino to Super-ORCA" (P2SO). Knowing that ORCA can get a sensitivity for measuring δ_{CP} comparable to Super-ORCA using atmospheric neutrinos, we expect a high sensitivity for P2SO.

First, we take another look at the expected event numbers at the detector site, assuming Super-ORCA to be built next to ORCA, see Fig. 4.13. As we can see, the event rates for Super-ORCA are much higher for low energies as for ORCA due to the effective mass (see Fig. 3.19). Additionally, in the left plot (a), we can see the second maximum in the energy range below 2 GeV, which we could not see in the event numbers for ORCA due to the lower effective mass for ORCA below 2 GeV. Here we have the problem of a high background of NC-events, which appear in a similar amount as the electron neutrinos, which are responsible for the majority of the δ_{CP} sensitivity.

When we apply the detector resolution (b), we can see that the distinctive peaks are smeared out, so we cannot distinguish them anymore. However, the information is still accessible to us, as we will see later in the results of the fits. The NC-events are shifted to lower energies, just like the tau neutrino events that use the same resolution.

As we can see here again, the main sensitivity comes from $\overset{(-)}{\nu}_e$ in the energy range between 1 and 6 GeV and a bit from $\overset{(-)}{\nu}_\mu$ in the energy range between 2 and 4 GeV.

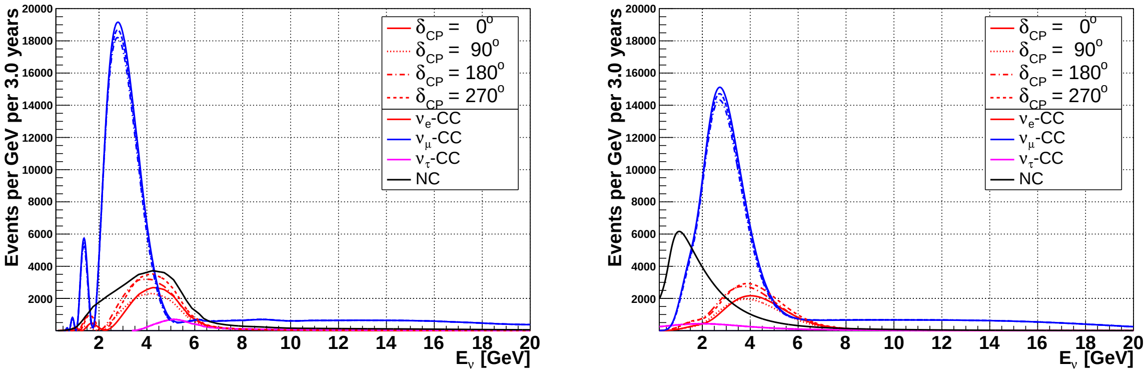

(a) Without resolution (b) With resolution

Figure 4.13: Expected event numbers for Super-ORCA after three years of data taking using the Protvino neutrino beam (positive horn polarity), assuming NH to be true for four different values of $\delta_{\rm CP}$. (a) With and (b) without resolution; in both plots the effective detector mass is applied.

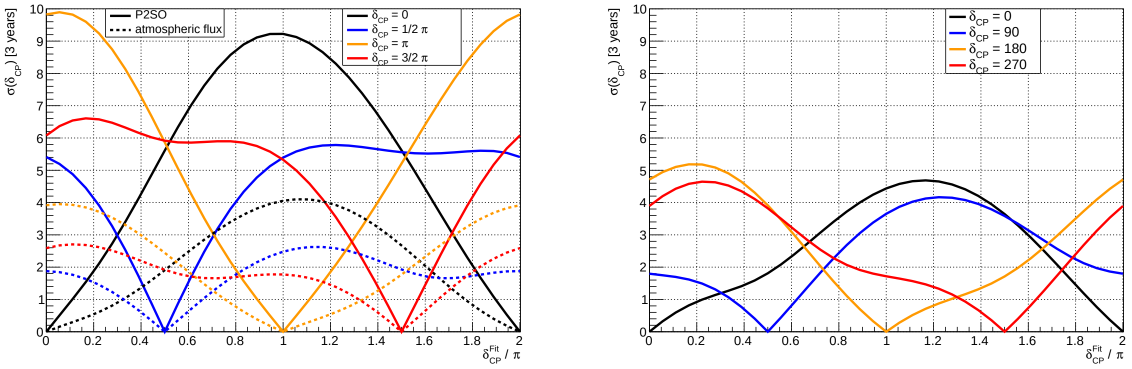

(a) Protvino beam (b) J-PARC beam

Figure 4.14: Sensitivity to exclude certain values of $\delta_{\rm CP}$ with Super-ORCA after three years of data taking as a function of $\delta_{\rm CP}^{\rm fit}$: (a) using the Protvino beam (solid lines) compared to the sensitivity using the atmospheric flux (dashed lines); (b) using the J-PARC beam, which sensitivity is much less than those of the Protvino beam. Normal hierarchy and θ_{23} is assumed.

Due to the second peak in the low energy range below 2 GeV, the general form of the fit curves in Fig. 4.14 (solid lines) resemble more the forms of the Super-ORCA fits using the atmospheric flux (dashed lines), than those of P2O. The sensitivity increases very much comparing P2SO with the normal sensitivity using the atmospheric flux. 70 % of $\delta_{\rm CP}$ values are disfavoured with more than 3σ for $\delta_{\rm CP}^{\rm true} = 0$ and π, while we can reject

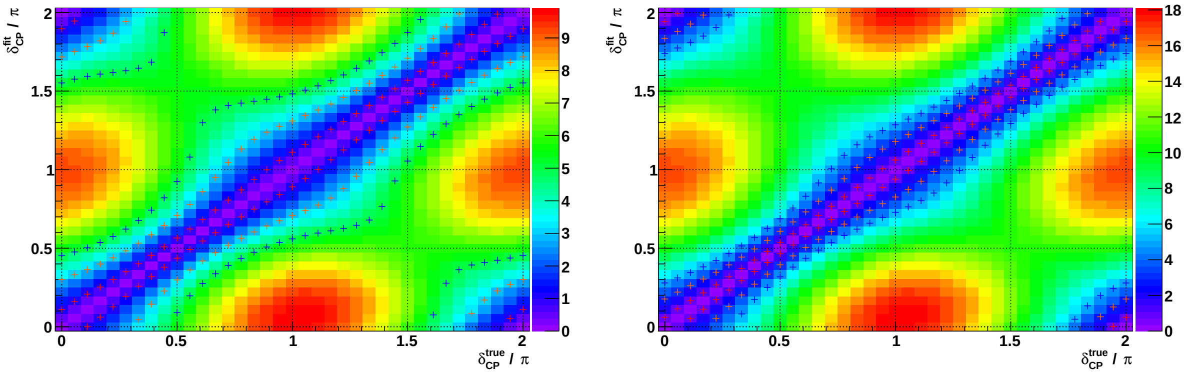

(a) after three years

(b) after ten years

Figure 4.15: Sensitivity to exclude certain values of $\delta_{\rm CP}$ with P2SO after three (a) and ten (b) years of data taking as a function of $\delta_{\rm CP}^{\rm true}$ and $\delta_{\rm CP}^{\rm fit}$ for NH, $\theta_{23} = 42°$. The colour gives the significance, while the red (orange, blue) crosses give the 1σ (3σ, 5σ) precision for each $\delta_{\rm CP}^{\rm true}$.

even 80 % for $\frac{\pi}{2}$ and $\frac{3}{2}\pi$ with a sensitivity of 3σ. In all cases, we have more than 50 % of $\delta_{\rm CP}$ to be excluded with more than 5σ after only three years of data taking, while we hardly reach 4σ using the atmospheric flux.

Additionally, we used another beam generated by the Hyper-Kamiokande collaboration using J-PARC, with a detector site in the Pacific ocean between Japan and Korea, Fig. 4.14 (b). As we can see in Fig. 3.18 (b), this beam has a flux with a high but sharp peak between 0.2 and 1.5 GeV and then drops rapidly with energy. As we have seen, our main sensitivity comes from the energy range between 1 and 6 GeV, but the high energy region of that interval is suppressed by the flux. Additionally, the detector site is not directly in the path of the J-PARC beam, but has an off-axis angle of 1.5°. Therefore the sensitivity after three years of data taking is much less than for the Protvino beam.

In Fig. 4.15 we can see the dependency of the statistical significance (colour) to reject a certain $\delta_{\rm CP}^{\rm fit}$ value assuming $\delta_{\rm CP}^{\rm true}$ to be true as a function of $\delta_{\rm CP}^{\rm fit}$ and $\delta_{\rm CP}^{\rm true}$ after three (a) and ten years (b) of data taking. The red (orange, blue) crosses give the 1σ (3σ, 5σ) precision for each $\delta_{\rm CP}^{\rm true}$. Compared to 4.10 (b), the maxima have shifted a little bit towards 0 and π and the sensitivity has increased by a factor of 2 thanks to the beam. After ten years of data taking, we can refute 95 % ($85 - 90$ %, $73 - 80$ %) of $\delta_{\rm CP}^{\rm fit}$ with a 1σ (3σ, 5σ) precision (see also Fig. 4.17 (a)).

If we compare the significance for CP conservation rejection after 10 years of data taking for P2SO and Hyper-Kamiokande using the J-PARC beam and DUNE in Fig. 4.16, we can see that we are competitive with the other two detectors. Though, Hyper-Kamiokande can reject CP-violation with a significance of 3σ for 70 % $-$ 78 % (depending on detector configuration) of $\delta_{\rm CP}^{\rm fit}$ values [33], and DUNE can reject 70 % [34], while we can reject 65 % of $\delta_{\rm CP}^{\rm fit}$ values. The different detector types of Hyper-Kamiokande are

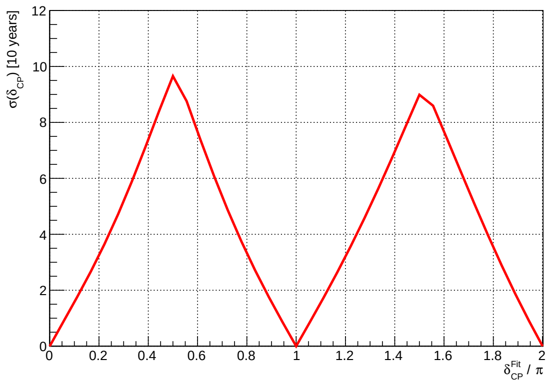

(a) P2SO

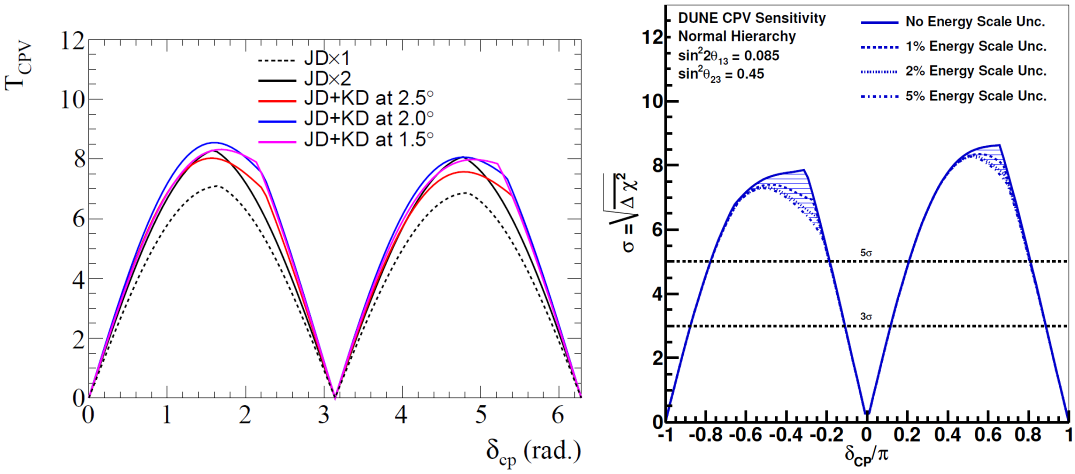

(b) Hyper-Kamiokande

(c) DUNE

Figure 4.16: Significance for CP conservation rejection as a function of $\delta_{\mathrm{CP}}^{\mathrm{fit}}$ after ten years of data taking and NH: (a) P2SO; (b) J-PARC beam for Hyper-Kamiokande using one or two detectors in Japan with an off-axis angle of 2.5° (JD×1 and JD×2), or one detector in Japan (JD) and one in Korea (KD) with an off-axis angle of 2.5°, 2.0° or 1.5° [33]; (c) DUNE for different energy scale uncertainties [34].

always using the J-PARC beam with one or two detectors in Japan with an off-axis angle of 2.5° (JD×1 and JD×2), or one detector in Japan with an off-axis angle of 2.5° and one in Korea with an off-axis angle of 2.5° (JD+KD at 2.5°), 2.0° (JD+KD at 2.5°) or 2.0° (JD+KD at 1.5°) [33].

Fig. 4.17 shows the fraction of δ_{CP} values that can be rejected with a precision of 1σ, 3σ and 5σ for P2SO and 1σ for different Hyper-Kamiokande configurations after ten years of data taking. The 1σ precision for P2SO and Hyper-Kamiokande is comparable to each other, with both detectors rejecting 95 % of $\delta_{\mathrm{CP}}^{\mathrm{fit}}$ on average. However, the result is complementary, because Hyper-Kamiokande is more sensitive around 0 and π, while

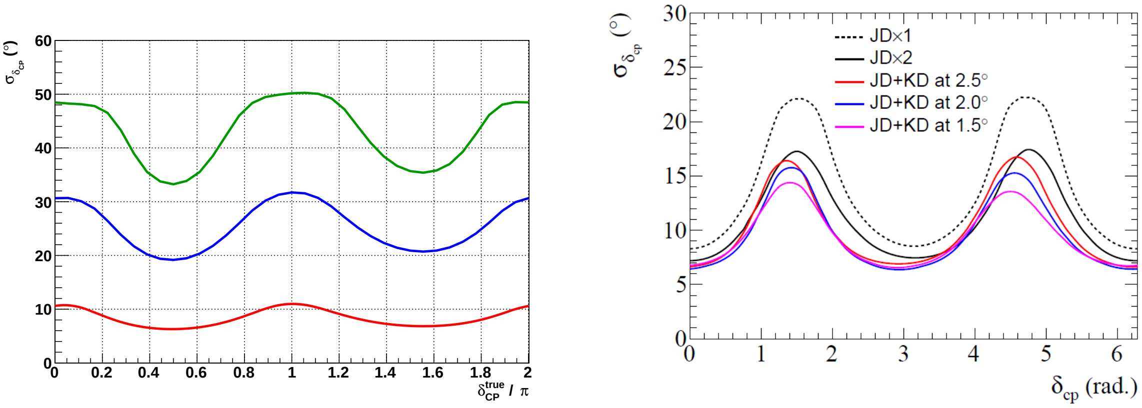

(a) P2SO

(b) Hyper-Kamiokande [33]

Figure 4.17: 1σ precision of the δ_{CP} measurement as a function of the true $\delta_{\mathrm{CP}}^{\mathrm{true}}$ value after 10 years of data taking for (a) P2SO (red) and (b) Hyper-Kamiokande [33]. Additionally, the blue and the green lines in (a) show the 3σ and 5σ precisions for P2SO.

P2SO has the best sensitivity around $\pi/2$ and $3\pi/2$. The reason for this difference in sensitivity comes from the second oscillation maximum below 2 GeV, Super-ORCA is able to measure, and the different baselines of the beams.

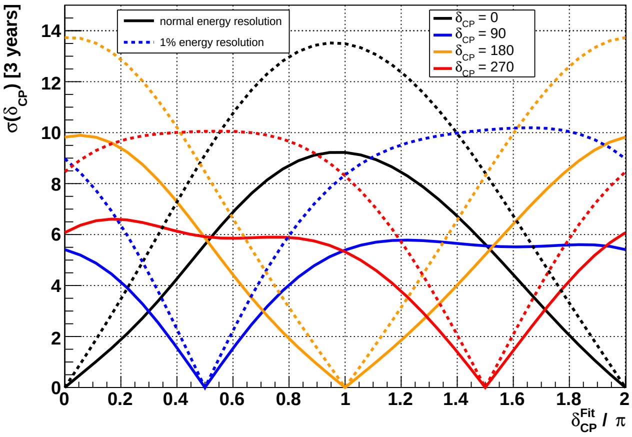

Figure 4.18: Sensitivity to exclude certain values of δ_{CP} with P2SO after three years of data taking as a function of $\delta_{\mathrm{CP}}^{\mathrm{fit}}$ for four different values of $\delta_{\mathrm{CP}}^{\mathrm{true}}$. Solid lines are using the normal energy resolution, dashed lines are using an energy resolution equal to 1 % using NuTag.

To improve the sensitivity even more, we have to reduce the smearing due to energy resolution. In order to do so, we have to track the primary particles like pions any muons directly after the Protvino accelerator. This is done by the silicon pixle detector NuTag, which measures the properties of the primary particles and therefore we the properties of each ν in the beam (neutrino tagging), especially their energy E_{true}. With this knowledge, we can reduce the energy resolution to or even below 1 % of the true energy [35].

Shown in Fig. 4.18 is the result of this reduction of the energy smearing. The sensitivity of P2SO is again improved significantly, the local minima vanish due to the achievable resolution power, so the second oscillation maximum is usable. Only after three years of data taking, we can reject 95 % (85 %, 75 %) of δ_{CP} with a precision of 1σ (3σ, 5σ). After ten years of data taking we could reject 97.5 % (92 %, 87 %) of δ_{CP} with a precision of 1σ (3σ, 5σ). These precisions differ slightly for different values of $\delta_{\text{CP}}^{\text{true}}$, but they do show the potential of P2SO using NuTag. If we want to compare the result with those of Super-PINGU (see Fig. 4.11 (b)), we have to multiply the results with $1/\sqrt{3} \approx 0.577$ to get the sensitivity after one year of data taking. Super-PINGU would have to measure at least two years until they reach the same P2SO sensitivity using the NuTag energy resolution upgrade.

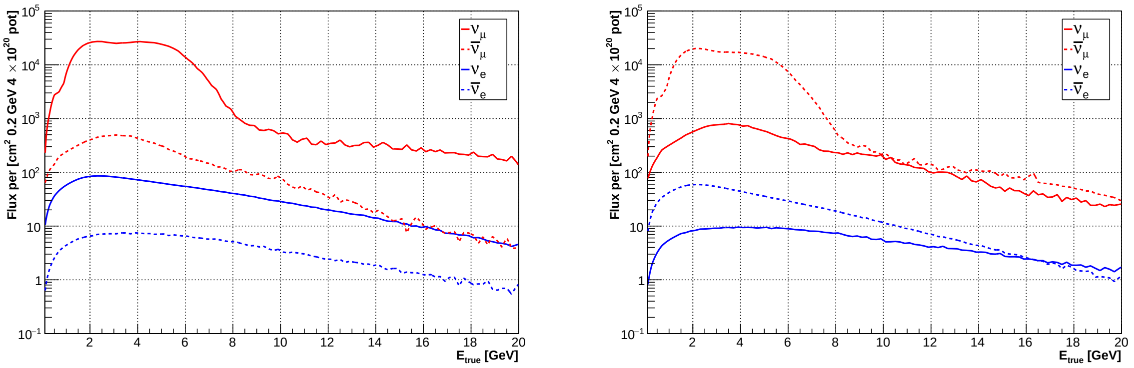

(a) positive horn polarity

(b) negative horn polarity

Figure 4.19: Unoscillated flux of a Protvino beam from 2017 [36] with positive horn (a) and negative horn polarity (b), favouring the neutrinos or antineutrinos, respectively.

Finally, we want to test the influence of the horn polarity of the beam: If we use positive horn polarity, as we did until now, we get a ν_μ beam with a little contamination of $\bar{\nu}_\mu$, ν_e and $\bar{\nu}_e$. If we use negative horn polarity, we mainly get a $\bar{\nu}_\mu$ beam with a higher contamination of the other neutrino flavours. We are interested which horn polarity works better for determining the CP-violating phase.

Because positive horn polarity generates a neutrino beam, we expect a higher sensitivity for normal hierarchy, while it is the other way around for negative horn polarity, where we expect a higher sensitivity for inverted hierarchy. To test this we use a slightly different setup of the Protvino beam from 2017 [36], because we do not have data of the Protvino beam we have used before [26] for negative horn polarity.

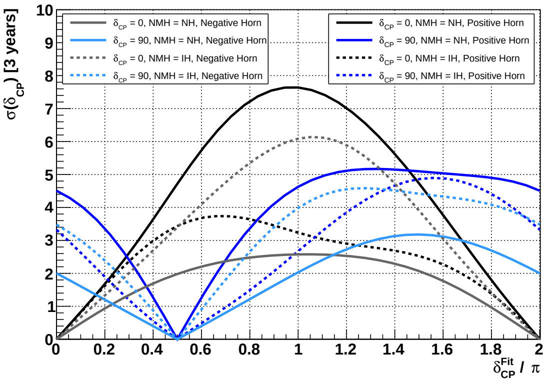

Figure 4.20: Sensitivity to exclude certain values of δ_{CP} with P2SO after three years of data taking as a function of $\delta_{\mathrm{CP}}^{\mathrm{fit}}$ using the Protvino beam from 2017 [36] for two different values of $\delta_{\mathrm{CP}}^{\mathrm{true}}$. Solid lines are used for NH, dashed lines for IH. Black and dark blue lines are used for positive horn polarity, grey and light blue lines for negative horn polarity.

As we can see in Fig. 4.20 these expectations are fulfilled. However, we see that the sensitivity for the positive horn polarity assuming NH is much better than the results for the negative horn polarity, while the difference is not so high if we assume IH to be true.

Chapter 5

Conclusion and Outlook

Due to the measurement of neutrino oscillation in matter, the unknown sign of the large squared mass difference, which defines the neutrino mass hierarchy (NMH), and the CP-violating phase δ_{CP} can be determined. The ORCA detector build by the KM3NeT collaboration, which is under construction at the moment, will be able to measure the NMH. A hypothetical, ten times denser detector called Super-ORCA is planned to determine δ_{CP}. It is still unknown whether nor where it will be built, but the preliminary sensitivities derived in this thesis are a strong encouragement to build it.

To calculate the sensitivity of a detector, the performance is parametrized and the reconstructed events used to determine the oscillation parameters are calculated based on this parametrisation. For this a software called *paramNMH* is used, which was developed for ORCA. In this thesis, the parametrization was extended by adding uncertainties concerning the energy scale, the particle identification and flux.

The additional uncertainties are reducing the statistical significance to determine the neutrino mass hierarchy with ORCA to a minimum of 2σ after three years, depending on the oscillation parameter θ_{23}. However, the uncertainties for new particle identification and energy scale parameters are educated guesses but are not based on any dedicated studies of the particle identification and the energy scale. Those uncertainties must be ascertained and implemented into the calculation and, if needed, the parameters have to be adapted.

Additionally, *paramNMH* was adopted for Super-ORCA, which is capable of measuring δ_{CP}. The sensitivity on the mass hierarchy is of course improved compared to ORCA significantly, so Super-ORCA could deliver the same results after only three years of data taking, ORCA could provide after eight years. Though, while the input parameters for ORCA are well established, the sensitivities for Super-ORCA are based on idealised and simplified detector response estimates and do not make use of the full KM3NeT detector simulation chain.

The use of a beam experiment with both detectors increases the sensitivity, so that Super-ORCA is comparable to other neutrino detectors like Hyper-Kamiokande, DUNE or Super-PINGU. The 1σ precision of δ_{CP} after ten years of data taking rejects 95 % of δ_{CP} and is complementary to the expected sensitivity for Hyper-Kamiokande.

When ORCA starts taking data, the uncertainties on the additional parameter will be better known, so that the parametrization can be improved. With a better understanding of the ORCA detector and more detailed work on the performance of Super-ORCA, the parametrization for the denser detector will be more accurate as well. The possibility of using a better energy resolution for beam experiments using neutrino tagging (NuTag), would open the way to the third generation of neutrino detectors, increasing the sensitivity of the measurement significantly, so that Super-PINGU would have to take data for two years to reach the same significance than P2SO with NuTag in one year. The 1σ precision of refuting δ_{CP} after 10 years of data taking will include 97.5 % of δ_{CP}, while Hyper-Kamiokande can refute 95 %.

Appendix A

Tables and Figures

	ν_e	$\bar{\nu}_e$	ν_μ	$\bar{\nu}_\mu$	ν_τ	$\bar{\nu}_\tau$	ν_{NC}	$\bar{\nu}_{\mathrm{NC}}$
N_{Meff} [Mton]	6.01	6.01	5.02	4.81	5.77	5.66	5.10	4.83
E_{min} [GeV]	1.84	1.74	1.85	1.80	3.25	3.09	3.58	3.97
σ_{Meff} [GeV]	6.13	5.16	4.76	3.84	12.2	12.9	22.9	35.8
x_0	0.047	0.011	1.350	0.903	0.141	0.163	0.081	0.061
x_1 [GeV$^{-x_2}$]	0.59	0.42	-1.05	-4.53	1.81	1.04	0.89	0.51
x_2	1.17	0.70	0.16	1.83	1.82	1.57	1.48	0.88
m_0	1.670	1.573	1.694	1.453	1.745	1.750	1.663	1.641
m_1	-1.097	-0.812	-1.285	-0.595	-1.664	-1.617	-1.520	-1.500
m_2	0.418	0.290	0.399	0.033	0.608	0.599	0.477	0.431
s_0	0.35	0.45	0.51	0.73	0.35	0.37	0.42	0.65
s_1 [GeV^{-1}]	0.238	0.206	0.187	0.120	0.179	0.185	0.149	0.114
s_2 [GeV^{-2}]	-0.0014	-0.0009	0.0051	0.0075	0.0014	0.0015	0.0028	0.0034
x_{med} [GeV$^{1/2}$]	10.0	8.0	13.0	8.0	14.0	12.5	14.5	15.5

Table A.1: Parameters for ORCA detector response (effective mass, PID, resolution), see section 3.1.3.

	standard	Energy scale without priors	Energy scale with priors
e_{Escale}	1	1.005	0.999
e_{EscNC}	0	-0.056	-0.024
e_{Escnu}	0	-0.018	-0.00025
e_{Escemu}	0	0.010	0.0046
e_{Esctau}	0	-0.074	-0.043
e_{Escctup}	0	0.030	0.022

Table A.2: Energy scale parameter values for NH, $\theta_{23} = 49°$, ORCA.

	standard	Energy scale without priors	Energy scale with priors
e_{Escale}	1	0.990	0.998
e_{EscNC}	0	0.015	0.0044
e_{Escnu}	0	0.024	0.0049
e_{Escemu}	0	-0.0061	-0.0013
e_{Esctau}	0	0.037	0.019
e_{Escctup}	0	-0.018	-0.014

Table A.3: Energy scale parameter values for IH, $\theta_{23} = 44°$, ORCA.

	standard	PID without priors	PID with priors = 5%	PID with priors = 2.5%
p_{nuanu0}	0	0.024	-0.022	-0.0095
p_{nuanu1}	0	0.24	0.053	0.016
p_{trsh0}	0	0.077	0.037	0.013
p_{trsh1}	0	0.016	0.0063	0.0043

Table A.4: PID parameter values for NH, $\theta_{23} = 49°$, ORCA.

	standard	PID without priors	PID with priors = 5%	PID with priors = 2.5%
p_{nuanu0}	0	-0.0009	0.0076	0.006
p_{nuanu1}	0	-0.076	-0.0076	-0.0042
p_{trsh0}	0	-0.020	0.0023	0.0065
p_{trsh1}	0	-0.031	-0.022	-0.013

Table A.5: PID parameter values for IH, $\theta_{23} = 44°$, ORCA.

	standard	Flux without priors, $\theta_{23} = 41°$	Flux with priors, $\theta_{23} = 41°$	Flux without priors, $\theta_{23} = 49°$	Flux with priors, $\theta_{23} = 49°$
f_{Fluxct1}	0	0.011	0.0046	-0.011	0.01
f_{Fluxct2}	0	0.011	0.0064	0.00052	0.0069
f_{Fluxemu}	0	0.052	0	0.00052	-0.0012
f_{nunubar}	0	-0.021	-0.011	0.019	-0.0062
$f_{\mathrm{nunubarct}}$	0	-0.015	-0.00012	-0.028	0.00068
f_{nunubarE}	0	0.015	0.014	-0.036	-0.044
f_{TrShct}	0	0.029	0.00049	0.05	0.0026
f_{TrShE}	0	-0.008	0.005	0.0013	-0.0037

Table A.6: Flux parameter values for NH, ORCA.

	standard	Flux without priors, $\theta_{23} = 41°$	Flux with priors, $\theta_{23} = 41°$	Flux without priors, $\theta_{23} = 49°$	Flux with priors, $\theta_{23} = 49°$
f_{Fluxct1}	0	0.0018	-0.006	-0.0061	-0.0049
f_{Fluxct2}	0	0.0036	-0.0048	-0.0046	-0.0053
f_{Fluxemu}	0	0.008	0.0007	-0.023	0.00023
f_{nunubar}	0	-0.0034	-0.0061	0.023	0.018
$f_{\text{nunubarct}}$	0	-0.025	-0.00089	0.0042	-0.00029
f_{nunubarE}	0	0.0068	0.0067	-0.018	-0.017
f_{TrShct}	0	-0.017	-0.0012	-0.022	-0.00069
f_{TrShE}	0	0	0.0045	0.002	-0.0032

Table A.7: Flux parameter values for IH, ORCA.

	ν_e	$\bar{\nu}_e$	ν_μ	$\bar{\nu}_\mu$	ν_{NC}	$\bar{\nu}_{\text{NC}}$
N_{Meff}	0.62	0.80	0.62	0.80	0.21	0.21
E_{min} [GeV]	0.32	0.34	0.52	0.56	0.29	0.30
σ_{Meff} [GeV]	0.46	0.40	0.45	0.34	0.80	0.66
x_0	0.02	0.02	0.94	0.97	0.10	0.10
x_1 [GeV]	0	0	0	0	-0.06	-0.06
x_2 [GeV^2]	0.03	0.01	0	0	0	0
x_3 [GeV]	0	0	0	0	0.02	0.02
m_0	0.98	1.05	0.97	1.05	0.37	0.26
m_1	1.41	1.14	1.86	1.58	0.37	0.49
m_2 [GeV]	0.33	0.33	0.40	0.39	1.00	1.00
m_3	-2.97	-2.75	-3.00	-3.00	-1.42	-1.23
s_0	0.13	0.11	0.13	0.11	0.15	0.15
s_1 [GeV$^{1/2}$]	0.12	0.12	0.11	0.11	0	0
s_2 [GeV]	0	0	0	0	0	0
s_3 [GeV^{s_4}]	0	0	0	0	0.01	0.004
s_4	0	0	0	0	1.80	2.10
d_0	0.0005	0.0005	0.0005	0.0005	0.01	0.01
d_1 [GeV$^{1/2}$]	0	0	0	0.0001	0.34	0.34
d_2 [GeV]	0.005	0.13	0.18	0.10	0	0
d_3 [GeV^2]	0	0.0003	0	0	0	0
d_4	0.5	0.3	0.4	0.3	0.6	0.6
d_5 [GeV^{d_6}]	0.26	0	0	0	0	0
d_6	-1.18	0	0	0	0	0

Table A.8: Parameters for Super-ORCA detector response (effective mass, PID, resolution), see section 4.1.1. We assumed the $\overset{(-)}{\nu}_\tau$-CC parameters to be identical to the with $\overset{(-)}{\nu}_{\text{NC}}$ parameters.

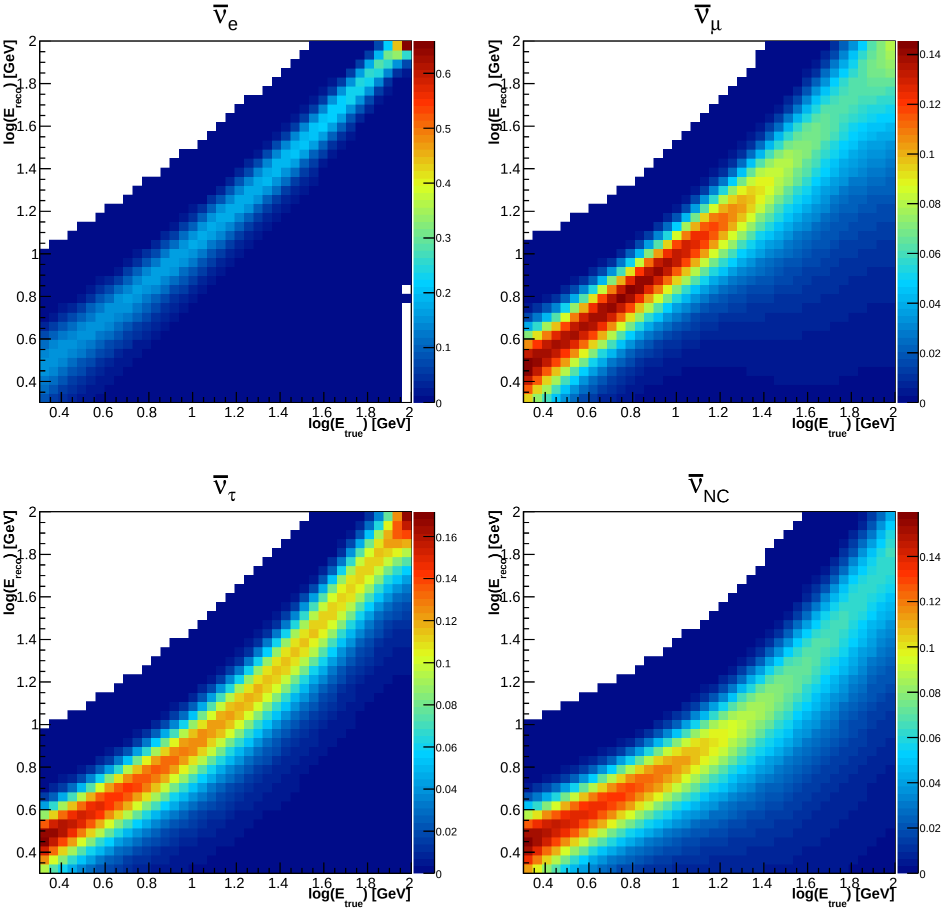

Figure A.1: Energy resolution E_{reco} in dependency of the true energy for all antineutrino interaction types for ORCA.

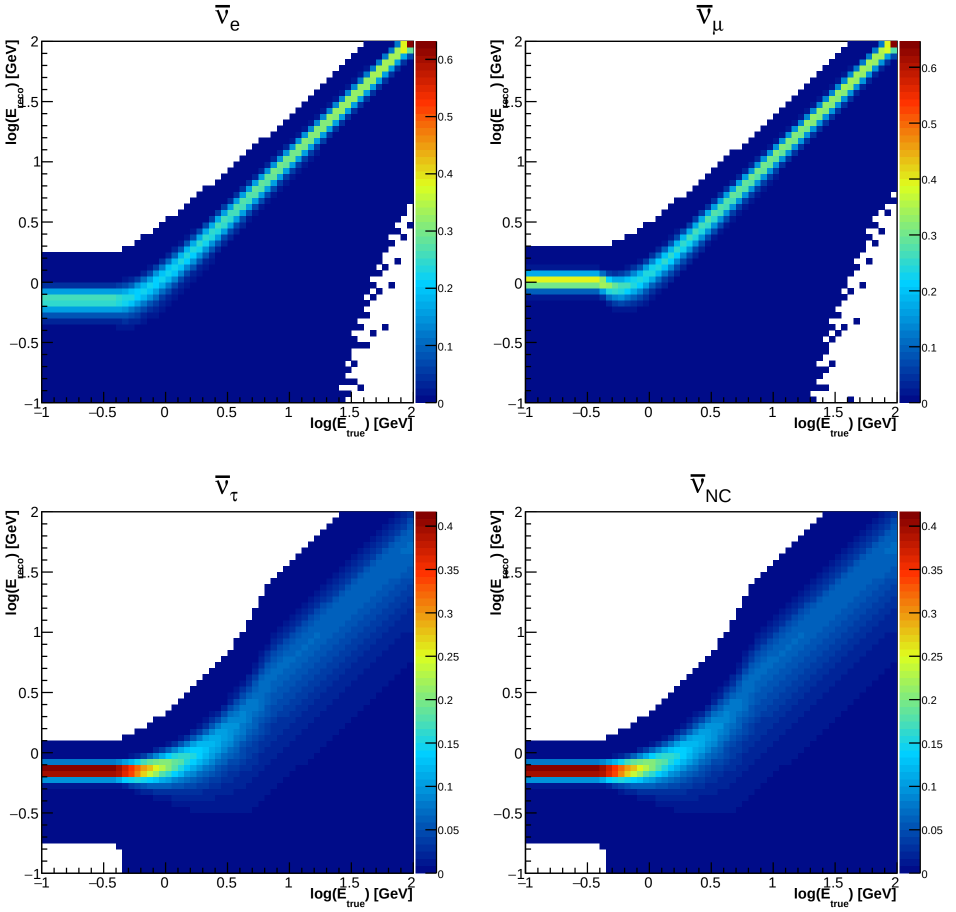

Figure A.2: Energy resolution E_{reco} in dependency of the true energy for all antineutrino interaction types for Super-ORCA. All bins below 0.4 GeV have the same resolution calculated for 0.4 GeV.

List of Figures

List of Tables

Bibliography

[1] R. Davis, D. S. Harmer, and K. C. Hoffman, *Search for neutrinos from the sun*, Phys.Rev.Lett. 20 1205–1209 (1968).

[2] Adrián-Martínez S. et al., *Letter of Intent for KM3Net 2.0, 2016*, J. Phys. G: Nucl. Part. Phys. 43 084001.

[3] B. Pontecorvo, *Inverse beta processes and nonconservation of lepton charge*, 1957, Zh.Eksp.Teor.Fiz. 34 (1957) 247, Sov.Phys.JETP 7 (1958) 172-173

[4] Z. Maki, M. Nakagawa, S. Sakata, *Remarks on the Unified Model of Elementary Particles*, 1962, Bibcode:1962PThPh..28..870M.

[5] Glen Cowan et al., *Asymptotic Formulae for Likelihood-Based Tests of New Physics*, The European Physical Journal C 71.2 (Feb. 2011), p. 1554. doi: 10.1140/epjc/s10052-011-1554-0.

[6] N. Schmitz, *Neutrinophysik*, Stuttgart 1997.

[7] *http://www.staff.uni-mainz.de/wurmm/juno.html*, 20.08.18.

[8] Particle Data Group, *Review of particle physics*, 2014.

[9] C. Giunti and Chung W. Kim, *Fundamentals of Neutrino Physics and Astrophysics*, 2007.

[10] T. Araki, et al, The KamLAND Collaboration, *Precision Measurement of Neutrino Oscillation Parameters with KamLAND*, In *Phys. Rev. Lett.* 100, p. 221803, 2008, DOI: 10.1103/PhysRevLett.100.221803, arXiv:0801.4589.

[11] W. Demtröder, *Experimentalphysik 4: Kern-, Teilchen- und Astrophysik*, 4. Auflage, 2014, ISBN: 978-3-642-21475-2, DOI: 10.1007/978-3-642-21476-9.

[12] A.M. Dziewonski & D.L. Anderson, *Preliminary reference Earth model*, In *Physics of the Earth and Planetary Interiors* 25 (1981) 297—356, December 1980.

[13] M. Honda et al., *Calculation of atmospheric neutrino flux using the interaction model calibrated with atmospheric muon data*, In *Phys. Rev. Lett.* D 75, p. 043006, 2007, DOI: 10.1103/PhysRevD.75.043006, arXiv:astro-ph/0611418.

[14] Q.R. Ahmad et al., *Direct Evidence for Neutrino Flavor Transformation from Neutral-Current Interactions in the Sudbury Neutrino Observatory*, In *Phys. Rev. Lett.* 89, p. 011301, 2002, DOI: 10.1103/PhysRevLett.89.011301, arXiv:nucl-ex/0204008.

[15] U.F. Katz, Ch. Spiering, *High-energy neutrino astrophysics: Status and perspectives*, Progress in Particle and Nuclear Physics 67 (2012) 651–704.

[16] *https://www.sheffield.ac.uk/physics/research/pppa/nugroup/nuwch.*

[17] *https://root.cern.ch/.*

[18] M. Volkert, *A muon veto for the measurement of the downgoing neutrino flux with KM3NeT/ORCA*, 2017, Master thesis.

[19] C. Andreopoulos et al., *The GENIE Neutrino Monte Carlo Generator, PHYSICS & USER MANUAL*, 2015, arXiv:1510.05494.

[20] G. Cowan et al., *Asymptotic formulae for likelihood-based tests of new physics*, In *The European Physical Journal C* 71, p. 1554, 2011, DOI: 10.1140/epjc/s10052-011-1554-0, arXiv:1007.1727.

[21] L. Quinn, *Determining the Neutrino Mass Hierarchy with KM3NeT/ORCA*, PhD thesis, 2018.

[22] *https://root.cern.ch/root/html534/guides/minuit2/Minuit2.html.*

[23] *https://de.wikipedia.org/wiki/Orthodrome.*

[24] G.D. Barr and S. Robbins, *Uncertainties in Atmospheric Neutrino Fluxes*, Phys.Rev.D74:094009, 2006, arXiv:astro-ph/0611266.

[25] D. Zaborov, *The KM3NeT Neutrino Telescope and the potential of a neutrino beam from Russia to the Mediterranean Sea*, 2018, arXiv:1803.08017.

[26] V.I. Garkusha, F.N. Novoskoltsev & A.A. Sokolov, *Neutrino oscillation research using the U-70 accelerator complex (in Russian)*, IHEP Preprint 2015-5, code: Prot_2200.

[27] *https://wiki.hyperk.org/working-groups/wg8-beam-accelerator/fluxfiles*, 04.10.18.

[28] S. Bhadra et al., *Letter of Intent to Construct a nuPRISM Detector in the J-PARC Neutrino Beamline*, 2014, arXiv:1412.3086.

[29] M. Tanabashi et al. (Particle Data Group), *Neutrino Masses, Mixing, and Oscillations*, 2017, Phys. Rev. D 98, 030001 (2018).

[30] Private Communication with Jannik Hofestädt.

[31] F. Capozzi et al., *Current unknowns in the three-neutrino framework*, April 2018, DOI: 10.1016/j.ppnp.2018.05.005, arXiv:1804.09678.

[32] S. Razzaque, A. Yu. Smirnov, *Super-PINGU for measurement of the leptonic CP-phase with atmospheric neutrinos*, 2015, DOI: 10.1007/JHEP05(2015)139, arXiv:1406.1407.

[33] K. Abe et al., *Physics Potentials with the Second Hyper-Kamiokande Detector in Korea*, 2018, arXiv:1611.06118.

[34] R. Acciarri et al., *Long-Baseline Neutrino Facility (LBNF) and Deep Underground Neutrino Experiment (DUNE) Conceptual Design Report Volume 2: The Physics Program for DUNE at LBNF*, 2016, arXiv:1512.06148.

[35] M. Perrin-Terrin talk at ORCA face-to-face meeting, Valencia.

[36] Private Communication A.A. Sokolov, IHEP, Protvino 2017, code: Prot_171113.

Acknowledgements

We would like to thank those people who helped me during the last year and without whom this work would not have been possible.

My first thanks go to Dr. habil. Thomas Eberl for the supervision of my thesis. Special thanks to Dr. Jannik Hofestädt, who always had an open ear and the right answers for my problems. Thanks as well to Dr. Jürgen Brunner and Liam Quinn, who have developed and maintained *paramNMH* and helped me with solving a lot of problems.

Last, special thanks to my parents, who have supported me in any non-physical way possible.

Erklärung

Hiermit bestätige ich, dass ich diese Arbeit selbstständig und nur unter Verwendung der angegebenen Hilfsmittel angefertigt habe.

Erlangen, den 30. November, 2018

Marc Bruchner